DIGITAL ACCESS TO SCHOLARSHIP AT HARVARD
DASH.HARVARD.EDU

HARVARD LIBRARY
Office for Scholarly Communication

Overcoming Genetic and Immunological Barriers to the Use of Adeno-Associated Viral Vectors for Ocular Gene Therapy

Citation
Wang, Sean Ku. 2020. Overcoming Genetic and Immunological Barriers to the Use of Adeno-Associated Viral Vectors for Ocular Gene Therapy. Doctoral dissertation, Harvard Medical School.

Permanent link
https://nrs.harvard.edu/URN-3:HUL.INSTREPOS:37365226

Terms of Use
This article was downloaded from Harvard University's DASH repository, and is made available under the terms and conditions applicable to Other Posted Material, as set forth at http://nrs.harvard.edu/urn-3:HUL.InstRepos:dash.current.terms-of-use#LAA

Share Your Story

The Harvard community has made this article openly available.
Please share how this access benefits you. Submit a story .

Accessibility

Overcoming Genetic and Immunological Barriers to the Use of Adeno-Associated Viral Vectors for Ocular Gene Therapy

by

Sean K. Wang

Submitted in Partial Fulfillment of the Requirements for the M.D. Degree
with Honors in a Special Field at Harvard Medical School

February 2020

Abstract

Gene therapy with adeno-associated viral (AAV) vectors has emerged as a promising treatment option for patients with debilitating genetic disorders. Nonetheless, implementation of AAV gene therapy for many conditions still faces substantial challenges, precluding large-scale clinical translation of these vectors. In this thesis, I explore two of the major barriers limiting the use of AAV gene therapy in patients: 1) genetic heterogeneity in diseases, which complicates the development of targeted therapies, and 2) vector-induced immunity and inflammation, which reduce treatment efficacy and, in some cases, may compromise safety. With collaborators, I design and conduct experimental studies addressing these obstacles in the eye, one of the primary sites of ongoing gene therapy trials. These studies result in several advances for the ocular gene therapy field, including 1) the creation of two novel AAV vectors capable of treating a genetically heterogeneous eye disease in mice, 2) the discovery that expression of AAV vectors in specific cell types correlates with ocular inflammation, 3) the successful mitigation of vector-induced inflammation in mice and pigs by “cloaking” AAV genomes from host immune responses, and 4) the development of a fluorescence *in situ* hybridization-based method that can visualize and quantify individual AAV genomes in transduced cells. This collection of work may improve the safety and efficacy of AAV vectors for a broad range of vision disorders with the potential to vastly expand the number of patients who benefit from gene therapy.

Table of Contents

Acknowledgements

The work presented here would not have been possible without the boundless support of my friends, family, and colleagues. Most of all, I would like to thank my mentor, Dr. Constance Cepko, for serving as a shining example of someone I aspire to be like both scientifically and personally. I am indebted to all members of the Cepko lab for their discussions, encouragement, and feedback, especially my collaborators: Yunlu Xue for expertise on electroretinography, Parimal Rana for performing the optomotor behavioral assays, Christin Hong for assistance with RNA sequencing, and Sylvain Lapan for insights on SABER-FISH. I would also like to thank former lab members Wenjun Xiong and David Wu for bringing the issue of AAV toxicity to our attention, as well as Ying Kai Chan from the lab of Dr. George Church for the opportunity to study the TLR9-blocking strategy in the retina. Finally, I am grateful for my collaborators from other completed and ongoing projects that I did not have a chance to include here, specifically Dr. Elio Raviola at Harvard, Dr. Matthew Lawrence at Yale/RxGen, Dr. Guangping Gao at UMass, and Dr. Dong Feng Chen at Schepens Eye Research Institute.

This research would also not have been possible without generous institutional support. In particular, I would like to thank Microscopy Resources on the North Quad for microscopy training, the Mouse Behavioral Core at Harvard Medical School for assistance with behavioral tests, and the Flow Cytometry Core at Joslin Diabetes Center for access to cell sorters. I am also thankful for the Howard Hughes Medical Institute, Foundation Fighting Blindness, and Fight for Sight for funding my work, as well as the Harvard Office of Technology Development and Astellas Pharma Inc. for ongoing efforts to bring AAV8-sCX3CL1 into clinical trials.

Lastly, I am beyond grateful for my friends and family who have been there for me throughout the past five years on my path toward becoming a physician-scientist. Thank you especially to my parents Zhu and Hanlin, my brother Jason, my partner Thazin, and my dog Siri, as well as Julia, Alex, Jenny, Felicia, and the many other medical school classmates who I am lucky to call friends.

Chapter 1: Overview

Gene therapy refers to the delivery of nucleic acids such as DNA and RNA as a therapeutic strategy for human disease. With the advent of whole genome sequencing and personalized medicine, it has become clear that many disease states are driven by underlying genetic changes, often due to aberrant activity in just one or several key genes (1). The goal of gene therapy is to restore healthy levels and functions of these genes in patients, whether by introducing a corrected allele, silencing or removing deleterious mutations, or expressing proteins beneficial to the affected cells (2). To achieve this, numerous methods for nucleic acid transfer have been devised over the past 50 years, many of which utilize viruses given their natural propensity to insert genetic material into cells (3). Recombinant vectors derived from a range of different viruses have demonstrated clinical promise in animal models and occasionally in humans (4). Increasingly, however, adeno-associated viral (AAV) vectors are emerging as the preferred vehicle for gene therapy delivery, especially in non-dividing cell types such as those of the brain, retina, muscle, and heart.

Derived from a member of the *Parvoviridae* family, AAV vectors are non-integrating and replication-defective, but capable of long-term transgene expression in host cells even after a single administration (5,6). The genetic material of these vectors, a single-stranded DNA genome, is surrounded by a protein capsid that determines cell tropism and can be modified to selectively infect target tissues (7,8). A major advantage of AAV vectors is their safety profile and relative lack of pathogenicity, as infection with the wild-type virus is not known to cause symptoms in humans (5). In addition, because they do not typically integrate into the host genome, AAV vectors have a much lower risk of insertional mutagenesis and oncogenesis compared to other viral vectors being considered for gene therapy (5). These therapeutically desirable features of AAV vectors have culminated in their use in over 200 clinical trials to date (clinicaltrials.gov).

Ocular disorders are thought to be particularly amenable to AAV gene therapy due to the accessibility and small size of the eye as well as the fact that it is relatively immune privileged (9). Indeed, the first *in vivo* AAV vector to be approved by the FDA, voretigene neparvovec-rzyl (Luxturna), was developed for an ophthalmic disease, establishing the safety and efficacy of this approach (10). Nonetheless, substantial obstacles still prevent widespread adoption of AAV vectors for debilitating eye conditions such as retinitis pigmentosa (RP), which affects one in every 4000 people and presently lacks effective treatment (11). Specifically, a significant barrier to implementing gene therapy in these patients is the extensive heterogeneity of causal mutations, as several thousand mutations spanning over 80 different genes are known to be pathogenic for RP (12). While it may be theoretically possible to design and produce AAV vectors targeting each of these genetic lesions, this is in practice infeasible considering the high cost of clinical trials and limited number of individuals with any given mutation. Until this issue of genetic heterogeneity is addressed, AAV gene therapy will likely not be a realistic treatment option for the majority of patients with RP.

Another concern with AAV gene therapy in both ocular and non-ocular tissues is the induction of inflammation and cellular toxicity by the vector, especially at higher doses. Although AAV vectors are considered non-pathogenic, they are still recognized by the body as foreign and can elicit robust innate and adaptive immune responses which may compromise the therapeutic effect (13). In fact, there is growing evidence from large animal studies as well as human clinical trials that host immunity may not only reduce the efficacy of gene therapy in the eye, but in some cases trigger intraocular inflammation despite immunosuppression with corticosteroids, resulting in structural damage and permanent vision loss (14–16). How AAV vectors precisely mediate this inflammation and cellular toxicity is not understood, although signaling through Toll-like receptor 9 (TLR9) has been implicated (17). A better characterization of these responses may enable the development of safer and less immunogenic AAV vectors, improving the clinical utility of AAV gene therapy both in and outside the eye.

In this thesis, I present data from five studies that I either led or helped design addressing the genetic and immunological barriers to ocular AAV gene therapy described above. To develop a broadly applicable gene therapy for RP circumventing the issue of genetic heterogeneity, I first investigated the pathways downstream of causal mutations in different mouse models of RP and identified microglial activation as a shared mechanism, leading to the discoveries of soluble CX3CL1 (Chapter 2) and TGF-β1 (Chapter 3) as potential mutation-independent treatments for this disease. In collaborative projects, I then help characterize the components of AAV vectors responsible for cellular toxicity and inflammation in the eye (Chapter 4) and report a strategy to mitigate these responses in both mice and pigs by "cloaking" the vector from TLR9-mediated immunity (Chapter 5). Finally, leveraging recent advances in fluorescent *in situ* hybridization, I describe a novel method to visualize and quantify individual AAV genomes in tissues (Chapter 6), allowing for future work examining early cellular events in the eye and other organs following transduction with toxic AAV vectors.

References:

1. Chakravarti A, Little P. Nature, nurture and human disease. Vol. 421, Nature. 2003. p. 412–4.
2. Dunbar CE, High KA, Joung JK, Kohn DB, Ozawa K, Sadelain M. Gene therapy comes of age. Vol. 359, Science. American Association for the Advancement of Science; 2018.
3. Friedmann T, Roblin R. Gene therapy for human genetic disease? Science. 1972;175(4025):949–55.
4. Finer M, Glorioso J. A brief account of viral vectors and their promise for gene therapy. Vol. 24, Gene Therapy. Nature Publishing Group; 2017. p. 1–2.
5. Daya S, Berns KI. Gene therapy using adeno-associated virus vectors. Vol. 21, Clinical Microbiology Reviews. 2008. p. 583–93.
6. Sehara Y, Fujimoto K, Ikeguchi K, Katakai Y, Ono F, Takino N, et al. Persistent Expression of Dopamine-Synthesizing Enzymes 15 Years After Gene Transfer in a Primate Model of Parkinson's Disease. Hum Gene Ther Clin Dev. 2017 Jun;28(2):74–9.
7. Gao G, Vandenberghe LH, Alvira MR, Lu Y, Calcedo R, Zhou X, et al. Clades of Adeno-Associated Viruses Are Widely Disseminated in Human Tissues. J Virol. 2004;78(12):6381–8.
8. Zinn E, Pacouret S, Khaychuk V, Turunen HT, Carvalho LS, Andres-Mateos E, et al. In silico reconstruction of the viral evolutionary lineage yields a potent gene therapy vector. Cell Rep. 2015;12(6):1056–68.
9. Rodrigues GA, Shalaev E, Karami TK, Cunningham J, Slater NKH, Rivers HM. Pharmaceutical Development of AAV-Based Gene Therapy Products for the Eye. Vol. 36, Pharmaceutical Research. Springer New York LLC; 2019.
10. Russell S, Bennett J, Wellman JA, Chung DC, Yu Z-F, Tillman A, et al. Efficacy and safety of voretigene neparvovec (AAV2-hRPE65v2) in patients with RPE65 -mediated inherited retinal dystrophy: a randomised, controlled, open-label, phase 3 trial. Lancet. 2017 Aug 26;390(10097):849–60.
11. Berson EL. Retinitis pigmentosa: unfolding its mystery. Proc Natl Acad Sci U S A. 1996 May 14;93(10):4526–8.
12. Daiger SP, Sullivan LS, Bowne SJ. Genes and mutations causing retinitis pigmentosa. Clin Genet. 2013 Aug;84(2):132–41.
13. Reichel FF, Dauletbekov DL, Klein R, Peters T, Ochakovski GA, Seitz IP, et al. AAV8 Can Induce Innate and Adaptive Immune Response in the Primate Eye. Mol Ther. 2017 Dec 6;25(12):2648–60.
14. Cukras C, Wiley HE, Jeffrey BG, Sen HN, Turriff A, Zeng Y, et al. Retinal AAV8-RS1 Gene Therapy for X-Linked Retinoschisis: Initial Findings from a Phase I/IIa Trial by Intravitreal Delivery. Mol Ther. 2018 Sep 5;26(9):2282–94.
15. Bainbridge JWB, Mehat MS, Sundaram V, Robbie SJ, Barker SE, Ripamonti C, et al. Long-Term Effect of Gene Therapy on Leber's Congenital Amaurosis. N Engl J Med. 2015;372(20):1887–97.
16. Dimopoulos IS, Hoang SC, Radziwon A, Binczyk NM, Seabra MC, MacLaren RE, et al. Two-Year Results after AAV2-Mediated Gene Therapy for Choroideremia: The Alberta Experience. Am J Ophthalmol. 2018;193:130–42.
17. Faust SM, Bell P, Cutler BJ, Ashley SN, Zhu Y, Rabinowitz JE, et al. CpG-depleted adeno-associated virus vectors evade immune detection. J Clin Invest. 2013;123(7):2994–3001.

Chapter 2: Soluble CX3CL1 gene therapy improves cone survival and function in mouse models of retinitis pigmentosa

Abstract

Retinitis pigmentosa (RP) is a disease that initially presents as night blindness due to genetic deficits in the rod photoreceptors of the retina. Rods then die, causing dysfunction and death of cone photoreceptors, the cell type that mediates high acuity and color vision, ultimately leading to blindness. We investigated immune responses in mouse models of RP and found evidence of microglial activation throughout the period of cone degeneration. Using adeno-associated viral (AAV) vectors, delivery of genes encoding microglial regulatory signals led to the identification of soluble CX3CL1 (AAV8-sCX3CL1) as a promising therapy for degenerating cones. Subretinal injection of AAV8-sCX3CL1 significantly prolonged cone survival in three strains of RP mice. Rescue of cones was accompanied by improvements in visual function. AAV8-sCX3CL1 did not affect rod survival, microglial localization, or inflammatory cytokine levels in the retina. Furthermore, although RNA sequencing of microglia demonstrated marked transcriptional changes with AAV8-sCX3CL1, pharmacological depletion of up to ~99% of microglia failed to abrogate the effect of AAV8-sCX3CL1 on cone survival. These findings indicate that AAV8-sCX3CL1 can rescue cones in multiple mouse models of RP via a pathway that does not require normal numbers of microglia. Gene therapy with sCX3CL1 is a promising mutation-independent approach to preserve vision in RP and potentially other forms of retinal degeneration.

Contributions

Sean K. Wang[1], Yunlu Xue[1], Parimal Rana[1], Christin M. Hong[1], Constance L. Cepko[1,2]

[1] Departments of Genetics and Ophthalmology, Harvard Medical School, Boston, MA 02115, USA

[2] Howard Hughes Medical Institute, Chevy Chase, MD 20815, USA

S.K.W. and C.L.C. conceived the study; S.K.W., Y.X., and C.L.C. designed research; S.K.W., Y.X., P.R., and C.M.H. performed experiments and analyzed data; S.K.W. and C.L.C. wrote the paper.

Note: This work has been published. For full-text, please refer to:
Wang SK, Xue Y, Rana P, Hong CM, Cepko CL. Soluble CX3CL1 gene therapy improves cone survival and function in mouse models of retinitis pigmentosa. *Proc Natl Acad Sci*. 2019 Apr 29;116(20):201901787.

Introduction

Retinitis pigmentosa (RP) is a disease of the eye that presents with progressive degeneration of rod and cone photoreceptors, the light-sensing cells of the retina (1). The disease can result from mutations in any of over 80 different genes and is the most common inherited cause of blindness in the world, affecting an estimated 1 in 4000 people (2–4). One approach proposed to treat RP is gene therapy, e.g. using adeno-associated viral (AAV) vectors to deliver a wild-type allele to complement a mutated gene (5,6). While this approach has proven successful in other conditions, even leading to the approval of a gene therapy for RPE65-associated Leber's congenital amaurosis (7), it is difficult to implement for the majority of RP patients given the extensive heterogeneity of genetic lesions and the fact that a causal mutation is not always identified (2). A gene therapy that is agnostic to the many possible underlying mutations in RP would provide a treatment option for a greater number of patients. Presently, there is no effective therapy of any kind for RP, and despite more than a dozen clinical trials to date, none have been able to demonstrate an improvement in visual function (8).

In patients with RP, there is an initial loss of rods, the photoreceptors that mediate vision in dim light. Clinically, this results in the first manifestation of RP, poor or no night vision, which usually occurs between birth and adolescence (1). Daylight vision in RP is largely normal for decades, but eventually deteriorates, beginning when most of the rods have died. This is due to dysfunction and then death of the cone photoreceptors, which are essential for high acuity and color vision, and are the major source of morbidity in the disease (1). Importantly, while the vast majority of genes implicated in RP are expressed in rods, few actually exhibit expression in cones, suggesting the existence of one or more common mechanisms by which diverse mutations in rods trigger non-autonomous cone degeneration (9–11). We and others have attempted to elucidate these mechanisms with the goal of developing therapies for RP that preserve cone vision regardless of the underlying mutation (12–16).

One possible contributor to non-autonomous cone degeneration in RP that has yet to be closely examined is the body's own immune system. As they die, many cells, including photoreceptors in RP, release damage-associated molecular patterns (DAMPs) that act as endogenous danger signals and incite inflammation (17,18). By numerous pathways, DAMPs can then stimulate proinflammatory cytokine activity or recruit immune cells, such as neutrophils and T cells, to the site of cell death (17). Even in homeostatic conditions, the retina is continuously surveyed by microglia, resident macrophages of the central nervous system (CNS) derived from myeloid progenitors in the embryonic yolk sac (19,20). Following injury or exposure to noxious stimuli, microglia may become activated, a state characterized by acquisition of an ameboid morphology, upregulation of cytokines, and increased phagocytosis of cell debris (21–23). Notably, activation of microglia can also be modulated by various regulatory factors from the CNS, allowing for manipulation of these cells in both experimental models and in humans (24–26).

Here, we investigated the involvement of immune responses during non-autonomous cone degeneration in mouse models of RP. We found evidence of microglial activation throughout the period of cone death. We subsequently developed four AAV vectors to deliver genes that target retinal microglia. One of these genes, soluble CX3CL1, also called fractalkine, significantly prolonged cone survival in three different mouse models of RP. Rescue of cones was accompanied by improvements in visual function, highlighting the potential of soluble CX3CL1 as a mutation-independent treatment for RP and other retinal diseases.

Results

Microglia reside in the photoreceptor layer throughout cone degeneration

The *rd1* and *rd10* mouse lines are commonly used models of RP (27). Each strain harbors a different mutation in the rod-specific phosphodiesterase beta subunit, with *rd1* exhibiting more rapid photoreceptor degeneration than *rd10* (28). To characterize immune

activity during non-autonomous cone degeneration, we first performed RT-PCR on retinas from albino *rd1* and pigmented *rd10* mice, as well as those from albino CD-1 and pigmented C57BL/6 (B6) mice, two strains with wild-type (WT) vision. Primers were designed to assay for mRNAs of both innate and adaptive immune components, including inflammatory cytokines (*Il1a*, *Il1b*, *Il6*, *Tnf*), complement (*C1qa*), neutrophils (*Ly6g*), T cells (*Cd4, Cd8a*), and microglia (*Tmem119*, *Cd68*). In each strain, two distinct time points were examined corresponding to the onset (postnatal day 20 [P20] for *rd1*, P40 for *rd10*) and peak (P35 for *rd1*, P70 for *rd10*) of cone degeneration (12,13). Compared to age-matched CD-1 and B6 retinas, *rd1* and *rd10* retinas demonstrated significant upregulation of *Il1a*, *Tnf*, and *C1qa* at both time points, as well as *Il1b* specifically in *rd1* mice (Fig. 1*A*-*D*). Upregulation of these factors was also associated with higher expression levels of *Tmem119*, a microglia-specific marker (29), and *Cd68*, a marker of lysosomal activity and microglial activation (30), but not *Ly6g*, *Cd4*, or *Cd8a*. As activated microglia have previously been shown to produce and secrete IL1A, TNF, and C1Q (23), these data pointed to a possible proinflammatory role of microglia during non-autonomous cone death.

Rods in mice, and in humans, are far more abundant than cones, representing ~95% of photoreceptors (31,32). In the retina, rod and cone cell bodies form a structure called the outer nuclear layer (ONL), which dramatically shrinks with rod death in RP until only a single row of cells remains, comprising the surviving cones. Pathologic infiltration of microglia into the ONL has been described during the initial rod death phase of RP (33,34). However, less is known about how microglia behave during the subsequent period of cone degeneration. To aid in visualizing microglia within the retina, RP and WT animals were bred with Cx3cr1^{GFP} reporter mice, in which microglia are labeled with GFP (35). Only ~10% of retinal microglia were normally located in the ONL in cross-sections from CD-1;Cx3cr1$^{GFP/+}$ and B6;Cx3cr1$^{GFP/+}$ WT eyes (Fig. 1*E*-*H*). Conversely, ~40-50% of retinal microglia could be seen in the ONL in *rd1*;Cx3cr1$^{GFP/+}$ and *rd10*;Cx3cr1$^{GFP/+}$ mice throughout the period of cone degeneration. Thus,

even after the disappearance of rods, cone degeneration in RP mice was associated with both cytokine upregulation and the continued localization of microglia to the photoreceptor layer.

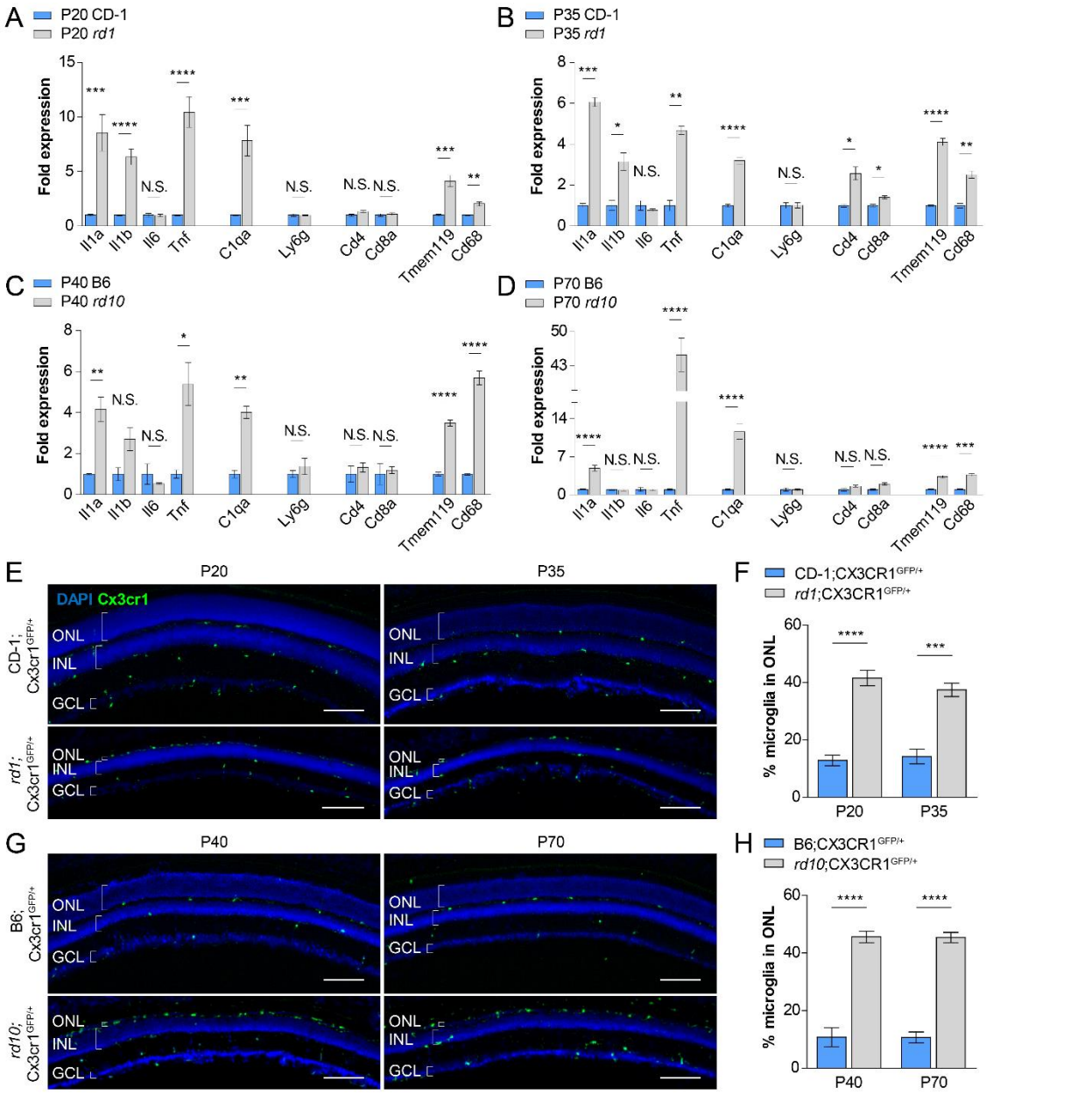

Figure 1. Expression of immune response genes and microglial localization during cone photoreceptor degeneration. (**A-D**) Whole retina RNA expression levels of immune response genes during onset (P20, P40) and peak (P35, P70) of cone degeneration in two RP mouse models (albino *rd1* and pigmented *rd10*) versus two WT strains (albino CD-1 and pigmented B6). (**E, G**) Retinal cross-sections from RP and WT mice depicting Cx3cr1^{GFP}-labeled microglia during cone degeneration. Scale bar, 100 µm. (**F, H**) Quantification of percent of total retinal microglia residing in the ONL during cone degeneration in RP and WT mice. Data shown as mean ± SEM. *n* = 4-6 animals per condition. * *P*<0.05, ** *P*<0.01, *** *P*<0.001, **** *P*<0.0001 by two-tailed Student's t-test with Bonferroni correction for (A-D), two-tailed Student's t-test for (F, H). ONL, outer nuclear layer; INL, inner nuclear layer; GCL, ganglion cell layer; N.S., not significant.

Overexpression of soluble CX3CL1 prolongs cone survival in RP mice

We hypothesized that during the later stages of RP, activated microglia may create a proinflammatory environment deleterious to nearby cones. We further postulated that overexpression of factors opposing microglial activation might alleviate this damage, favoring cone survival. To test this idea, a previously characterized AAV vector expressing GFP under the human red opsin promotor (AAV8-GFP) was chosen to label cones and aid in their quantification (Fig. 2*A*) (36). Subretinal delivery of AAV8-GFP in neonatal mice led to brightly labeled cones throughout the entire retina, allowing for visualization of these cells in adult animals (Fig. 2*B* and Supplemental Fig. 1). AAV vectors were then designed to express either CD200 or CX3CL1, membrane-bound proteins reported to suppress proinflammatory activity via their respective receptors on microglia, CD200R and CX3CR1 (24–26). Given the hypothesized interaction between microglia and degenerating cones, full-length variants of CD200 (fCD200) and CX3CL1 (fCX3CL1) were expressed under the cone-specific human red opsin promoter (Fig. 2*D*). Because soluble variants of both proteins have also been described (37,38), additional AAV vectors were generated for soluble CD200 (sCD200) and CX3CL1 (sCX3CL1) using the human Best1 promoter to drive expression in the retinal pigment epithelium (RPE), a cell layer adjacent to the photoreceptors (Supplemental Fig. 2) (39).

The ability of the four vectors (AAV8-fCD200, AAV8-sCD200, AAV8-fCX3CL1, AAV8-sCX3CL1) to prolong cone survival was initially tested in *rd1* mice, which were injected at P0-P1 and evaluated at P50. In mouse RP, cone death proceeds from center to periphery starting from the optic nerve head. To assay cone survival during degeneration, the central retina was therefore interrogated. Using an ImageJ module, the number of GFP-positive cones in the central retina could be reliably quantified (Supplemental Fig. 3). Compared to *rd1* retinas infected with AAV8-GFP alone (Fig. 2*C*), there was no significant improvement in cone survival with the addition of AAV8-fCD200, AAV8-sCD200, or AAV8-fCX3CL1 (Fig. 2*E* and *F*). In contrast, co-infection of AAV8-GFP with AAV8-sCX3CL1 significantly increased the number of

cones remaining in the central retina (*P*<0.0001), supporting a potential therapeutic effect of sCX3CL1 in RP.

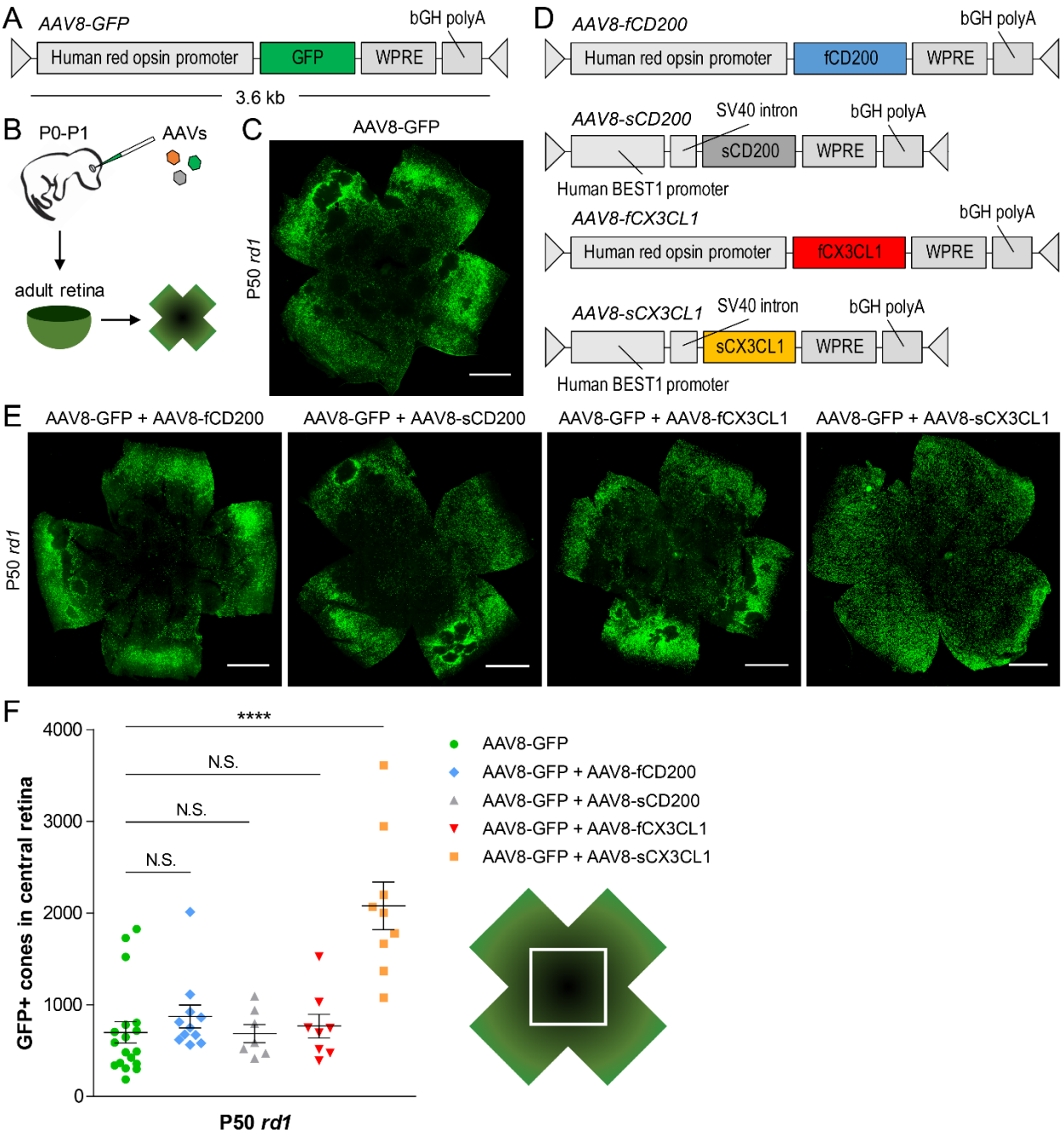

Figure 2. Effect of CD200 and CX3CL1 overexpression on cone survival. (**A**, **B**) Schematics of AAV8-GFP vector and delivery. (**C**) Flat-mounted P50 *rd1* retina infected at P0-P1 with AAV8-GFP. Scale bar, 1 mm. (**D**) Schematics of CD200 and CX3CL1 AAV vectors. (**E**) Flat-mounted P50 *rd1* retinas infected at P0-P1 with the indicated vectors. Scale bar, 1 mm. (**F**) Quantification of cone survival in the central retina of P50 *rd1* retinas infected with the indicated vectors. Data shown as mean ± SEM. *n* = 7-18 animals per condition. **** *P*<0.0001 by two-tailed Student's t-test with Bonferroni correction.

Cone survival with AAV8-sCX3CL1 was next examined in older, more degenerated *rd1* mice. At P75, co-infection of AAV8-GFP with AAV8-sCX3CL1 continued to prolong cone survival compared to AAV8-GFP alone (P<0.001) (Fig. 3*A-A"*). Even at P100, by which time the central retinas of AAV8-GFP infected eyes were nearly devoid of cones, significantly greater cone survival with AAV8-sCX3CL1 was observed (P<0.01) (Fig. 3*B-B"*). To determine if sCX3CL1 might provide a generic therapy for non-autonomous cone death, AAV8-sCX3CL1 was trialed in *rd10* (Fig. 3*C-C"*) and *Rho*$^{-/-}$ (Fig. 3*D-D"*) mice. *Rho*$^{-/-}$ mice lack rhodopsin, the

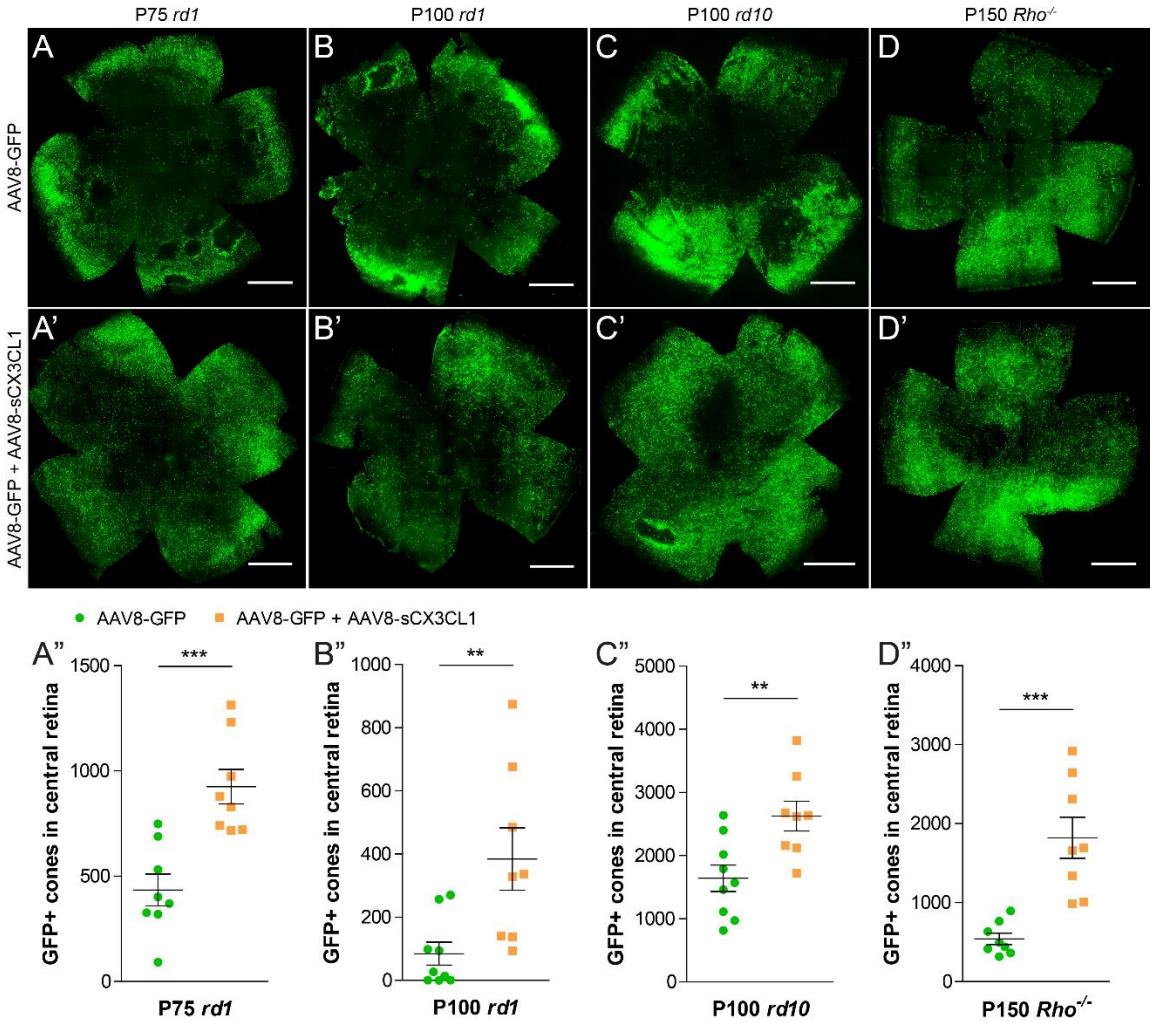

Figure 3. Effect of AAV8-sCX3CL1 on long-term cone survival in RP mouse models. (**A-D'**) Flat-mounted P75 *rd1* (A, A'), P100 *rd1* (B, B'), P100 *rd10* (C, C'), and P150 Rho$^{-/-}$ (D, D') retinas infected at P0-P1 with AAV8-GFP alone or AAV8-GFP plus AAV8-sCX3CL1. Scale bar, 1 mm. (**A"-D"**) Quantification of cone survival in the central retina of P75 *rd1* (A"), P100 *rd1* (B"), P100 *rd10* (C"), and P150 Rho$^{-/-}$ (D") retinas. Data shown as mean ± SEM. n = 7-9 animals per condition. ** P<0.01, *** P<0.001 by two-tailed Student's t-test.

photopigment gene in rods, which is also the most commonly mutated gene in humans with autosomal dominant RP (40). Photoreceptors in the *Rho*$^{-/-}$ strain degenerate at a slower rate than in the *rd1* or *rd10* strain (41,42). In *rd10* and *Rho*$^{-/-}$ mice, AAV8-GFP plus AAV8-sCX3CL1 again resulted in a higher number of cones in the central retina compared to AAV8-GFP alone (P<0.01 for *rd10*, P<0.001 for *Rho*$^{-/-}$).

AAV8-sCX3CL1 improves cone-mediated visual function

Because we observed histological preservation of cones with AAV8-sCX3CL1, we asked whether cone-mediated vision was similarly rescued. Electroretinography (ERG), a physiological measure of retinal activity in response to light, can be used to record rod and cone activity. We thus used ERG to measure photopic b-wave responses, a cone-mediated signal from the inner retina known to decline relatively early in RP in both animals and humans (1,13). ERG recordings from P40 *rd10* mice showed no difference in photopic b-waves between AAV8-GFP infected and untreated eyes, as expected (Fig. 4*A*). In contrast, in animals treated with AAV8-GFP plus AAV8-sCX3CL1 in one eye and AAV8-GFP in the other, a modest but significant increase in photopic b-wave amplitudes could be seen (P<0.05) (Fig. 4*A* and *B*).

To evaluate vision using a behavioral test, we additionally subjected *rd10* mice to the optomotor assay. This assay elicits a motor response to simulated motion, that of moving stripes. By varying the stripe width until the animal is no longer able track the stimulus, a spatial frequency threshold can be calculated, corresponding to the visual acuity in each eye (43,44). Mice were placed under bright light conditions to probe cone vision. In *rd10* mice infected with AAV8-GFP in one eye and untreated in the other, optomotor results from P45 to P60 showed a similar drop in visual acuity between the two eyes over time (Fig. 4*C*). However, when animals were infected with AAV8-GFP plus AAV8-sCX3CL1 instead of AAV8-GFP alone, loss of visual acuity over the same interval was slowed in the AAV8-sCX3CL1 treated eye (P<0.01).

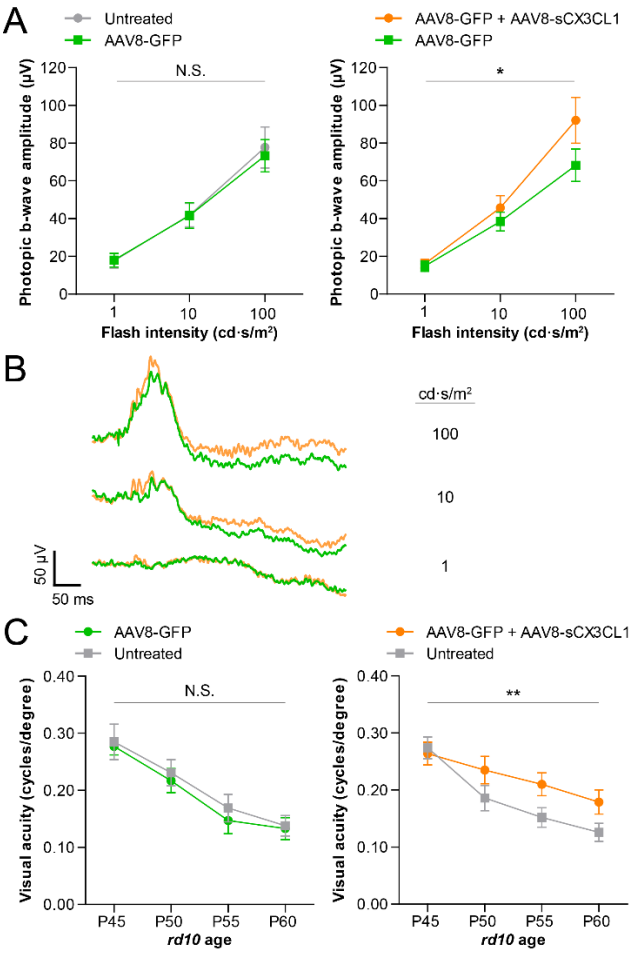

Figure 4. Effect of AAV8-sCX3CL1 on cone-mediated visual function.

(**A**) Photopic ERG responses in P40 *rd10* mice infected at P0-P1 with AAV8-GFP in one eye only (*n* = 12) or AAV8-GFP in one eye and AAV8-GFP plus AAV8-sCX3CL1 in the contralateral eye (*n* = 17).

(**B**) Representative photopic ERG traces from a P40 *rd10* animal infected with AAV8-GFP in one eye (green) and AAV8-GFP plus AAV8-sCX3CL1 in the contralateral eye (orange).

(**C**) Optomotor assessments of visual acuity in *rd10* mice at the indicated ages compared to contralateral uninjected eyes after infection with AAV8-GFP (*n* = 20) or AAV8-GFP plus AAV8-sCX3CL1 (*n* = 21).

Data shown as mean ± SEM. * *P*<0.05, ** *P*<0.01 by two-tailed two-way ANOVA. N.S., not significant.

AAV8-sCX3CL1 does not improve rod survival, microglial localization, or retinal inflammation

Absence of CX3CL1 signaling during rod degeneration in RP mice has been shown to decrease rod survival, reduce the number of microglia in the ONL, and upregulate levels of TNF and IL1B in the retina (33,45). We thus investigated the effect of AAV8-sCX3CL1 on these phenotypes to uncover possible mechanisms by which sCX3CL1 gene therapy might promote cone survival. Rods normally comprise ~95% of cells in the ONL and are thought to support cone survival through several pathways, such as secretion of trophic factors and maintenance of a normoxic environment (15,31,46). To examine how sCX3CL1 treatment affected rods, the thickness of the ONL in RP retinas was measured. In P20 *rd1* and P40 *rd10* retinas infected with AAV8-GFP, only one to two rows of nuclei remained in the ONL (Fig. 5*A*), consistent with

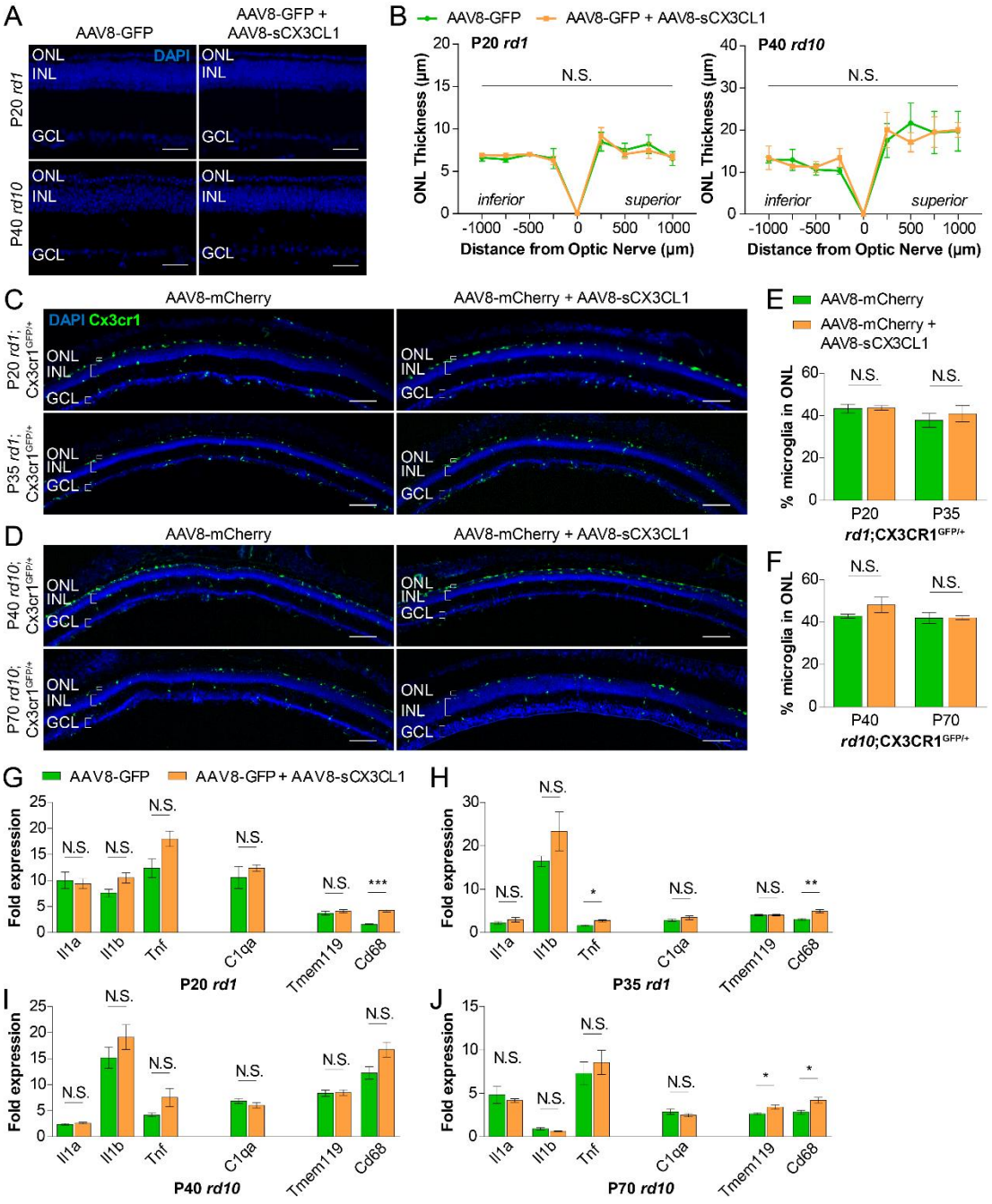

Figure 5. Effect of AAV8-sCX3CL1 on microglial localization and immune response genes during cone degeneration. (**A**) Mid-peripheral retinal cross-sections from *rd1* and *rd10* mice infected at P0-P1 with AAV8-mCherry or AAV8-mCherry plus AAV8-sCX3CL1. Scale bar, 50 µm. (**B**) Quantification of ONL thickness in *rd1* and *rd10* retinas during onset of cone degeneration. (**C, E**) Cx3cr1^{GFP}-labeled microglia in *rd1* (C) and *rd10* (E) retinal cross-sections infected with AAV8-mCherry or AAV8-mCherry plus AAV8-sCX3CL1. Scale bar, 100 µm. (**D, F**) Quantification of microglia residing in the ONL during cone degeneration with or without AAV8-sCX3CL1. (**G-J**) Whole retina RNA expression levels of immune response genes during the onset (G, I) and peak (H, J) of cone degeneration with and without AAV8-sCX3CL1. Fold changes are relative to age-matched WT retinas. Data shown as mean ± SEM. *n* = 4-6 animals per condition. * *P*<0.05, ** *P*<0.01, *** *P*<0.001 by two-tailed two-way ANOVA for (B), two-tailed Student's t-test for (D, F), two-tailed Student's t-test with Bonferroni correction for (G-J). ONL, outer nuclear layer; INL, inner nuclear layer; GCL, ganglion cell layer; N.S., not significant.

near completion of rod death by the onset of cone degeneration (12,13). Relative to these retinas, co-infection with AAV8-sCX3CL1 did not significantly alter ONL thickness (Fig. 5*A* and *B*). This observation demonstrated not only a lack of rod preservation by AAV8-sCX3CL1, but also that cone survival was not secondary to rescue of rods.

We next asked how microglia responded to sCX3CL1 therapy by comparing retinas from *rd1*;Cx3cr1$^{GFP/+}$ (Fig. 5*C*) and *rd10*;Cx3cr1$^{GFP/+}$ (Fig. 5*D*) mice with and without AAV8-sCX3CL1. As use of AAV8-GFP in these animals complicated visualization of GFP-expressing microglia, an analogous AAV8-mCherry virus was generated for control infections. During both the onset and peak of cone degeneration in eyes receiving only AAV8-mCherry, ~40% of retinal microglia could be found in the ONL, indicating continued localization of these cells to the vicinity of cones (Fig. 5*E* and *F*). This percentage remained unchanged with the addition of AAV8-sCX3CL1, arguing against a role of sCX3CL1 in reducing microglial residence in the ONL.

Finally, given upregulation of inflammatory cytokines and complement during the period of non-autonomous cone death, the effect of AAV8-sCX3CL1 on these factors was evaluated by RT-PCR. For the majority of genes tested, including *Il1a*, *Il1b*, *C1qa*, and *Tmem119*, expression levels in the retina were similar in eyes infected with AAV8-GFP or AAV8-GFP plus AAV8-sCX3CL1 (Fig. 5*G*-*J*). The notable exception was *Cd68*, a microglial activation marker which was upregulated with AAV8-sCX3CL1 throughout cone degeneration (30). Collectively, these data challenged the notion that AAV8-sCX3CL1 attenuates complement and inflammatory cytokine activity in the retina. Moreover, they showed that even with massive rod death, microglia in the ONL, and ongoing inflammation in the eye, AAV8-sCX3CL1 was still able to prolong cone survival.

AAV8-sCX3CL1 induces markers of microglial activation

To probe for gene expression changes in microglia that might be brought about by AAV8-sCX3CL1, RNA sequencing (RNA-seq) of retinal microglia from AAV8-sCX3CL1 infected

eyes was performed. Flow cytometry of RP retinas carrying the Cx3cr1^{GFP} transgene indicated that microglia corresponded to a CD11b+ Ly6G/Ly6C- population in the retina (Supplemental Fig. 4), consistent with earlier studies (47,48). Using these cell surface markers, retinal microglia from *rd10* mice infected with AAV8-GFP or AAV8-GFP plus AAV8-sCX3CL1 were sorted at P70 during the peak of cone degeneration. Sorted microglia were a highly purified population, expressing microglia-specific genes, such as *Fcrls, P2ry12*, and *Tmem119*, but not markers for other retinal cell types compared to non-microglia (CD11b- Ly6G/Ly6C- and CD11b- Ly6G/Ly6C+) cells (Supplemental Fig. 5) (49–56).

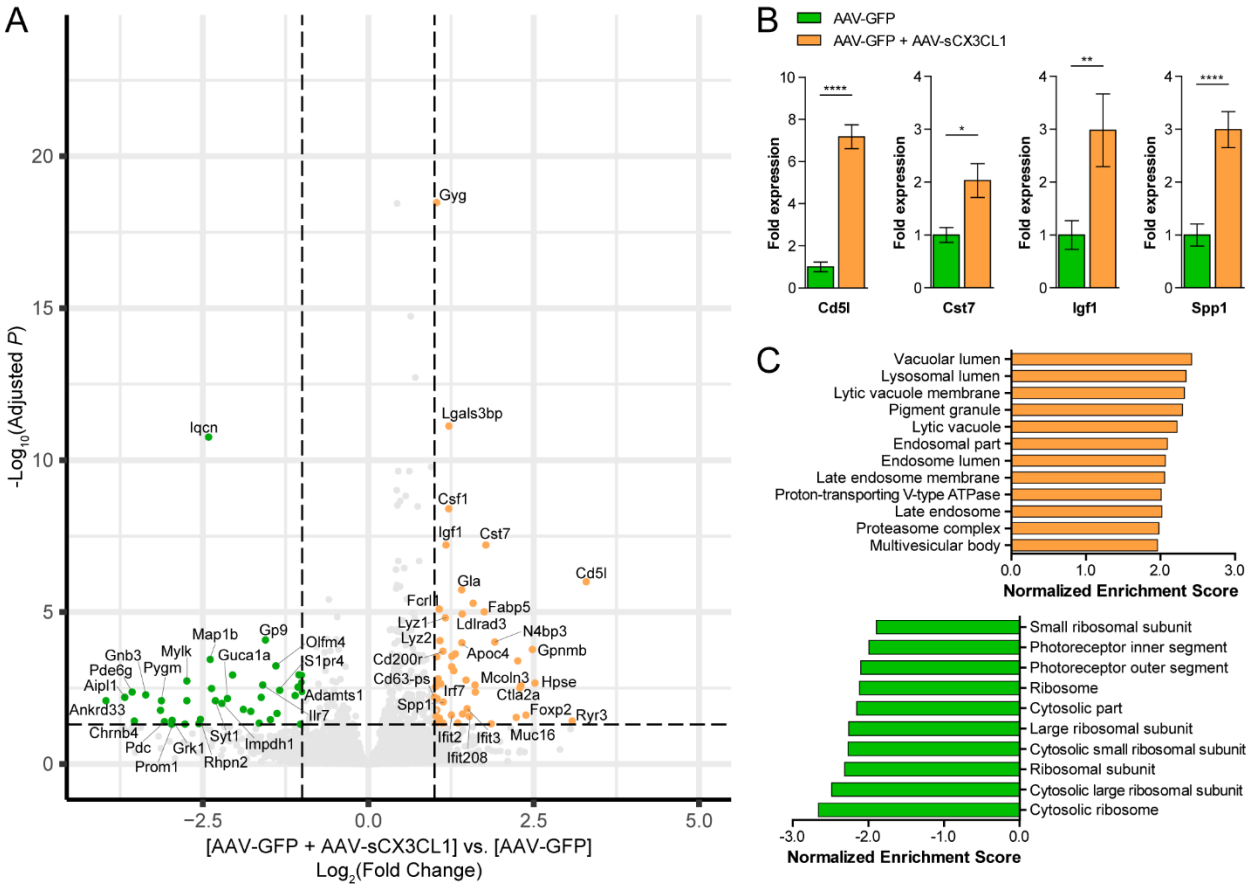

Figure 6. Transcriptional profiling of retinal microglia during cone degeneration with sCX3CL1. (**A**) Volcano plot of upregulated and downregulated genes from P70 *rd10* retinal microglia following infection at P0-P1 with AAV8-GFP or AAV8-GFP plus AAV8-sCX3CL1. Dotted lines indicate adjusted *P*<0.05 and magnitude of fold change ≥2. (**B**) RT-PCR validation of gene expression changes in P70 *rd10* retinal microglia with AAV8-sCX3CL1. (**C**) Gene set enrichment analysis of P70 *rd10* microglia from retinas infected with AAV8-GFP plus AAV8-sCX3CL1 (orange) compared to AAV8-GFP alone (green). Gene sets with family-wise error rate (FWER) <0.05 are displayed. Data shown as mean ± SEM. *n* = 7-8 animals per condition. * *P*<0.05, ** *P*<0.01, **** *P*<0.0001 by two-tailed Student's t-test.

RNA-seq analysis of sorted microglia from P70 *rd10* retinas infected with AAV8-sCX3CL1 demonstrated significant (adjusted $P<0.05$, fold change ≥2) upregulation and downregulation of 50 and 40 genes, respectively (Fig. 6*A*). Four of these expression changes were validated by RT-PCR on independent samples (Fig. 6*B*). Among the genes upregulated with AAV8-sCX3CL1 were known markers of microglial activation during neurodegeneration, including *Cst7*, *Spp1*, *Igf1*, *Csf1*, *Lyz2*, *Cd63-ps*, and *Gpnmb* (57–60). In support of this, gene set enrichment analysis (GSEA) of microglia with AAV8-sCX3CL1 revealed significant enrichment of lysosome components (Fig. 6*C*), a prominent feature of activated microglia (30,34,61). Interestingly, low levels of multiple cone-specific genes such as *Aipl1*, *Chrnb4*, and *Gnb3* were observed in microglia from AAV8-GFP treated retinas (62–64), potentially due to phagocytosis of dying cones or cone fragments. Fewer of these transcripts were detected in microglia from AAV8-sCX3CL1 treated retinas, hinting that sCX3CL1 might affect the digestion of phagocytosed materials.

Normal numbers of microglia are not necessary for cone rescue with AAV8-sCX3CL1

In healthy eyes, CX3CR1, the only known receptor for CX3CL1, is thought to be specifically expressed by microglia (65). This fact and the above RNA-seq data prompted us to ask what effect ablation of microglia might have on cone survival. In addition, we were curious if microglia were necessary for the rescue of cones by AAV8-sCX3CL1. It is possible to pharmacologically deplete microglia using PLX3397, a potent colony stimulating factor 1 receptor (CSF1R) inhibitor (23,66). To this end, *rd1* mice were fed PLX3397, and depletion of retinal microglia was assessed using flow cytometry. PLX3397 treatment led to ~99% depletion of microglia after 30 days (Fig. 7*A* and *B*). To determine if reduction in microglia prolonged cone survival, and to test whether the activity of AAV8-sCX3CL1 in preserving cones required microglia, *rd1* mice were infected with AAV8-GFP with or without AAV8-sCX3CL1 and administered PLX3397 for 30 days during the period of cone degeneration. Depletion of

microglia non-significantly (*P*>0.05) increased cone survival in both conditions (Fig. 7*C* and *D*). Moreover, depletion of microglia did not abrogate the ability of AAV8-sCX3CL1 to rescue cones (*P*<0.0001).

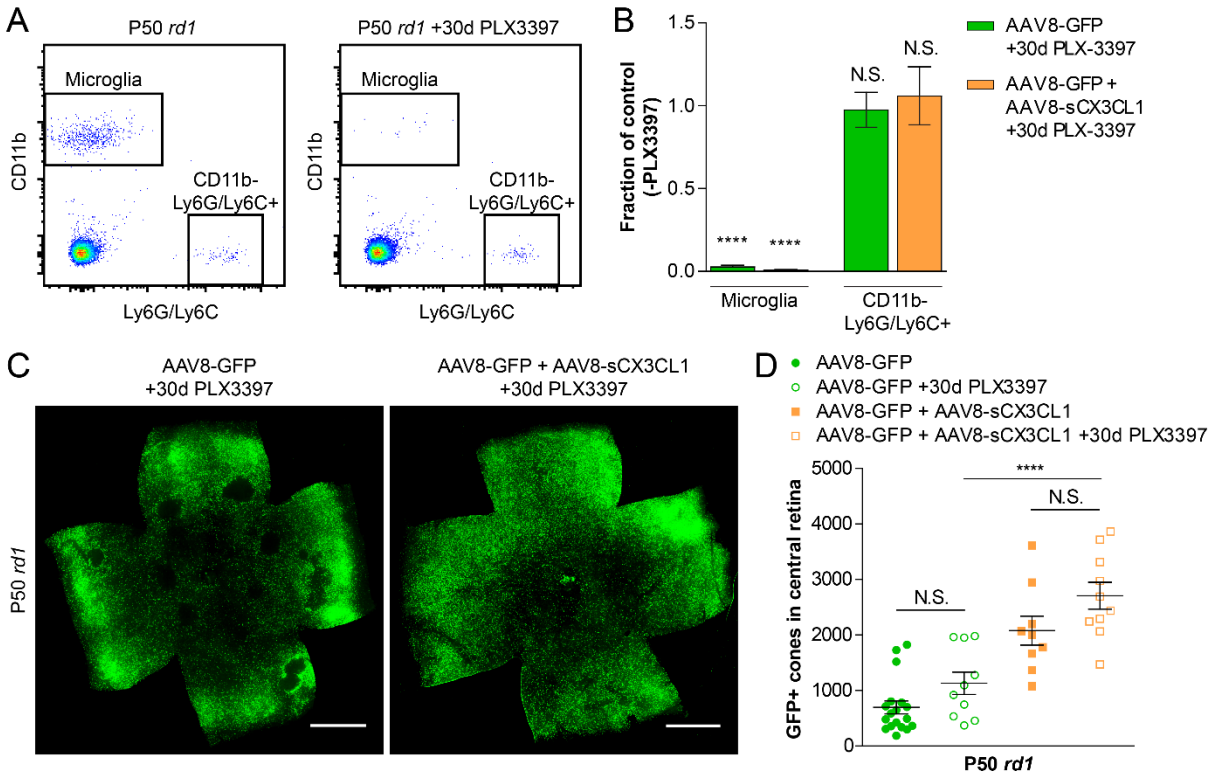

Figure 7. Effect of microglia depletion on AAV8-sCX3CL1 cone rescue. (**A**) Representative flow cytometry gating of microglia (CD11b+ Ly6G/Ly6C-) and CD11b- Ly6G/Ly6C+ populations in P50 *rd1* retinas with or without PLX3397 treatment from P20 to P49. Panels are gated on live cells (DAPI-) following doublet exclusion. (**B**) Fraction of microglia and CD11b- Ly6G/Ly6C+ cells remaining relative to controls in P50 *rd1* retinas infected at P0-P1 with AAV8-GFP alone or AAV8-GFP plus AAV8-sCX3CL1 after 30 days of PLX3397 treatment. Retinas from littermates without PLX3397 treatment were used as controls. (**C**) Flat-mounted P50 *rd1* retinas from PLX3397 treated mice infected with AAV8-GFP or AAV8-GFP plus AAV8-sCX3CL1. Scale bar, 1 mm. (**D**) Quantification of cone survival in the central retina of P50 *rd1* retinas from PLX3397 treated mice infected with AAV8-GFP or AAV8-GFP plus AAV8-sCX3CL1. Data shown as mean ± SEM. *n* = 3-4 animals per condition for (A), *n* = 9-18 animals per condition for (D). **** *P*<0.0001 by two-tailed Student's t-test. N.S., not significant.

Discussion

In this study, we developed a novel gene therapy vector, AAV8-sCX3CL1, that prolonged cone survival in three different RP mouse models and delayed the loss of cone-mediated vision. Preservation of cones with AAV8-sCX3CL1 occurred despite elevated cytokine levels in the retina, and despite the continued presence of microglia in the ONL. Depletion of up

to ~99% of microglia during cone degeneration non-significantly improved cone survival and did not disrupt the rescue effect of AAV8-sCX3CL1. While the mechanism by which AAV8-sCX3CL1 saves cones remains to be elucidated, our findings suggest that sCX3CL1 gene therapy could be beneficial for a wide range of RP patients, and potentially for other patients with inflammatory processes that affect vision or other areas of the CNS.

CX3CL1 is a 373-amino acid protein with a single transmembrane domain that can undergo proteolytic cleavage to release sCX3CL1 into the extracellular environment (38). In the CNS, both fCX3CL1 and sCX3CL1 are primarily produced by neurons and, by binding CX3CR1 on microglia, are thought to regulate key aspects of microglial physiology (67,68). One of the main responsibilities of CX3CL1 in neuron-microglia interactions is to suppress the activation of microglia (69,70). Supporting this notion, exogenous delivery of CX3CL1 has been shown to decrease microglial activation as well as neurological deficits in animal models of Parkinson's disease and stroke (71–73).

Based on these data, we overexpressed CX3CL1 in RP mice with the hope that it would attenuate immune responses in the retina that were perpetuating non-autonomous cone death. Use of sCX3CL1 indeed prolonged cone survival during degeneration, though it did so without reducing inflammation or the number of microglia in the ONL. Interestingly, cone rescue was seen when sCX3CL1 was secreted by the RPE, but not when full-length membrane-bound CX3CL1 was expressed on cones. This result could be due to differences in the level of expression, as the RPE-specific human Best1 promoter is quite strong relative to the human red opsin promoter. Alternatively, it could be that sCX3CL1 acts on other cell types besides microglia and is better able to reach these cells when secreted. In contrast, overexpression of CD200, another repressor of microglial activation (24), failed to rescue cones whether expressed as a sCD200 from the RPE or fCD200 on cones. Of note, we recently reported dose-dependent vector toxicity with certain promoters, including human Best1, resulting in

dysmorphic RPE and mild photoreceptor damage (74). In this study, AAV8-sCX3CL1 containing the human Best1 promoter was nonetheless able to improve cone survival.

Activated microglia are a hallmark of early RP, given their migration into the ONL, production of inflammatory cytokines, and phagocytosis of living photoreceptors (33,34,45). In early RP, rods are degenerating, and these microglia activities are deleterious, as genetic ablation of microglia has been demonstrated to ameliorate rod death (34). Acute retinal detachment, another condition causing photoreceptor loss, is similarly characterized by inflammatory cytokines and phagocytic microglia (75,76). Unlike with early RP, however, removal of microglia during retinal detachment was observed to accelerate photoreceptor degeneration, implying a protective role for activated microglia (76). Here, we found evidence of microglial activation during cone death in RP as illustrated by the presence of microglia in the ONL, and upregulation of *Il1a*, *Tnf*, *C1qa,* and *Cd68*. We hypothesized that, as in early RP, these microglia might be detrimental, and consequently, our goal was to develop AAV vectors capable of suppressing retinal microglial activation. Interestingly, drug-induced depletion of microglia in *rd1* retinas provided evidence for only a slight negative effect of activated microglia on cones; only a small increase in the number of cones was seen with microglia depletion, and this change did not reach statistical significance. One explanation for this could be that while activated microglia in RP do hinder cone survival, they may also provide some benefits. We speculate that one such benefit may be increased clearance of harmful cell debris. By RNA-seq, we detected small amounts of cone-specific RNAs in microglia from AAV8-GFP infected *rd10* retinas, potentially from phagocytosis of cones or cone fragments. Because such RNAs were fewer in microglia from AAV8-sCX3CL1 infected retinas, cone debris might accumulate in control microglia if digestion of these materials cannot keep up with engulfment. Inability of microglia to complete phagocytosis may then trigger the release of factors injurious to cones, akin to the model of “frustrated phagocytosis” experienced by microglia in Alzheimer’s disease (77). As we observed upregulation of lysosomal pathways in microglia with AAV8-sCX3CL1,

these cells may more efficiently digest cone material, alleviating this frustration and favoring cone preservation.

Notably, depletion of up to ~99% of microglia also failed to abrogate AAV8-sCX3CL1 cone rescue. Although this could indicate that sCX3CL1 prolongs cone survival independently of microglia, we cannot rule out the possibility that sCX3CL1 mediated the rescue effect via microglia prior to their depletion. Because AAV8-sCX3CL1 was administered before PLX3397, there may have been enough time for microglia to respond to sCX3CL1 and alter the retinal microenvironment in a manner promoting cone survival. While it normally takes around two months for subretinal AAV8 expression to peak, a small amount of signal can be detected as early as five days post-infection (78). Consistent with this, we did see transcriptional changes in retinal microglia 20 days after delivery of AAV8-sCX3CL1 (data not shown), though it is difficult to interpret the relevance of such changes in delaying cone degeneration. Another scenario could be that only a few microglia are needed for AAV8-sCX3CL1 to save cones. In a recent study by Liddelow et al., depletion of microglia by PLX3397 was unable to eliminate a phenotype in astrocytes induced by microglia (23). Specifically, the authors found that inflammatory cytokines from activated microglia caused astrocytes to damage neurons. Astrocyte neurotoxicity was absent in CSF1R null mice, which are devoid of microglia (79). However, in other strains, neurotoxicity was still observed despite pharmacologically depleting 95% of microglia (23). Thus, it could be that the ~1% of retinal microglia that survive PLX3397 treatment are sufficient to respond to sCX3CL1 and preserve degenerating cones. For these remaining microglia, greater sCX3CL1 signaling per cell may additionally account for the slight additivity of AAV8-sCX3CL1 and microglia depletion on cone rescue.

An alternative model, given how modest the effect of microglia depletion was on cone survival, is that non-autonomous cone death is caused by mechanisms largely independent of microglia (9,13–15). For AAV8-sCX3CL1, the reason for cone rescue might then be due to sCX3CL1 acting on a CX3CR1-expressing cell type other than microglia. This cell type would

have to be external to the retina, since none of the non-microglia cells in our *rd1*;Cx3cr1$^{GFP/+}$ retinas expressed CX3CR1 when analyzed by flow cytometry. Outside of the CNS, CX3CR1 is also present on several immune cell populations, including monocytes, peripheral macrophages, and certain subsets of T cells, natural killer cells, and dendritic cells (35,80). In these populations, one of the roles of CX3CR1 is to mediate a chemotactic response to CX3CL1 (80,81). It is therefore plausible that sCX3CL1 secreted by the RPE might act on one of these cell types in the vascular-rich choroid, perhaps to induce migration into the subretinal space. Future work is needed to examine these possibilities and determine at a molecular level how sCX3CL1 preserves cones. Such information will aid the development of better RP treatments that more specifically target cone degeneration.

In 2017, an AAV vector encoding the RPE65 gene became the first gene therapy to be approved for an inherited retinal disorder (82). Despite this achievement, there are still thousands of retinal disease mutations for which no effective treatment exists (83). Addressing these lesions one by one would be cost-prohibitive and time-consuming, and specifically for RP, rods carrying the mutation have often died by the time of diagnosis (1), making gene correction therapy infeasible. Mutation-independent gene therapy is an alternative approach that, while not curative, may improve vision for a much larger number of patients, including those for whom no causal mutation has been identified. Previously, only two examples of mutation-independent gene therapy have been shown to rescue cones in animal models of RP (84). In 2015, Byrne et al. reported better cone survival and vision in two strains of RP mice with viral-mediated expression of rod-derived cone viability factor (RdCVF), a protein normally secreted from rods that stimulates cones to take up glucose (15,85,86). That same year, our group found that cone numbers and function in three RP mouse lines could be improved with AAV-mediated delivery of antioxidant-based therapy, particularly a master antioxidant transcription factor, NRF2 (13). Here, we demonstrated that AAV8-sCX3CL1 is also a mutation-independent gene therapy capable of saving cones in different types of RP mice. Our results support further assessment of

AAV8-sCX3CL1 in larger RP animal models and highlight its potential to help treat this disease in patients, regardless of their mutation.

Finally, photoreceptor death occurs in other diseases, such as age-related macular degeneration (AMD), the leading cause of blindness in the industrialized world (87). Although AMD pathogenesis is not fully understood, loss of rods typically precedes that of cones (88,89), not unlike non-autonomous cone death in RP. Furthermore, genetic polymorphisms in CX3CR1, the receptor for CX3CL1, have been associated with a higher risk of AMD in patients (90). It would thus be interesting to test if sCX3CL1 can similarly alleviate retinal degeneration in AMD.

Materials and Methods

Animals. CD-1 (#022), *rd1* (FVB/N) (#207), and C57BL/6 (#027) mice were purchased from Charles River Laboratories. Cx3cr1^{GFP} (#005582) (35) and *rd10* (#004297) (27) mice on a C57BL/6 background were purchased from The Jackson Laboratory. Rhodopsin null (*Rho*$^{-/-}$) mice were a gift from Janis Lem (Tufts University, Boston, MA, USA) (42). Animals were subsequently bred and maintained at Harvard Medical School on a 12-hour alternating light and dark cycle. All experimental procedures were approved by the Institutional Animal Care and Use Committee (IACUC) at Harvard University.

Plasmids. The AAV-human red opsin-GFP-WPRE-bGH (AAV8-GFP) vector plasmid was a gift from Botond Roska (Friedrich Miescher Institute for Biomedical Research, Basel, Switzerland) (91) and used the promoter region originally developed by Wang et al. (92). The AAV8-mCherry vector was generated by replacing the GFP coding sequence with that of mCherry flanked by NotI and AgeI restriction sites. AAV8-fCD200 and AAV8-fCX3CL1 were then cloned by digesting AAV8-mCherry with NotI and HindIII restriction enzymes and replacing the mCherry coding sequence with the GCCGCCACC Kozak sequence followed by the full-length mouse cDNA for CD200 (NM_010818.3) or CX3CL1 (NM_009142.3), respectively. A vector utilizing the human Best1 promoter was created by replacing the CMV promoter of the

AAV-CMV-PI-EGFP-WPRE-bGH plasmid, a gift from James M. Wilson (University of Pennsylvania, Philadelphia, PA, USA), with the -540/+38 base pair region of the human Best1 promoter (93). Vector plasmids for AAV8-sCD200 and AAV8-sCX3CL1 were cloned by digesting the AAV-human Best1 promoter vector with NotI and HindIII restriction enzymes and replacing the EGFP coding sequence with the GCCGCCACC Kozak sequence followed by the first 714 base pairs (amino acids 1-238) of CD200 or first 1008 base pairs (amino acids 1-336) of CX3CL1, respectively, followed by a stop codon.

Vector production and purification. Recombinant AAV serotype 8 (AAV8) vectors were generated as previously described (13,94). HEK293T cells were transfected using polyethylenimine with a mixture of the AAV plasmid, rep2/cap8 packaging plasmid, and adenovirus helper plasmid. Seventy-two hours post-transfection, the supernatant was harvested and vector particles precipitated by overnight PEGylation followed by centrifugation. To remove cell debris, vectors were then subjected to centrifugation through an iodixanol gradient. The recovered AAV vectors were washed three times with phosphate-buffered saline (PBS) and concentrated to a final volume of 100-200 µl. The titer of purified vectors was semi-quantitatively determined by staining of viral capsid proteins VP1, VP2, and VP3 using SYPRO Ruby (Molecular Probes) and relating the staining intensity to a standard titered using RT-PCR of genome sequences.

Subretinal injections. All injections were performed on P0-P1 neonatal mice. Following anesthetization of the mouse on ice, the palpebral fissure was carefully cut using a 30-gauge needle and the eye exposed with dull forceps. A glass needle controlled by a FemtoJet microinjector (Eppendorf) was then used to deliver a volume of ~0.25 µl into the subretinal space for all injections. To standardize labeling of cones, AAV8-GFP and AAV8-mCherry were administered at 5 x 10^8 vector genomes (vg) per eye, a dose adequate for infecting >90% of cones in WT retinas (Supplemental Fig. 1). All other vectors were dosed at 1 x 10^9 vg per eye. The subretinal bleb was formed in the inferotemporal quadrant for the right eye and

superotemporal quadrant for the left. Right and left eye injections for each condition were alternated from litter to litter, and no significant difference was found in the number or distribution of GFP-positive cones between right or left eyes injected with the same vectors.

Histology. Enucleated eyes for retinal cross-sections were dissected in PBS. Following removal of the cornea, iris, lens, and ciliary body, the remaining eye cup was fixed in 4% paraformaldehyde for two hours at room temperature, cryoprotected in 10%, 20%, and 30% sucrose in PBS, and embedded in a 1:1 mixture of 30% sucrose in PBS and optimal cutting temperature compound (Tissue-Tek) on dry ice. Frozen eye cups were cut on a Leica CM3050S cryostat (Leica Microsystems) into 50 µm sections for Cx3cr1^{GFP} retinas or 20 µm sections otherwise and stained with 4′,6-diamidino-2-phenylindole (DAPI) (Thermo Fisher Scientific) for five minutes at room temperature before mounting with Fluoromount-G (SouthernBiotech). For flat-mounted retinas, isolated retinas were fixed in 4% paraformaldehyde for 30 minutes at room temperature. Four radial incisions were made to relax the retina into four leaflets, which were flattened onto a microscope slide with the ganglion cell layer facing up using a fine-haired brush. To perform antibody staining of retinal cross-sections or whole retinas, tissues were blocked with 5% goat serum or 5% bovine serum albumin in PBS with 0.1% Triton X-100 for one hour at room temperature, after which tissues were incubated with primary antibodies in block solution at 4°C overnight followed by secondary antibodies in PBS for two hours at room temperature. Primary antibodies included rabbit anti-CX3CL1 (Abcam, ab25088, 1:500) and rhodamine-conjugated peanut agglutinin (PNA) (Vector Laboratories, RL-1072, 1:1000). Goat anti-rabbit Alexa Fluor 594 (Jackson ImmunoResearch, 111-585-144, 1:1000) was used as a secondary antibody.

Image acquisition and analysis. Images of microglia in retinal cross-sections and of flat-mounted retinas were acquired on a Keyence BZ-9000 widefield fluorescent microscope using a 10x air objective. All other images were acquired on a Zeiss LSM710 scanning confocal microscope using a 10x air, 20x air, or 40x oil objective. Image analysis was performed using

ImageJ. To calculate the percentage of microglia in the ONL, a mask was drawn around the ONL following the outlines of DAPI-labeled nuclei. Each microglia was determined to reside in the ONL if 50% or more of its cell body was located within the mask. GFP-positive cones in flat-mounted retinas were quantified using a custom ImageJ module. To indicate the location of the optic nerve head and boundaries of the retina, a line was first drawn by the user from the optic nerve head to the center of the edge of each of the four retinal leaflets as depicted in Supplemental Fig. 2. All subsequent steps were performed by the module without requiring user input. To define the region corresponding to the central retina, the module connected the four aforementioned lines at their midpoints to form a quadrilateral around the optic nerve head. The image then underwent several processing steps to account for areas of uneven fluorescence or overlapping GFP signal, including local background subtraction, watershed segmentation, and particle size filtering. Finally, an automatic threshold was applied, and the number of GFP-positive particles within the quadrilateral was quantified by the module. This value was used to represent the number of GFP-positive cones in the central retina of the sample. The module can be freely downloaded from https://sites.imagej.net/Seankuwang/.

Electroretinography (ERG). *In vivo* ERG recordings were performed and measured using the Espion E3 System (Diagonsys) as previously described (13,95). To minimize inter-animal variation, conditions were tested using right and left eyes of the same animals. Mice were dark-adapted overnight and anesthetized with an intraperitoneal injection of 100 mg/kg ketamine and 10 mg/kg xylazine. Following dilation of the pupils with 1% tropicamide, gold-wire electrodes were applied to the surface of both eyes and hydrated with a drop of lubricating gel (Optixcare). Reference and ground electrodes were placed subcutaneously near the scalp and tail, respectively. The animal was then light-adapted for 12 minutes under a 30 cd/m^2 background light. Upon completion of light adaptation, photopic vision was assessed using multiple flashes of 1, 10, and 100 cd/m^2 light. The average amplitude of the photopic b-wave in

response to each flash intensity was subsequently measured by an observer (Y.X.) blinded to the treatment assignment.

Optomotor assay. Visual acuity was measured using the OptoMotry System (Cerebral Mechanics) as previously described (13,95). Mice were placed on a platform within a virtual-reality chamber in which the spatial frequency of a displayed sine wave grating could be altered using a computer program. A bright background luminance setting was used to saturate rod responses to provide a measure of cone vision. During each test, an observer (P.R.) blinded to the treatment assignment assessed for reflexive head-tracking movements in response to the grating stimulus. Right and left eyes were tested independently using counterclockwise and clockwise gratings, respectively, as only motion in the temporal-to-nasal direction evokes the optomotor response in mice (44). For each eye, the highest spatial frequency at which the animal tracked the grating was determined to be the visual acuity.

RT-PCR. For RT-PCR of whole retinas, freshly dissected retinas were homogenized using a handheld pellet pestle (Kimble Chase) in 350 µl of RLT buffer containing 1% beta-mercaptoethanol. One retina was used per sample. For RT-PCR of microglia, approximately 1000 microglia per retina were sorted into 10 µl of Buffer TCL (Qiagen) to lyse cells, to which 70 µl of RLT buffer containing 1% beta-mercaptoethanol was added. RNA extractions were performed using an RNeasy Micro Kit (Qiagen) followed by cDNA synthesis using the SuperScript III First-Strand Synthesis System (Invitrogen). RT-PCR reactions were conducted in triplicate using the Power SYBR Green PCR Master Mix (Applied Biosystems) on a CFX96 real-time PCR detection system (BioRad) to determine cycle threshold (Ct) values. Expression levels were quantified by normalizing to the housekeeping gene *Gapdh* with fold changes relative to age-matched WT (CD-1 or B6) retinas. *P*-values were calculated using ΔΔCt values. Primers for RT-PCR were designed using PrimerBank (96).

RPE explants. Enucleated eyes were dissected in PBS to remove the cornea, iris, lens, ciliary body, retina, and connective tissue. Four relaxing radial incisions were made to the

remaining RPE-choroid-sclera complex. Each complex was then placed on a 12 mm Millicell cell culture insert (Millipore) resting on 3 mL of prewarmed culture media with the RPE side facing up. Culture media consisted of a 1:1 ratio of DMEM and F-12 supplemented with L-glutamine, B27, N2, and penicillin-streptomycin. Explants were maintained in humidified incubators at 37°C and 5% CO2 for 48 hours, after which the media was collected and assayed for CX3CL1 protein using a commercial ELISA kit (R&D Systems) according to manufacturer's instructions. ELISA reactions were performed in duplicate using 50 µl of media as input.

Flow cytometry and cell sorting. Retinal microglia were isolated using fluorescence-activated cell sorting (FACS) and data analyzed on FlowJo 10 (Tree Star). To dissociate cells, freshly dissected retinas were incubated in 400 µl of cysteine-activated papain solution (Worthington) for 5 minutes at 37ºC, followed by gentle trituration with a micropipette. Dissociated cells were blocked with rat anti-mouse CD16/32 (BD Pharmingen, 1:100) for 5 minutes on ice followed by staining with PE-Cy5-conjugated anti-CD11b (BioLegend, M1/70, 1:200), APC-Cy7-conjugated anti-Ly6G (BioLegend, 1A8, 1:200), and APC-Cy7-conjugated anti-Ly6C (BioLegend, HK1.4, 1:200) for 20 minutes on ice. After washes, cells were resuspended in FACS buffer (2% fetal bovine serum, 2mM EDTA in PBS) containing 0.5 µg/mL DAPI to label non-viable cells and passed through a 40 µm filter. Sorting was performed on a BD FACSAria II using a 70 µm nozzle according to the gating shown in Supplemental Fig. 4.

RNA sequencing of microglia. Eight biological replicates were used per experimental condition. For each retina, 1000 microglia (CD11b+ Ly6G/Ly6C-) were sorted into 10 µl of Buffer TCL (Qiagen) containing 1% beta-mercaptoethanol and immediately frozen on dry ice. For a subset of retinas, 1000 non-microglia cells (CD11b-) were also sorted. Upon collection of all samples, frozen microglia and non-microglia lysates were thawed on wet ice and loaded into a 96-well plate for cDNA library synthesis and sequencing. A modified Smart-Seq2 protocol was performed on samples by the Broad Institute Genomics Platform (97). Libraries from 96 samples with unique barcodes were combined and sequenced on a NextSeq 500 Sequencing

System (Illumina) to an expected coverage of ~6 million reads per sample. Following demultiplexing, reads were subjected to quality control measures and mapped to the GRCm38.p6 reference genome. Reads assigned to each gene were quantified using featureCounts (98), and samples with fewer than 30% assigned reads were excluded from further analysis. Count data were analyzed using DESeq2 to identify differentially expressed genes with an adjusted *P*-value less than 0.05 considered significant (99). Gene set enrichment analysis (GSEA) was performed using GSEA v3.0 software from the Broad Institute under default settings on the GO Cellular Component Ontology collection (580 gene sets) from the Molecular Signatures Database (MSigDB). Gene sets with a family-wise error rate (FWER) less than 0.05 were considered significantly enriched.

Microglia depletion. Microglia were depleted using PLX3397 (SelleckChem), an orally available CSF1R inhibitor. PLX3397 was incorporated into AIN-76A rodent chow (Research Diets) at 290 mg/kg and provided *ad libitum* for 30 days prior to harvesting of the animal on P50.

Statistics. Unpaired two-tailed Student's t-tests were used for comparisons between two groups. For comparisons of three or more groups, a Bonferroni correction was added to the test by multiplying the resulting *P*-value by the number of hypotheses tested. Two-tailed two-way ANOVA was used to analyze ERG, optomotor, and ONL thickness experiments in which the same subjects are compared over a series of conditions or time points. In all cases, a *P*-value less than 0.05 was considered statistically significant.

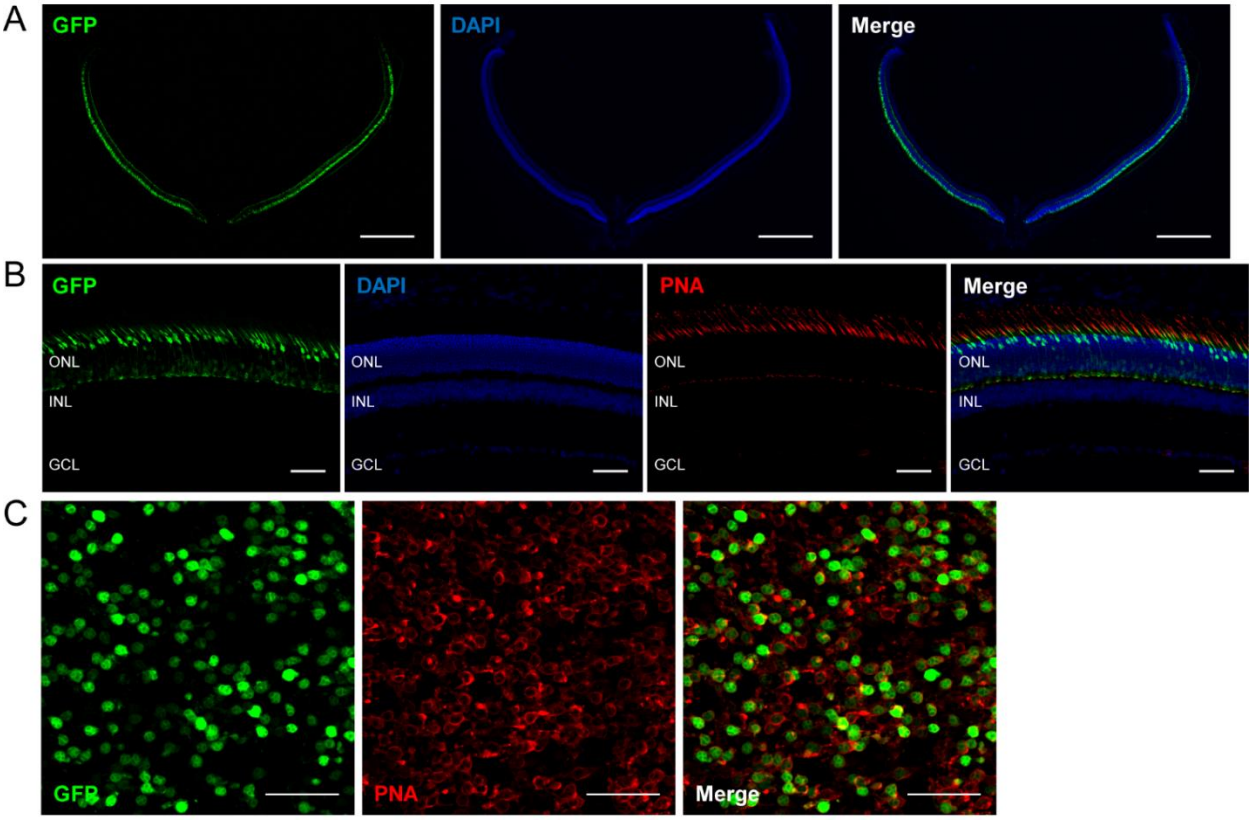

Supplemental Figure 1. Expression of AAV8-GFP in cone photoreceptors. (**A**, **B**) Cross-section from a P50 WT (CD-1) retina infected at P0-P1 with 5 x 10^8 vg of AAV8-GFP and stained with peanut agglutinin lectin (PNA), a marker of the matrix surrounding cone inner and outer segments (100). Scale bars, 500 µm (A), 50 µm (B). (**C**) High-magnification image of a flat-mounted P50 WT retina infected at P0-P1 with AAV8-GFP and stained with PNA. Scale bar, 20 µm.

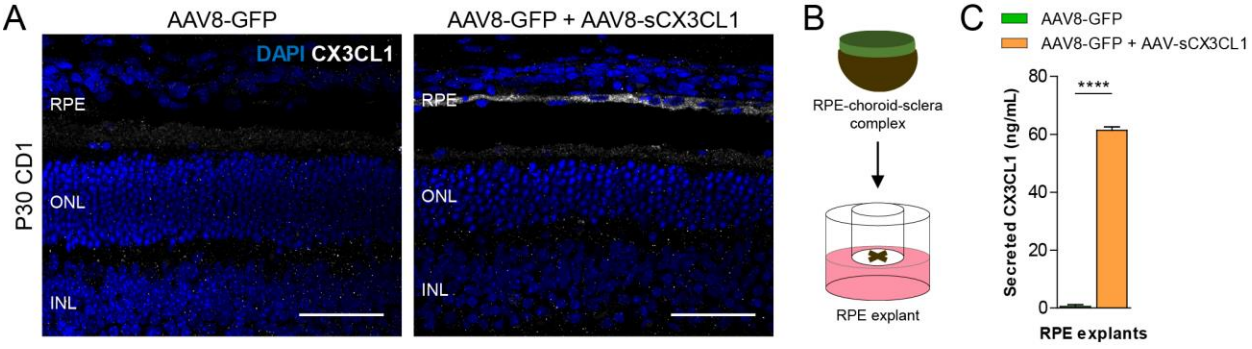

Supplemental Figure 2. Validation of sCX3CL1 overexpression with AAV8-sCX3CL1. (**A**) Cross-section from a P30 WT (CD-1) retina infected at P0-P1 with AAV8-GFP or AAV8-GFP plus AAV8-sCX3CL1 and stained with anti-CX3CL1 antibody. Scale bar, 50 µm. (**B**) Schematic of RPE explant culture. The RPE-choroid-sclera complex was isolated from the rest of the eye and placed on a cell culture insert resting on culture media. (**C**) Quantification of secreted CX3CL1 from P40 WT RPE extracts infected at P0-P1 with AAV8-GFP or AAV8-GFP plus AAV8-sCX3CL1. Media was collected 48 hours after explantation and assayed by ELISA. **** P<0.0001 by two-tailed Student's t-test.

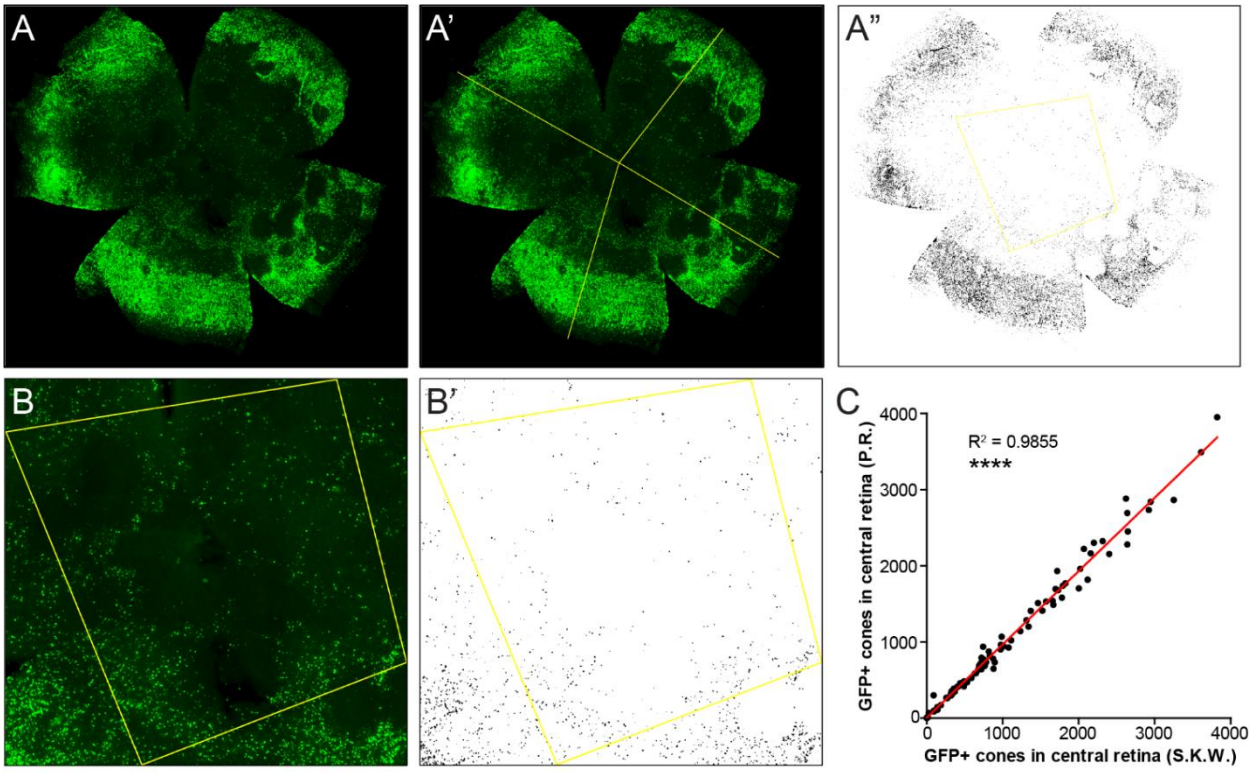

Supplemental Figure 3. Cone quantification methodology. (**A**) Representative image of a P50 flat-mounted RP retina infected at P0-P1 with 5 x 10^8 vg of AAV8-GFP to label cones. (**A'**) A line was drawn by the user from the optic nerve head to the center of the edge of each of the four retinal leaflets. (**A"**) An ImageJ module then subjected the image to automatic processing and thresholding, connected the midpoints of these four lines to form a region defined as the central retina, and quantified the number of GFP-positive cones in the central retina. (**B**, **B'**) Comparison of raw image from a flat-mounted RP retina infected with AAV8-GFP versus the same retina after automatic processing and thresholding. (**C**) Correlation of cone quantification results obtained independently by two authors (S.K.W. and P.R.) using the ImageJ module. Each dot (n = 87) represents a separate retina. **** P<0.0001. R^2 determined using Pearson's correlation analysis.

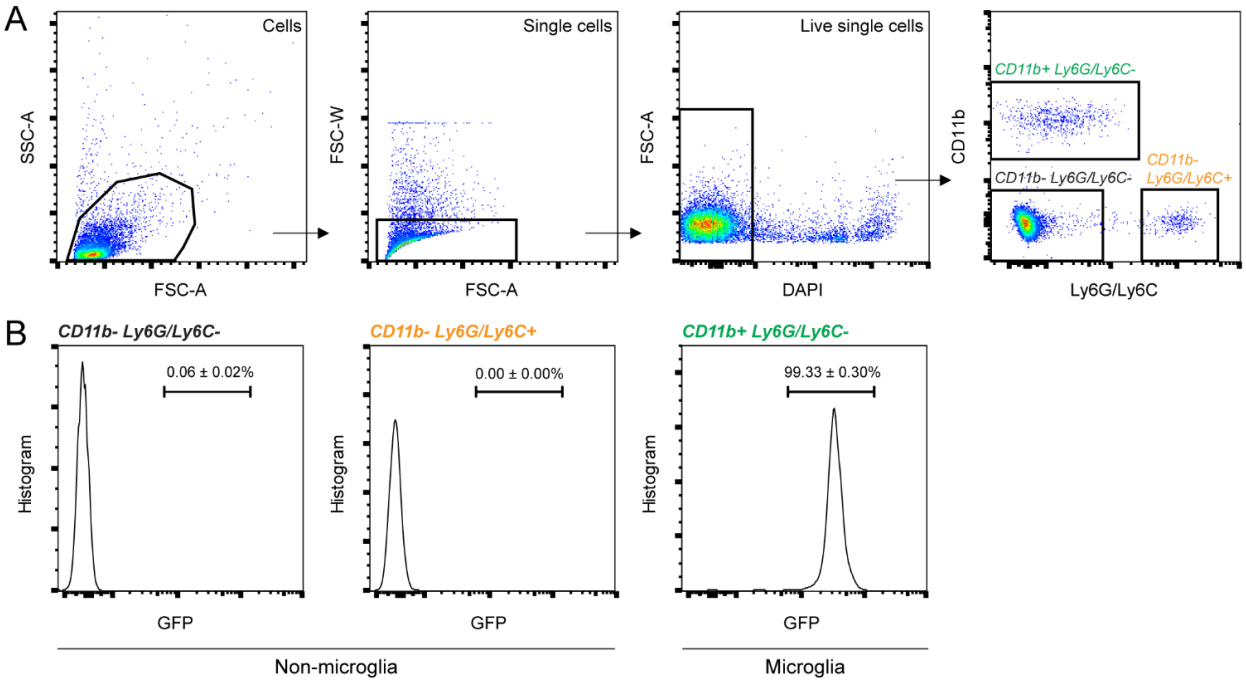

Supplemental Figure 4. Flow cytometry gating of retinal microglia. (A) P35 *rd1*;Cx3cr1$^{GFP/+}$ retinas were dissociated and gated for DAPI-negative single cells, from which three populations were isolated. (**B**) Histograms of Cx3cr1^{GFP} signal in each population. CD11b+ Ly6G/Ly6C- cells were defined as microglia while CD11b- Ly6G/Ly6C- and CD11b- Ly6G/Ly6C+ cells were defined as non-microglia. Data shown as mean ± SEM. *n* = 4 animals per condition.

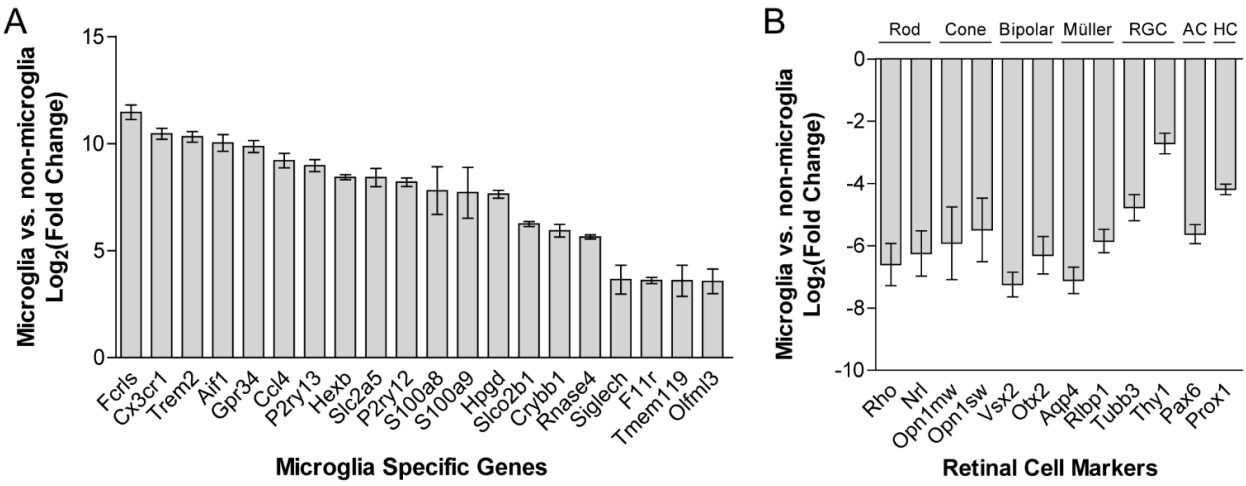

Supplemental Figure 5. Microglia and retinal cell markers in sorted cell populations. (**A**) Comparison of microglia and non-microglia cell populations sorted from *rd10* retinas for expression of 20 microglia-specific genes by RNA-seq (50). (**B**) Comparison of microglia and non-microglia cell populations sorted from *rd10* retinas for expression of indicated retinal cell-type markers by RNA-seq (51–56). Data shown as mean ± SEM. *n* = 24 animals for microglia, *n* = 6 animals for non-microglia. RGC, retinal ganglion cell; AC, amacrine cell; HC, horizontal cell.

References

1. Hartong DT, Berson EL, Dryja TP. Retinitis pigmentosa. Lancet. 2006 Nov 18;368(9549):1795–809.
2. Daiger SP, Sullivan LS, Bowne SJ. Genes and mutations causing retinitis pigmentosa. Clin Genet. 2013 Aug;84(2):132–41.
3. Berson EL. Retinitis pigmentosa: unfolding its mystery. Proc Natl Acad Sci U S A. 1996 May 14;93(10):4526–8.
4. Haim M. Epidemiology of retinitis pigmentosa in Denmark. Acta Ophthalmol Scand Suppl. 2002;(233):1–34.
5. Ali RR, Reichel MB, Thrasher AJ, Levinsky RJ, Kinnon C, Kanuga N, et al. Gene transfer into the mouse retina mediated by an adeno-associated viral vector. Hum Mol Genet. 1996 May;5(5):591–4.
6. Murata T, Kimura H, Sakamoto T, Osusky R, Spee C, Stout TJ, et al. Ocular Gene Therapy: Experimental Studies and Clinical Possibilities. Ophthalmic Res. 1997;29(5):242–51.
7. Maguire AM, Simonelli F, Pierce EA, Pugh EN, Mingozzi F, Bennicelli J, et al. Safety and Efficacy of Gene Transfer for Leber's Congenital Amaurosis. N Engl J Med. 2008 May 22;358(21):2240–8.
8. Sacchetti M, Mantelli F, Merlo D, Lambiase A. Systematic Review of Randomized Clinical Trials on Safety and Efficacy of Pharmacological and Nonpharmacological Treatments for Retinitis Pigmentosa. J Ophthalmol. 2015;2015:737053.
9. Narayan DS, Wood JPM, Chidlow G, Casson RJ. A review of the mechanisms of cone degeneration in retinitis pigmentosa. Acta Ophthalmol. 2016 Dec;94(8):748–54.
10. Wang W, Lee SJ, Scott PA, Lu X, Emery D, Liu Y, et al. Two-Step Reactivation of Dormant Cones in Retinitis Pigmentosa. Cell Rep. 2016 Apr 12;15(2):372–85.
11. Komeima K, Rogers BS, Lu L, Campochiaro PA. Antioxidants reduce cone cell death in a model of retinitis pigmentosa. Proc Natl Acad Sci U S A. 2006 Jul 25;103(30):11300–5.
12. Punzo C, Kornacker K, Cepko CL. Stimulation of the insulin/mTOR pathway delays cone death in a mouse model of retinitis pigmentosa. Nat Neurosci. 2009 Jan;12(1):44–52.
13. Xiong W, Garfinkel AEM, Li Y, Benowitz LI, Cepko CL. NRF2 promotes neuronal survival in neurodegeneration and acute nerve damage. J Clin Invest. 2015;125(4):1433–45.
14. Venkatesh A, Ma S, Le YZ, Hall MN, Rüegg MA, Punzo C. Activated mTORC1 promotes long-term cone survival in retinitis pigmentosa mice. J Clin Invest. 2015 Apr 1;125(4):1446–58.
15. Aït-Ali N, Fridlich R, Millet-Puel G, Clérin E, Delalande F, Jaillard C, et al. Rod-Derived Cone Viability Factor Promotes Cone Survival by Stimulating Aerobic Glycolysis. Cell. 2015 May 7;161(4):817–32.
16. Murakami Y, Matsumoto H, Roh M, Suzuki J, Hisatomi T, Ikeda Y, et al. Receptor interacting protein kinase mediates necrotic cone but not rod cell death in a mouse model of inherited degeneration. Proc Natl Acad Sci. 2012 Sep 4;109(36):14598–603.
17. Zitvogel L, Kepp O, Kroemer G. Decoding Cell Death Signals in Inflammation and Immunity. Cell. 2010 Mar 19;140(6):798–804.
18. Murakami Y, Ikeda Y, Nakatake S, Miller JW, Vavvas DG, Sonoda KH, et al. Necrotic cone photoreceptor cell death in retinitis pigmentosa. Cell Death Dis. 2015 Dec 31;6(12):e2038.
19. Silverman SM, Wong WT. Microglia in the Retina: Roles in Development, Maturity, and Disease. Annu Rev Vis Sci. 2018 Sep 15;4(1):45–77.
20. Salter MW, Stevens B. Microglia emerge as central players in brain disease. Nat Med. 2017 Sep 8;23(9):1018–27.
21. Block ML, Hong J-S. Microglia and inflammation-mediated neurodegeneration: Multiple triggers with a common mechanism. Prog Neurobiol. 2005 Jun;76(2):77–98.
22. Lynch MA. The Multifaceted Profile of Activated Microglia. Mol Neurobiol. 2009 Oct 23;40(2):139–56.

23. Liddelow SA, Guttenplan KA, Clarke LE, Bennett FC, Bohlen CJ, Schirmer L, et al. Neurotoxic reactive astrocytes are induced by activated microglia. Nature. 2017 Jan 18;541(7638):481–7.
24. Hoek RM, Ruuls SR, Murphy CA, Wright GJ, Goddard R, Zurawski SM, et al. Down-regulation of the macrophage lineage through interaction with OX2 (CD200). Science. 2000 Dec 1;290(5497):1768–71.
25. Biber K, Neumann H, Inoue K, Boddeke HWGM. Neuronal 'On' and 'Off' signals control microglia. Trends Neurosci. 2007 Nov;30(11):596–602.
26. Cardona AE, Pioro EP, Sasse ME, Kostenko V, Cardona SM, Dijkstra IM, et al. Control of microglial neurotoxicity by the fractalkine receptor. Nat Neurosci. 2006 Jul 18;9(7):917–24.
27. Chang B, Hawes NL, Hurd RE, Davisson MT, Nusinowitz S, Heckenlively JR. Retinal degeneration mutants in the mouse. Vision Res. 2002 Feb;42(4):517–25.
28. Pennesi ME, Michaels K V., Magee SS, Maricle A, Davin SP, Garg AK, et al. Long-Term Characterization of Retinal Degeneration in *rd1* and *rd10* Mice Using Spectral Domain Optical Coherence Tomography. Investig Opthalmology Vis Sci. 2012 Jul 10;53(8):4644.
29. Bennett ML, Bennett FC, Liddelow SA, Ajami B, Zamanian JL, Fernhoff NB, et al. New tools for studying microglia in the mouse and human CNS. Proc Natl Acad Sci. 2016 Mar 22;113(12):E1738–46.
30. Bodea L-G, Wang Y, Linnartz-Gerlach B, Kopatz J, Sinkkonen L, Musgrove R, et al. Neurodegeneration by activation of the microglial complement-phagosome pathway. J Neurosci. 2014 Jun 18;34(25):8546–56.
31. Carter-Dawson LD, Lavail MM. Rods and cones in the mouse retina. I. Structural analysis using light and electron microscopy. J Comp Neurol. 1979 Nov 15;188(2):245–62.
32. Curcio CA, Sloan KR, Kalina RE, Hendrickson AE. Human photoreceptor topography. J Comp Neurol. 1990 Feb 22;292(4):497–523.
33. Peng B, Xiao J, Wang K, So K-F, Tipoe GL, Lin B. Suppression of Microglial Activation Is Neuroprotective in a Mouse Model of Human Retinitis Pigmentosa. J Neurosci. 2014 Jun 11;34(24):8139–50.
34. Zhao L, Zabel MK, Wang X, Ma W, Shah P, Fariss RN, et al. Microglial phagocytosis of living photoreceptors contributes to inherited retinal degeneration. EMBO Mol Med. 2015 Sep;7(9):1179–97.
35. Jung S, Aliberti J, Graemmel P, Sunshine MJ, Kreutzberg GW, Sher A, et al. Analysis of fractalkine receptor CX(3)CR1 function by targeted deletion and green fluorescent protein reporter gene insertion. Mol Cell Biol. 2000 Jun;20(11):4106–14.
36. Li Q, Timmers AM, Guy J, Pang J, Hauswirth WW. Cone-specific expression using a human red opsin promoter in recombinant AAV. Vision Res. 2008 Feb;48(3):332–8.
37. Wong KK, Zhu F, Khatri I, Huo Q, Spaner DE, Gorczynski RM. Characterization of CD200 Ectodomain Shedding. Kanellopoulos J, editor. PLoS One. 2016 Apr 25;11(4):e0152073.
38. Bazan JF, Bacon KB, Hardiman G, Wang W, Soo K, Rossi D, et al. A new class of membrane-bound chemokine with a CX3C motif. Nature. 1997 Feb 13;385(6617):640–4.
39. Young RW. The renewal of photoreceptor cell outer segments. J Cell Biol. 1967 Apr;33(1):61–72.
40. Sung CH, Davenport CM, Hennessey JC, Maumenee IH, Jacobson SG, Heckenlively JR, et al. Rhodopsin mutations in autosomal dominant retinitis pigmentosa. Proc Natl Acad Sci U S A. 1991 Aug 1;88(15):6481–5.
41. Gargini C, Terzibasi E, Mazzoni F, Strettoi E. Retinal organization in the retinal degeneration 10 (rd10) mutant mouse: A morphological and ERG study. J Comp Neurol. 2007 Jan 10;500(2):222–38.
42. Lem J, Krasnoperova N V, Calvert PD, Kosaras B, Cameron DA, Nicolò M, et al. Morphological, physiological, and biochemical changes in rhodopsin knockout mice. Proc Natl Acad Sci U S A. 1999 Jan 19;96(2):736–41.
43. Prusky GT, Alam NM, Beekman S, Douglas RM. Rapid Quantification of Adult and Developing Mouse Spatial Vision Using a Virtual Optomotor System. Investig Opthalmology Vis Sci. 2004 Dec

1;45(12):4611.

44. Douglas RM, Alam NM, Silver BD, McGill TJ, Tschetter WW, Prusky GT. Independent visual threshold measurements in the two eyes of freely moving rats and mice using a virtual-reality optokinetic system. Vis Neurosci. 2005 Sep 6;22(5):677–84.
45. Zabel MK, Zhao L, Zhang Y, Gonzalez SR, Ma W, Wang X, et al. Microglial phagocytosis and activation underlying photoreceptor degeneration is regulated by CX3CL1-CX3CR1 signaling in a mouse model of retinitis pigmentosa. Glia. 2016 Sep;64(9):1479–91.
46. Yu DY, Cringle SJ, Su EN, Yu PK. Intraretinal oxygen levels before and after photoreceptor loss in the RCS rat. Invest Ophthalmol Vis Sci. 2000 Nov;41(12):3999–4006.
47. Liyanage SE, Gardner PJ, Ribeiro J, Cristante E, Sampson RD, Luhmann UFO, et al. Flow cytometric analysis of inflammatory and resident myeloid populations in mouse ocular inflammatory models. Exp Eye Res. 2016;151:160–70.
48. Murinello S, Moreno SK, Macauley MS, Sakimoto S, Westenskow PD, Friedlander M. Assessing Retinal Microglial Phagocytic Function In Vivo Using a Flow Cytometry-based Assay. J Vis Exp. 2016;(116).
49. Butovsky O, Jedrychowski MP, Moore CS, Cialic R, Lanser AJ, Gabriely G, et al. Identification of a unique TGF-β–dependent molecular and functional signature in microglia. Nat Neurosci. 2014 Jan 8;17(1):131–43.
50. Hickman SE, Kingery ND, Ohsumi TK, Borowsky ML, Wang L, Means TK, et al. The microglial sensome revealed by direct RNA sequencing. Nat Neurosci. 2013 Dec 27;16(12):1896–905.
51. Akimoto M, Cheng H, Zhu D, Brzezinski JA, Khanna R, Filippova E, et al. Targeting of GFP to newborn rods by Nrl promoter and temporal expression profiling of flow-sorted photoreceptors. Proc Natl Acad Sci U S A. 2006 Mar 7;103(10):3890–5.
52. Shekhar K, Lapan SW, Whitney IE, Tran NM, Macosko EZ, Kowalczyk M, et al. Comprehensive Classification of Retinal Bipolar Neurons by Single-Cell Transcriptomics. Cell. 2016 Aug 25;166(5):1308-1323.e30.
53. Roesch K, Jadhav AP, Trimarchi JM, Stadler MB, Roska B, Sun BB, et al. The transcriptome of retinal Müller glial cells. J Comp Neurol. 2008 Jul 10;509(2):225–38.
54. Chintalapudi SR, Patel NN, Goldsmith ZK, Djenderedjian L, Wang X Di, Marion TN, et al. Isolation of Primary Murine Retinal Ganglion Cells (RGCs) by Flow Cytometry. J Vis Exp. 2017 Jul 5;(125):e55785.
55. Cherry TJ, Trimarchi JM, Stadler MB, Cepko CL. Development and diversification of retinal amacrine interneurons at single cell resolution. Proc Natl Acad Sci U S A. 2009 Jun 9;106(23):9495–500.
56. Dyer MA, Livesey FJ, Cepko CL, Oliver G. Prox1 function controls progenitor cell proliferation and horizontal cell genesis in the mammalian retina. Nat Genet. 2003 May 14;34(1):53–8.
57. Keren-Shaul H, Spinrad A, Weiner A, Matcovitch-Natan O, Dvir-Szternfeld R, Ulland TK, et al. A Unique Microglia Type Associated with Restricting Development of Alzheimer's Disease. Cell. 2017 Jun 15;169(7):1276-1290.e17.
58. Song WM, Joshita S, Zhou Y, Ulland TK, Gilfillan S, Colonna M. Humanized TREM2 mice reveal microglia-intrinsic and -extrinsic effects of R47H polymorphism. J Exp Med. 2018 Mar 5;215(3):745–60.
59. Chiu IM, Morimoto ETA, Goodarzi H, Liao JT, O'Keeffe S, Phatnani HP, et al. A neurodegeneration-specific gene-expression signature of acutely isolated microglia from an amyotrophic lateral sclerosis mouse model. Cell Rep. 2013 Jul 25;4(2):385–401.
60. Iaccarino HF, Singer AC, Martorell AJ, Rudenko A, Gao F, Gillingham TZ, et al. Gamma frequency entrainment attenuates amyloid load and modifies microglia. Nature. 2016;540(7632):230–5.
61. Neumann H, Kotter MR, Franklin RJM. Debris clearance by microglia: an essential link between degeneration and regeneration. Brain. 2009 Feb;132(Pt 2):288–95.
62. Iribarne M, Nishiwaki Y, Nakamura S, Araragi M, Oguri E, Masai I. Aipl1 is required for cone photoreceptor function and survival through the stability of Pde6c and Gc3 in zebrafish. Sci Rep.

2017 Dec 5;7(1):45962.

63. Decembrini S, Martin C, Sennlaub F, Chemtob S, Biel M, Samardzija M, et al. Cone Genesis Tracing by the Chrnb4 -EGFP Mouse Line: Evidences of Cellular Material Fusion after Cone Precursor Transplantation. Mol Ther. 2017 Mar 1;25(3):634–53.
64. Tummala H, Ali M, Getty P, Hocking PM, Burt DW, Inglehearn CF, et al. Mutation in the Guanine Nucleotide–Binding Protein β-3 Causes Retinal Degeneration and Embryonic Mortality in Chickens. Investig Opthalmology Vis Sci. 2006 Nov 1;47(11):4714.
65. Combadière C, Feumi C, Raoul W, Keller N, Rodéro M, Pézard A, et al. CX3CR1-dependent subretinal microglia cell accumulation is associated with cardinal features of age-related macular degeneration. J Clin Invest. 2007 Oct;117(10):2920–8.
66. Elmore MRP, Najafi AR, Koike MA, Dagher NN, Spangenberg EE, Rice RA, et al. Colony-stimulating factor 1 receptor signaling is necessary for microglia viability, unmasking a microglia progenitor cell in the adult brain. Neuron. 2014 Apr 16;82(2):380–97.
67. Paolicelli RC, Bisht K, Tremblay M-Ã. Fractalkine regulation of microglial physiology and consequences on the brain and behavior. Front Cell Neurosci. 2014 May 13;8:129.
68. Lauro C, Catalano M, Trettel F, Limatola C. Fractalkine in the nervous system: neuroprotective or neurotoxic molecule? Ann N Y Acad Sci. 2015 Sep;1351(1):141–8.
69. Zujovic V, Benavides J, Vigé X, Carter C, Taupin V. Fractalkine modulates TNF-alpha secretion and neurotoxicity induced by microglial activation. Glia. 2000 Feb 15;29(4):305–15.
70. Mizuno T, Kawanokuchi J, Numata K, Suzumura A. Production and neuroprotective functions of fractalkine in the central nervous system. Brain Res. 2003 Jul 25;979(1–2):65–70.
71. Nash KR, Moran P, Finneran DJ, Hudson C, Robinson J, Morgan D, et al. Fractalkine over expression suppresses α-synuclein-mediated neurodegeneration. Mol Ther. 2015 Jan;23(1):17–23.
72. Pabon MM, Bachstetter AD, Hudson CE, Gemma C, Bickford PC. CX3CL1 reduces neurotoxicity and microglial activation in a rat model of Parkinson's disease. J Neuroinflammation. 2011 Jan 25;8(1):9.
73. Cipriani R, Villa P, Chece G, Lauro C, Paladini A, Micotti E, et al. CX3CL1 is neuroprotective in permanent focal cerebral ischemia in rodents. J Neurosci. 2011 Nov 9;31(45):16327–35.
74. Xiong W, Wu DM, Xue Y, Wang SK, Chung MJ, Ji X, et al. AAV cis-regulatory sequences are correlated with ocular toxicity. Proc Natl Acad Sci U S A. 2019 Mar 4;116(12):5785–94.
75. Nakazawa T, Matsubara A, Noda K, Hisatomi T, She H, Skondra D, et al. Characterization of cytokine responses to retinal detachment in rats. Mol Vis. 2006 Aug 7;12:867–78.
76. Okunuki Y, Mukai R, Pearsall EA, Klokman G, Husain D, Park D-H, et al. Microglia inhibit photoreceptor cell death and regulate immune cell infiltration in response to retinal detachment. Proc Natl Acad Sci U S A. 2018;115(27):E6264–73.
77. Sokolowski JD, Mandell JW. Phagocytic clearance in neurodegeneration. Am J Pathol. 2011 Apr;178(4):1416–28.
78. Natkunarajah M, Trittibach P, McIntosh J, Duran Y, Barker SE, Smith AJ, et al. Assessment of ocular transduction using single-stranded and self-complementary recombinant adeno-associated virus serotype 2/8. Gene Ther. 2008 Mar 15;15(6):463–7.
79. Ginhoux F, Greter M, Leboeuf M, Nandi S, See P, Gokhan S, et al. Fate Mapping Analysis Reveals That Adult Microglia Derive from Primitive Macrophages. Science. 2010 Nov 5;330(6005):841–5.
80. Imai T, Hieshima K, Haskell C, Baba M, Nagira M, Nishimura M, et al. Identification and molecular characterization of fractalkine receptor CX3CR1, which mediates both leukocyte migration and adhesion. Cell. 1997 Nov 14;91(4):521–30.
81. Haskell CA, Cleary MD, Charo IF. Unique Role of the Chemokine Domain of Fractalkine in Cell Capture. J Biol Chem. 2000 Nov 3;275(44):34183–9.
82. Russell S, Bennett J, Wellman JA, Chung DC, Yu Z-F, Tillman A, et al. Efficacy and safety of voretigene neparvovec (AAV2-hRPE65v2) in patients with RPE65 -mediated inherited retinal

dystrophy: a randomised, controlled, open-label, phase 3 trial. Lancet. 2017 Aug 26;390(10097):849–60.

83. Ran X, Cai W-J, Huang X-F, Liu Q, Lu F, Qu J, et al. “RetinoGenetics”: a comprehensive mutation database for genes related to inherited retinal degeneration. Database (Oxford). 2014;2014.
84. Fortuny C, Flannery JG. Mutation-Independent Gene Therapies for Rod-Cone Dystrophies. Adv Exp Med Biol. 2018;1074:75–81.
85. Byrne LC, Dalkara D, Luna G, Fisher SK, Clérin E, Sahel J-A, et al. Viral-mediated RdCVF and RdCVFL expression protects cone and rod photoreceptors in retinal degeneration. J Clin Invest. 2015 Jan 2;125(1):105–16.
86. Léveillard T, Mohand-Saïd S, Lorentz O, Hicks D, Fintz A-C, Clérin E, et al. Identification and characterization of rod-derived cone viability factor. Nat Genet. 2004 Jul 27;36(7):755–9.
87. Pennington KL, DeAngelis MM. Epidemiology of age-related macular degeneration (AMD): associations with cardiovascular disease phenotypes and lipid factors. Eye Vis (London, England). 2016;3:34.
88. Curcio CA, Medeiros NE, Millican CL. Photoreceptor loss in age-related macular degeneration. Invest Ophthalmol Vis Sci. 1996 Jun;37(7):1236–49.
89. Shelley EJ, Madigan MC, Natoli R, Penfold PL, Provis JM. Cone Degeneration in Aging and Age-Related Macular Degeneration. Arch Ophthalmol. 2009 Apr 1;127(4):483.
90. Chan C-C, Tuo J, Bojanowski CM, Csaky KG, Green WR. Detection of CX3CR1 single nucleotide polymorphism and expression on archived eyes with age-related macular degeneration. Histol Histopathol. 2005;20(3):857–63.
91. Busskamp V, Duebel J, Balya D, Fradot M, Viney TJ, Siegert S, et al. Genetic Reactivation of Cone Photoreceptors Restores Visual Responses in Retinitis Pigmentosa. Science. 2010 Jul 23;329(5990):413–7.
92. Wang Y, Macke JP, Merbs SL, Zack DJ, Klaunberg B, Bennett J, et al. A locus control region adjacent to the human red and green visual pigment genes. Neuron. 1992 Sep;9(3):429–40.
93. Esumi N, Oshima Y, Li Y, Campochiaro PA, Zack DJ. Analysis of the *VMD2* Promoter and Implication of E-box Binding Factors in Its Regulation. J Biol Chem. 2004 Apr 30;279(18):19064–73.
94. Grieger JC, Choi VW, Samulski RJ. Production and characterization of adeno-associated viral vectors. Nat Protoc. 2006 Nov;1(3):1412–28.
95. Xue Y, Shen SQ, Jui J, Rupp AC, Byrne LC, Hattar S, et al. CRALBP supports the mammalian retinal visual cycle and cone vision. J Clin Invest. 2015 Feb 2;125(2):727–38.
96. Wang X, Spandidos A, Wang H, Seed B. PrimerBank: a PCR primer database for quantitative gene expression analysis, 2012 update. Nucleic Acids Res. 2012 Jan 1;40(D1):D1144–9.
97. Picelli S, Björklund ÅK, Faridani OR, Sagasser S, Winberg G, Sandberg R. Smart-seq2 for sensitive full-length transcriptome profiling in single cells. Nat Methods. 2013 Nov 22;10(11):1096–8.
98. Liao Y, Smyth GK, Shi W. featureCounts: an efficient general purpose program for assigning sequence reads to genomic features. Bioinformatics. 2014 Apr 1;30(7):923–30.
99. Anders S, Huber W. Differential expression analysis for sequence count data. Genome Biol. 2010;11(10):R106.
100. Kawano K, Uehara F, Sameshima M, Ohba N. Binding sites of peanut agglutinin in mammalian retina. Jpn J Ophthalmol. 1984;28(3):205–14.

Chapter 3: Modulation of microglia by TGF-β1 as a generic therapy for retinitis pigmentosa

Abstract

As discussed in Chapter 2, retinitis pigmentosa (RP) is a genetically heterogenous group of eye diseases in which initial degeneration of rods triggers secondary degeneration of cones, leading to significant loss of daylight, color, and high-acuity vision. Gene complementation with adeno-associated viral (AAV) vectors is one strategy to treat RP. Its implementation faces substantial challenges, however – e.g., the tremendous diversity of causal mutations. Gene therapy targeting secondary cone degeneration is an alternative approach that could provide a much-needed generic treatment for many RP patients. Here, we show that microglia are required for the upregulation of potentially neurotoxic inflammatory factors during the period of cone degeneration in RP, creating conditions that might contribute to cone dysfunction and death. To ameliorate the effects of such factors, we used AAV vectors to express isoforms of the anti-inflammatory cytokine transforming growth factor-beta (TGF-β). AAV-mediated delivery of TGF-β1 rescued degenerating cones in three mouse models of RP carrying different pathogenic mutations. Treatment with TGF-β1 protected vision, as measured by two behavioral assays, and could be pharmacologically disrupted by either depleting microglia or blocking the TGF-β receptors. Our results suggest that TGF-β1 may be broadly beneficial for patients with cone degeneration, and potentially other forms of neurodegeneration, through a pathway dependent upon microglia.

Contributions

Sean K. Wang[1], Yunlu Xue[1], Constance L. Cepko[1,2]

[1] Departments of Genetics and Ophthalmology, Harvard Medical School, Boston, MA 02115, USA

[2] Howard Hughes Medical Institute, Chevy Chase, MD 20815, USA

S.K.W. and C.L.C. conceived the study; S.K.W., Y.X., and C.L.C. designed research; S.K.W. and Y.X. performed experiments and analyzed data; S.K.W. and C.L.C. wrote the paper.

Note: This work has been submitted for publication and is currently in revision at the *Journal of Clinical Investigation*.

Introduction

As discussed in Chapter 2, retinitis pigmentosa (RP) is a genetically heterogenous group of eye diseases that causes progressive loss of vision due to the dysfunction and degeneration of photoreceptors. Worldwide, the condition affects an estimated two million people, with thousands of pathogenic mutations identified to date spanning at least 80 different genes (1). In RP, there is early death of rods, the photoreceptors needed for vision in dim light, leading to difficulty with night vision typically by adolescence (2,3). Rod degeneration is then followed by the dysfunction and death of cones, the cells essential for daylight, color, and high-acuity vision, loss of which can eventually result in blindness (3,4). The pathogenesis of cone degeneration in RP is not understood, in part due to the fact that causal mutations are often exclusively expressed in rods, suggesting that cone death may be driven by a set of converging mechanisms independent of the genetic lesion (4). Despite ongoing efforts to characterize these mechanisms, there are currently no effective interventions to halt primary rod degeneration or secondary cone degeneration in patients with RP (5,6).

One proposed treatment for RP and other inherited retinal diseases (IRDs) is the use of gene therapy to introduce an allele that can complement the mutation. This strategy recently led to the first commercial gene therapy for an IRD and has tremendous therapeutic promise (7,8). Nonetheless, its implementation for RP faces several key challenges. Specifically, developing a gene therapy and clinical trial for each disease gene in RP will be logistically difficult considering the large number of genes to target, but the limited number of individuals with any given mutation (1). Because RP may go undiagnosed until the onset of night blindness (3), patients might also not have sufficient rods for correction of the genetic lesion. In addition to these obstacles, RP due to autosomal dominant or unidentified mutations, which together comprise one-third of cases (9), is not amenable to gene complementation and thus requires an alternative approach. To address these challenges, we and others have focused instead on the development of gene therapy that targets secondary cone degeneration (10–12), the process

ultimately responsible for loss of quality of life in RP. Such therapies, if successful, would provide a much-needed and broadly applicable treatment option for the many patients with RP for whom gene therapy is otherwise infeasible.

Microglia are the resident immune cells of the retina and central nervous system (CNS). In response to infection or tissue damage, they can become activated, a state characterized by changes in microglial morphology, phagocytosis, and cytokine production (13,14). Excessive microglial activation has been implicated in virtually every neurodegenerative disorder (13–15), including RP, in which activated microglia in the retina have been shown to phagocytose photoreceptors (16). During primary rod degeneration in RP, activated microglia appear to be harmful as ablating these cells or suppressing their activation have been reported to enhance rod survival (16,17). However, how microglia contribute to secondary cone degeneration is less clear. In a previous study of cone degeneration in RP, we overexpressed soluble CX3CL1 (fractalkine), a secreted molecule thought to regulate activation of microglia through a receptor on their surface (12). While soluble fractalkine prolonged cone survival and function in RP mouse models, it surprisingly did not require microglia to do so. In the current study, we further addressed the role of microglia in cone death by overexpressing different isoforms of transforming growth factor beta (TGF-β), an anti-inflammatory cytokine known to inhibit microglial activation (18,19). Using three mouse models of RP, we found that TGF-β1 was able to protect degenerating cones and save vision via a mechanism that required both microglia and TGF-β receptor signaling. Our data support the application of TGF-β1 as a generic therapy for patients with RP and highlight the therapeutic potential of modulating microglia to treat neurodegenerative conditions.

Results and Discussion

To examine the effects of microglia during secondary cone degeneration, mice were treated with PLX5622, a potent colony stimulating factor 1 receptor (CSF1R) inhibitor that

selectively eliminates microglia (20). In the *rd1* mouse line, the most widely used animal model of RP (21), PLX5622 treatment for 20 days depleted ~99% of retinal microglia (Fig. 1*A-D*) without affecting peripheral immune populations, such as circulating monocytes or peritoneal macrophages (Supplemental Fig. 1). We previously found that during secondary cone degeneration, there is persistent upregulation in the retina of *Tmem119*, a marker for microglia (22), as well as *Il1a*, *C1qa*, and *Tnf* (12), inflammatory factors that have been shown to induce neurotoxicity both *in vitro* and *in vivo* (15,23). Here, we confirmed these findings (Fig. 1*E*) and sought to determine if microglia were not just correlated with, but responsible for the upregulation of inflammatory genes. RT-PCR performed on retinas from *rd1* mice with or without PLX5622 treatment demonstrated that increased expression of *Il1a*, *C1qa*, and *Tnf* were abolished following microglia depletion (Fig. 1*E*). We thus concluded that microglia play a causal role in retinal inflammation during secondary cone degeneration.

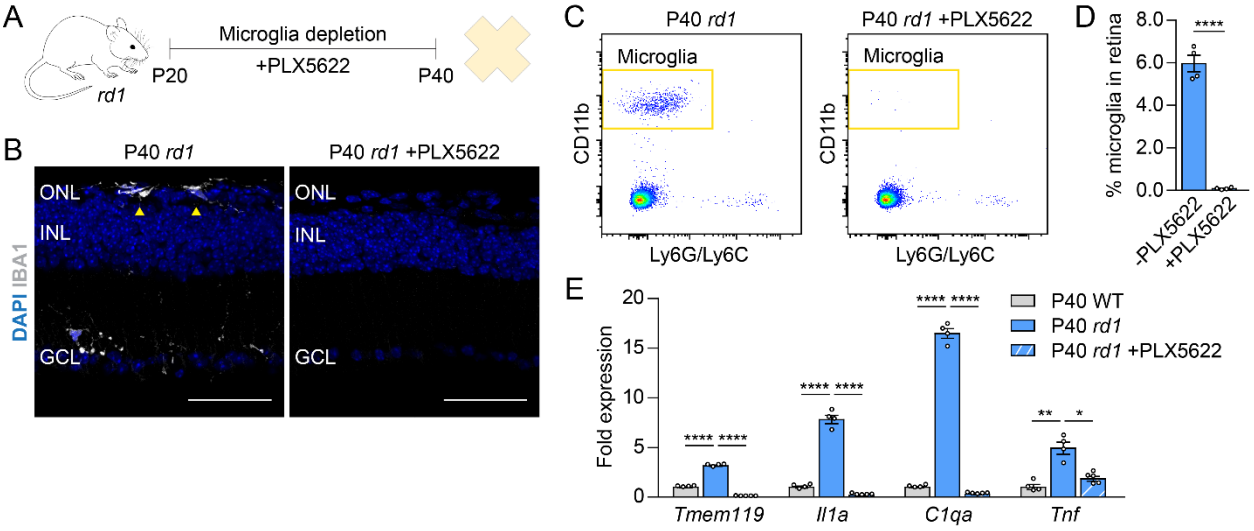

Figure 1. Retinal expression of inflammatory genes after microglia depletion. (**A**) Timeline of microglia depletion. Microglia from FVB (*rd1*) mice were pharmacologically depleted with PLX5622 beginning at P20 with harvesting of retinas at P40. (**B**) Retinal cross-sections from P40 *rd1* mice with or without depletion. Arrowheads depict Iba1-positive microglia in the ONL by immunostaining. Scale bar, 50 µm. (**C**, **D**) Representative gating (C) and quantification (D) by flow cytometry of microglia as a percentage of all retinal cells in P40 *rd1* mice (n = 4) with or without depletion. Microglia were defined as CD11b-positive Ly6G/Ly6C-negative cells. For full gating strategy, see Supplemental Fig. 1. (**E**) mRNA expression of indicated genes in retinas (n = 4-5) from WT (CD-1) or *rd1* mice with or without depletion. Fold changes are relative to WT retinas. Data shown as mean ± SEM. * P<0.05, ** P<0.01, **** P<0.0001 by two-tailed Student's t-test for (D), two-tailed Student's t-test with Bonferroni correction for (E). ONL, outer nuclear layer; INL, inner nuclear layer; GCL, ganglion cell layer.

TGF-β is a major anti-inflammatory cytokine that signals through the TGF-β type I (TGFBR1) and II (TGFBR2) receptors to trigger downstream expression of target genes (24). Exogenous TGF-β can inhibit microglial production of inflammatory cytokines such as *Tnf* and *Il6* (18,19), whereas ablation of TGF-β signaling in microglia via genetic deletion of TGFBR2 leads to activation of these cells (25) and, notably, degenerative changes in the retina highly reminiscent of RP (26). We reasoned that suppressing microglial activation and its resulting inflammation with TGF-β might be beneficial for degenerating cones in RP. To test this idea, adeno-associated viral (AAV) vectors encoding each of the TGF-β isoforms – TGF-β1 (AAV8-TGFB1), TGF-β2 (AAV8-TGFB2), and TGF-β3 (AAV8-TGFB3) – were synthesized and subretinally injected into *rd1* mice at postnatal day 0-1 (P0-P1), a time point that enables infection of the entire retina (Fig. 2*A* and *B*). These vectors used the human red opsin promoter to drive expression in cones (27) and were co-administered with a previously described GFP vector (AAV8-GFP) employing the same promoter to facilitate cone quantification (11,12). GFP driven by the human red opsin promoter could first be detected in cones around 7 days post-injection, with strong expression by day 14 (Supplemental Fig. 2). AAV vectors with this same promoter resulted in significant upregulation of TGF-β in infected retinas at both the mRNA and protein levels (Supplemental Fig. 2).

Secondary cone degeneration begins around P20 in *rd1* mice, with massive loss of cones by P50, particularly within the central retina (Fig. 2*C*). To measure the effect of TGF-β isoforms on retinal degeneration, the number of GFP-positive cones in the central retina was therefore quantified. Compared to AAV8-GFP alone, there was no significant difference in the number of cones at P50 with the addition of AAV8-TGFB2, and only a modest increase with AAV8-TGFB3 (Fig. 2*D* and *E*). In contrast, co-infection with AAV8-TGFB1 nearly tripled the number of cones in the central retina at P50. To determine whether greater cone numbers with TGF-β1 were a result of cone preservation or rather a perturbation in retinal development, *rd1* retinas treated with AAV8-GFP or AAV8-GFP plus AAV8-TGFB1 were examined at P20, prior to

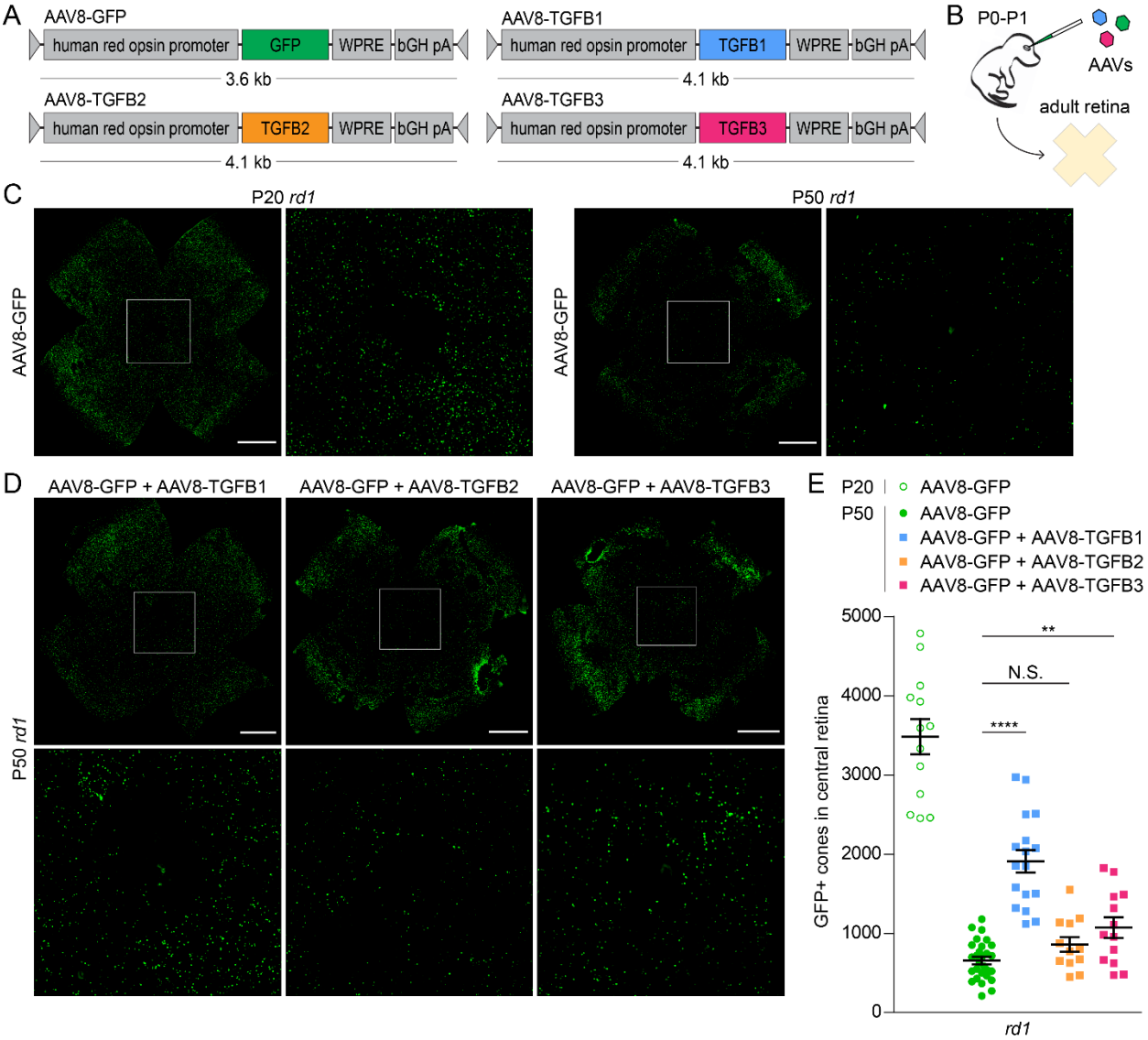

Figure 2. Effect of overexpressing TGF-β isoforms on cone survival. (**A**, **B**) Schematics of AAV vector design (A) and delivery (B). (**C**) Representative flat-mounts of FVB (*rd1*) retinas treated with AAV8-GFP and harvested at P20 or P50. Paired images depict low and high magnifications (boxed areas). Scale bar, 1 mm. (**D**) Representative flat-mounts of *rd1* retinas treated with indicated vectors and harvested at P50. Scale bar, 1 mm. (**E**) Quantification of GFP-positive cones in central retinas of *rd1* mice treated with indicated vectors (n = 12-28). Data shown as mean ± SEM. ** P<0.01, **** P<0.0001 by two-tailed Student's t-test with Bonferroni correction. N.S., not significant.

secondary cone degeneration. AAV8-TGFB1 did not alter the number of cones at this time point (Supplemental Fig. 2), suggesting that the difference in cones at P50 was indeed due to longer survival. As increased cone counts with TGF-β1 could also be explained by a rearrangement of peripheral cones to the central retina, whole *rd1* retinas were analyzed at P30 by flow cytometry, which showed significantly more GFP-positive cones in eyes treated with AAV8-GFP

plus AAV8-TGFB1 compared to AAV8-GFP only (Supplemental Fig. 2). Together, these data indicated that AAV8-TGFB1 could rescue degenerating cones in the *rd1* model of RP.

AAV8-TGFB1 was next studied in two more slowly degenerating mouse models of RP: *rd10*, which harbors a mutation in *Pde6b*, a common cause of autosomal recessive RP (21), and *Rho*$^{-/-}$, which lacks rhodopsin, the most frequently mutated gene in autosomal dominant RP (28). In both strains, AAV8-TGFB1 again significantly improved cone survival (Fig. 3*A*-*C*), implying that TGF-β1 might be broadly beneficial for cones in RP irrespective of the causal mutation. In addition, the impact of TGF-β1 on rod survival was investigated in *rd10* mice by measuring the thickness of the outer nuclear layer (ONL), which normally consists primarily of rods. Despite preserving cones in the same model, AAV8-TGFB1 did not prevent rod death and the reduction of ONL thickness in *rd10* retinas (Supplemental Fig. 3). Thus, the therapeutic effect of AAV8-TGFB1 in RP appears to be selective for cones.

Encouraged by our histological findings, we assessed the potential clinical relevance of TGF-β1 gene therapy by subjecting treated mice to a light-dark discrimination test. Sighted mice spend less time in well-illuminated spaces as demonstrated by the strong preference of wild-type animals for the dark half of a 50:50 light-dark box (Fig. 3*D* and Supplemental Fig. 3*C*). Conversely, *rd1* mice, which can no longer distinguish light from dark by P30 due to loss of functional photoreceptors, equally split their time between the two compartments. Compared to animals without treatment or receiving AAV8-GFP only, *rd1* mice treated with AAV8-GFP plus AAV8-TGFB1 spent significantly more time in the dark, consistent with an improvement in visual function allowing for light-dark discrimination. As a complementary measure of vision, the optomotor assay was performed on *rd10* mice treated with AAV8-GFP in one eye and AAV8-GFP plus AAV8-TGFB1 in the other. In this experiment, moving stripes are used to elicit the visually-dependent optomotor response. By adjusting the stripes until the animal can no longer track them, the visual acuity in each eye can be estimated (29). At P60, *rd10* eyes treated with AAV8-GFP plus AAV8-TGFB1 exhibited significantly better visual acuity than those only

receiving AAV8-GFP (Fig. 3*E*). From these data, we concluded that TGF-β1 in mouse RP not only helps preserve cones, but also importantly protects from vision loss.

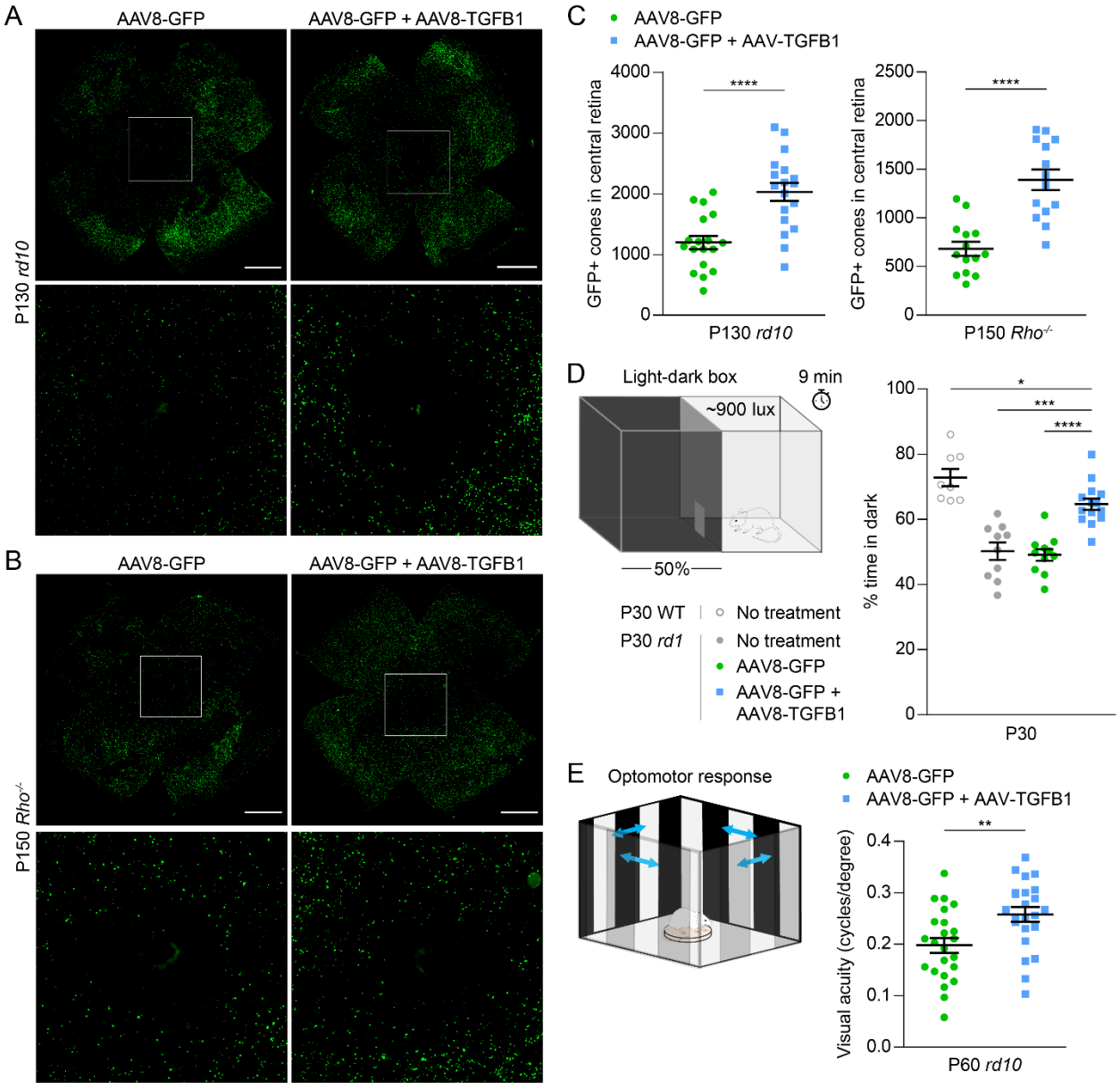

Figure 3. Effect of AAV8-TGFB1 on long-term cone survival and cone-mediated vision. (**A**, **B**) Representative flat-mounts of *rd10* (A) and *Rho*$^{-/-}$ (B) retinas treated with AAV8-GFP or AAV8-GFP plus AAV8-TGFB1. Paired images depict low and high magnifications (boxed areas). Scale bar, 1 mm. (**C**) Quantification of GFP-positive cones in central retinas of *rd10* (*n* = 18) and *Rho*$^{-/-}$ (*n* = 14) mice. (**D**) Percentage of time spent in dark in a 50:50 light-dark box for untreated animals and C3H (*rd1*) mice treated with AAV8-GFP or AAV8-GFP plus AAV8-TGFB1 (*n* = 8-14). (**E**) Visual acuity in eyes from P60 *rd10* mice (*n* = 23) as measured by optomotor after treatment with AAV8-GFP or AAV8-GFP plus AAV8-TGFB1. Data shown as mean ± SEM. * $P<0.05$, ** $P<0.01$, *** $P<0.001$, **** $P<0.0001$ by two-tailed Student's t-test for (C, E), two-tailed Student's t-test with Bonferroni correction for (D).

How does AAV8-TGFB1 combat secondary cone degeneration? Given the anti-inflammatory properties of TGF-β, mRNA levels of *Tmem119*, *Il1a*, *C1qa*, and *Tnf* in P40 *rd1* retinas were quantified and, surprisingly, were found to be unchanged with AAV8-TGFB1 (Fig. 4*A*). AAV8-TGFB1 likewise did not affect the number of microglia in the retina as assayed by flow cytometry (Supplemental Fig. 4), and treatment did not alter the percentage of microglia in the ONL (Fig. 4*B* and *C*), the retinal layer in which microglia preferentially localize during degeneration (12). To better understand the microglial response to AAV8-TGFB1, microglia from P30 *rd1* retinas treated with AAV8-GFP or AAV8-GFP plus AAV8-TGFB1 were isolated by cell sorting and subjected to RNA sequencing (RNA-seq). Sorted microglia were highly pure, expressing microglia markers such as *Tmem119* and *P2ry12,* but not those of other cell types (Supplemental Fig. 4). Only 23 genes were significantly altered (adjusted $P<0.05$, $\log_2$ fold change >0.4) in microglia treated with AAV8-TGFB1 (Fig. 4*D*). These included *Spp1* and *Gas6*, the most upregulated and downregulated of the 23 genes, respectively, which were validated by RT-PCR in microglia from both P30 *rd1* and P200 *rd10* retinas (Supplemental Fig. 4).

The importance of these gene expression changes in microglia was subsequently evaluated by depleting microglia from mice treated with AAV8-TGFB1 during secondary cone degeneration. Beginning at P20, *rd1* mice were administered PLX5622, which eliminated ~99% of retinal microglia even in AAV-infected eyes (Supplemental Fig. 4). While microglia depletion had no significant effect on cone survival in *rd1* retinas treated with AAV8-GFP only (Fig. 4*G*), consistent with our prior observations (12), it significantly abrogated cone rescue by AAV8-TGFB1. These findings indicate that microglia are not inherently helpful or harmful for degenerating cones, but are necessary for the cone survival mediated by TGF-β1 gene therapy. In the retina, microglia are among the only cells that highly express TGFBR1 and TGFBR2 (Fig. 4*E* and *F*) (26), both of which are required for TGF-β signaling (24). We therefore hypothesized that AAV8-TGFB1 might act via TGF-β receptors on microglia in order to promote cone survival. To test this, *rd1* mice treated with AAV8-GFP or AAV8-GFP plus AAV8-TGFB1 were

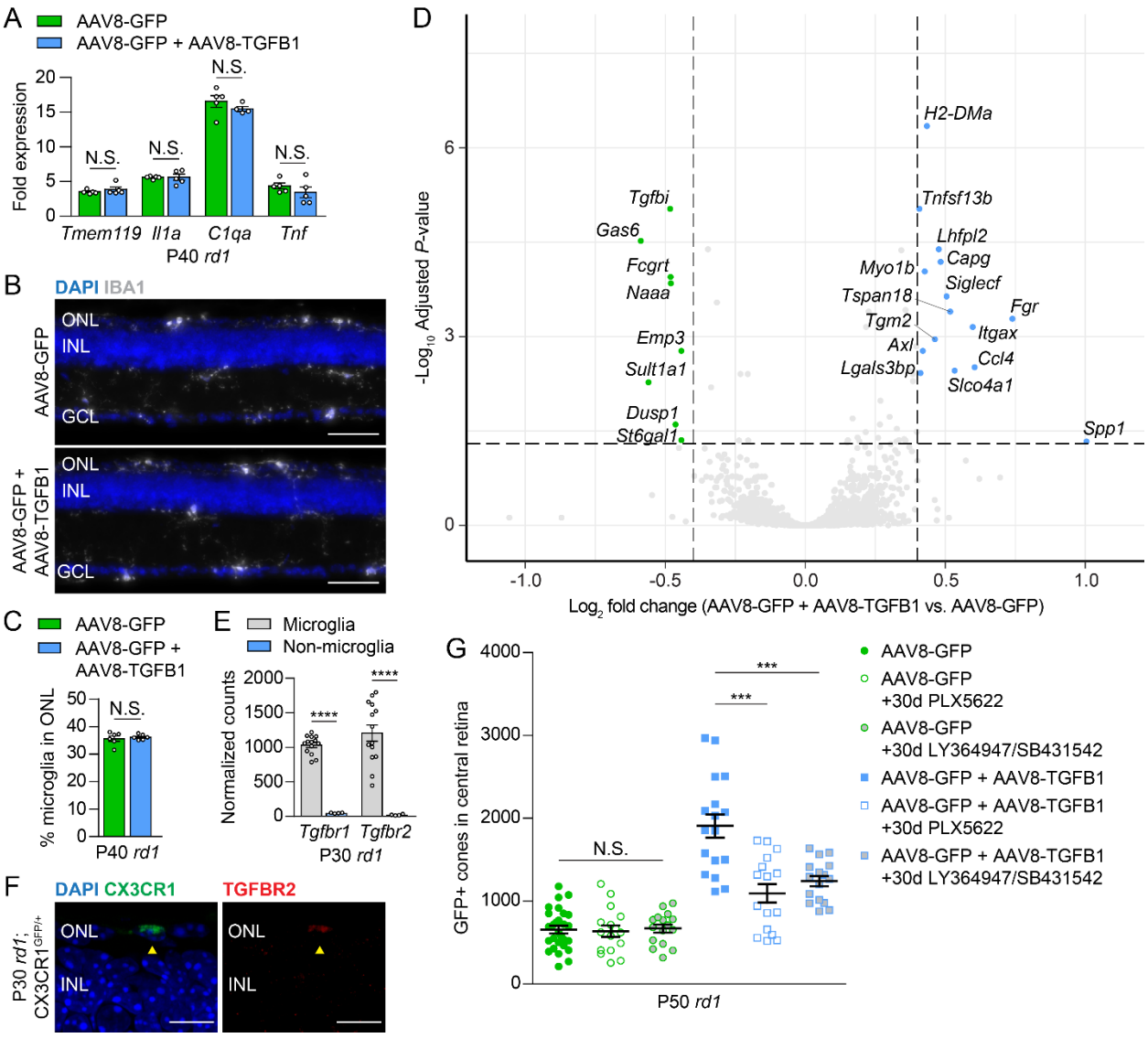

Figure 4. Role of retinal microglia in AAV8-TGFB1-mediated cone survival. (**A**) mRNA expression of indicated genes in FVB (*rd1*) retinas (*n* = 4-5) treated with AAV8-GFP or AAV8-GFP plus AAV8-TGFB1. Fold changes are relative to WT (CD-1) retinas. (**B**, **C**) Representative images (**B**) and quantification (**C**) of Iba1-positive microglia in the ONL of P40 *rd1* retinas (*n* = 6-7) treated with AAV8-GFP or AAV8-GFP plus AAV8-TGFB1. Scale bar, 50 µm. (**D**) Volcano plot of up- and down-regulated genes in microglia sorted from P30 *rd1* retinas (*n* = 7) after treatment with AAV8-GFP plus AAV8-TGFB1 relative to AAV8-GFP only. Dotted lines indicate adjusted *P*<0.05 and log2 fold-change >0.4. (**E**) Normalized RNA-seq counts for expression of *Tgfbr1* and *Tgfbr2* in microglia versus non-microglia cells from P30 *rd1* retinas (*n* = 4-14). (**F**) Immunostaining for TGFBR2 in an *rd1*;CX3CR1$^{GFP/+}$ retina. Arrowhead indicates colocalization TGFBR2 with a CX3CR1-positive microglia in the ONL. Scale bar, 10 µm. (**G**) Quantification of GFP-positive cones in central retinas of *rd1* mice after 30 days of microglia depletion with PLX5622 (*n* = 16) or inhibition of TGFBR1/2 with LY364947 and SB431542 (*n* = 16). Data for untreated groups are taken from Figure 2E. Data shown as mean ± SEM. *** *P*<0.001, **** *P*<0.0001 by two-tailed Student's t-test with Bonferroni correction for (**A**, **G**), two-tailed Student's t-test for (**C**, **E**). INL, inner nuclear layer; N.S., not significant.

administered a combination of LY364947 and SB431542, potent TGFBR1/2 inhibitors capable of blocking these receptors *in vivo* (30). As with microglia depletion, TGFBR1/2 inhibition had no discernable effect on retinas treated with AAV8-GFP only (Fig. 4*G*), suggesting that any endogenous signaling through these receptors during cone degeneration did not dramatically affect cone survival. On the other hand, treatment with LY364947 and SB431542 significantly disrupted the ability of AAV8-TGFB1 to preserve cones (Fig. 4*G*). Collectively, these results demonstrated that both microglia and TGF-β signaling through TGFBR1 and TGFBR2 are needed for AAV8-TGFB1 to function therapeutically.

In summary, AAV8-TGFB1 provides a novel gene therapy that generically protects cones and vision in multiple mouse models of RP, supporting its potential translation to human patients. Interestingly, although depletion of microglia itself does not help or hinder cone survival, cone rescue by AAV8-TGFB1 requires microglia. Together, these findings suggest that microglia do not play a significantly negative role during cone degeneration in RP, and under certain conditions, can be induced to benefit cones. Our study further shows a dependence of TGF-β gene therapy upon TGFBR1 and TGFBR2, which likely mediate signaling directly within microglia. We favor a model in which this signaling induces microglia to create a retinal environment favorable to cone survival. Our findings thus highlight a new immunomodulatory strategy centered around microglia for treating patients with RP, an approach that may also be relevant for other degenerative diseases of the visual system and CNS.

Materials and Methods

***Animals*.** CD-1 (#022) and FVB (*rd1*) (#207) mice were purchased from Charles River Laboratories. *rd10* (#004297), C3H (*rd1*) (#000659), sighted C3H (#003648), and CX3CR1$^{GFP/+}$ (#005582) mice were purchased from The Jackson Laboratory. Rhodopsin null (*Rho*$^{-/-}$) mice were a gift from Janis Lem (Tufts University, Boston, MA, USA) (28). FVB and CX3CR1$^{GFP/+}$ mice were crossed for at least four generations to obtain *rd1*;CX3CR1$^{GFP/+}$ animals. All mice

were subsequently bred and maintained at Harvard Medical School on a 12-hour alternating light and dark cycle.

Histology. Preparation of retinal cross-sections for immunohistochemistry and retinal flat-mounts to measure cone survival was performed as described in Chapter 2. If applicable, sections were then blocked for one hour at room temperature in phosphate-buffered saline (PBS) containing 5% goat serum and 0.1% Triton X-100 and stained with either 1:1000 of rabbit anti-Iba1 (Thermo Fisher Scientific) or 1:100 of rabbit anti-TGFBR2 (Abcam), followed by 1:1000 of goat anti-rabbit Alexa Fluor 594 (Jackson ImmunoResearch).

***Microglia depletion*.** Microglia were depleted using PLX5622 (a gift from Plexxikon, Berkeley, CA, USA), an orally available CSF1R inhibitor, formulated into AIN-76A rodent chow (Research Diets) at 1200 mg/kg and provided *ad libitum*.

***Flow cytometry and cell sorting*.** Flow cytometry and cell sorting were performed on a BD FACSAria II and analyzed using FlowJo 10 (Tree Star). Sorting of retinal cells was performed as described in Chapter 2. For peripheral blood cells, 50 µL of tail vein blood from each mouse was collected in PBS containing 2mM ethylenediaminetetraacetic acid (EDTA) and red blood cells lysed using BD Pharm Lysing Buffer according to manufacturer's instructions. For peritoneal cells, 10 mL of FACS buffer (PBS containing 2% fetal bovine serum and 2mM EDTA) was injected into the peritoneal cavity of each animal shortly after sacrifice. Following peritoneal massage, the buffer was collected and centrifuged at 400 x g for ten minutes to precipitate peritoneal cells. If applicable, harvested cells were blocked for five minutes on ice with 1:100 of rat anti-mouse CD16/32 (BD Pharmingen) and stained with 1:200 of PE-Cy5 anti-CD11b, FITC anti-F4/80, APC-Cy7 anti-Ly6C, or APC-Cy7 anti-Ly6G (all BioLegend). Populations were then passed through a 40 µm filter and resuspended in FACS buffer containing 0.5 µg/mL 4′,6-diamidino-2-phenylindole (DAPI) to exclude non-viable cells.

***RT-PCR*.** mRNA was collected from whole retinas or sorted microglia as described in Chapter 2. Following cDNA synthesis, RT-PCR reactions were performed in triplicate with

expression normalized to the housekeeping gene *Gapdh*. Sequences for RT-PCR primers were designed using PrimerBank (31).

***Plasmid design and vector production*.** The AAV-human red opsin-GFP-WPRE-bGH (AAV8-GFP) plasmid was a gift from Botond Roska (Friedrich Miescher Institute for Biomedical Research, Basel, Switzerland) (32). To generate plasmids for TGF-β isoforms, the GFP coding sequence from AAV8-GFP was replaced with the full-length mouse cDNA for TGF-β1 (NM_011577.2), TGF-β2 (NM_009367.4), or TGF-β3 (NM_009368.3) flanked by NotI and AgeI restriction sites. Recombinant AAV serotype 8 (AAV8) vectors were produced as described in Chapter 2.

***Subretinal injections*.** All injections were performed on neonatal mice (P0-P1) as described in Chapter 2. For each eye, 5×10^8 vector genomes (vg) per eye of AAV8-GFP were administered, a dose sufficient to infect 90-99% of cones in wild-type retinas (11,12). All other vectors were administered at 1×10^9 vg per eye. At these doses, co-infection with two AAV vectors in cones is expected to be at least 90% (11).

***Image acquisition and analysis*.** Images of retinal cross-sections and flat-mounts were acquired using a Zeiss LSM710 scanning confocal microscope (20x air objective or 40x oil objective) and Nikon Ti inverted widefield microscope (10x air objective), respectively. All image analysis was performed using ImageJ. Quantification of cone survival in retinal flat-mounts and microglia in the ONL of retinal cross-sections were performed as described in Chapter 2.

***Ex vivo retinal culture*.** Freshly isolated retinas were relaxed with four radial incisions and placed on a 12 mm Millicell cell culture insert (Millipore) resting on 2 mL of prewarmed culture media with the ganglion cell layer facing up. Culture media consisted of a 1:1 ratio of DMEM and F-12 supplemented with L-glutamine, B27, N2, and penicillin-streptomycin. Explants were maintained in humidified incubators at 37°C and 5% CO2 for 48 hours, after which the media was assayed for TGF-β1 protein using a commercial ELISA kit (R&D Systems). ELISA reactions were performed in triplicate with 50 µL of media as input.

***Light-dark discrimination*.** Innate light-avoidance behavior in mice was assessed as previously described (33) with minor modifications. A 28 cm (length) by 28 cm (width) by 21 cm (height) plastic chamber (Med Associates) was divided into two equally sized compartments: one dark and one brightly illuminated (~900 lux). Temperatures in the two compartments differed by less than 1°C. A small opening connected the two compartments, allowing subjects to freely travel throughout the chamber. At the beginning of each trial, a mouse was placed in the illuminated compartment and its activity recorded for ten minutes. If after one minute, the animal had not yet entered the dark compartment, it was gently directed there, removed from the chamber, and the trial restarted. The location and movement of each mouse were determined by infrared sensors and analyzed with Activity Monitor (Med Associates). Time spent in dark was calculated based on activity during the final nine minutes of each trial.

***Optomotor assay*.** Visual acuity was measured using the optomotor response by an observer (Y.X.) blinded to the treatment assignment as described in Chapter 2.

***RNA sequencing*.** Transcriptional profiling of microglia (seven biological replicates per experimental condition) or non-microglia (four biological replicates total) was performed as described in Chapter 2. 1000 microglia (CD11b+ Ly6G/Ly6C-) or non-microglia cells (CD11b-) were sequenced from each retina with an expected coverage of ~6 million reads per sample.

***TGFBR1/2 inhibition*.** Pharmacological inhibition of the TGF-β type I and II receptors *in vivo* was performed using a combination of SB431542 (SelleckChem) and LY364947 (SelleckChem) as previously described (30). Both compounds were dissolved in PBS containing 5% dimethyl sulfoxide (DMSO) and 30% polyethylene glycol 300 and dosed at 10 mg/kg daily via intraperitoneal injections.

***Statistics*.** All group data are shown as mean ± SEM. Two-tailed Student's t-tests were used to compare experimental groups, with the addition of a Bonferroni correction if three or more hypotheses were tested. Differences between groups were considered significant when the *P*-value was less than 0.05.

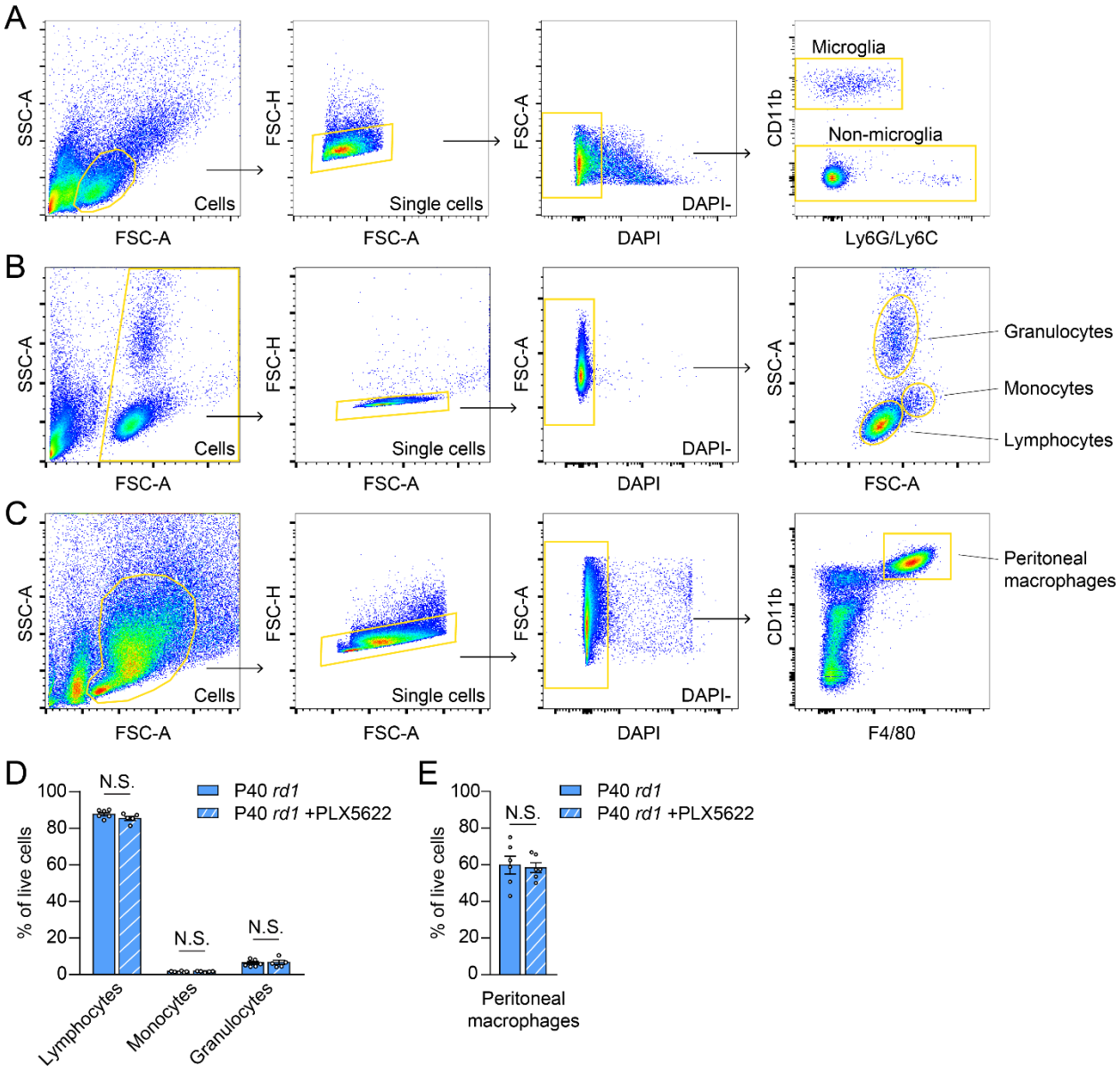

Supplemental Figure 1. (**A**) Representative flow cytometry gating for microglia and non-microglia cells in the retina. Microglia were defined as CD11b-positive Ly6G/Ly6C-negative cells. Non-microglia were defined as CD11b-negative cells. (**B**) Representative flow cytometry gating for lymphocytes, monocytes, and granulocytes from peripheral blood. Each population was defined based on its characteristic forward scatter (FSC) and side scatter (SSC) profile as previously described (34). (**C**) Representative flow cytometry gating for peritoneal macrophages isolated from the peritoneal cavity. Peritoneal macrophages were defined as CD11b-positive F4/80-positive cells. (**D**, **E**) Quantification of peripheral blood immune populations (n = 5-6) (D) and peritoneal macrophages (n = 6) (E) from P40 FVB (*rd1*) mice with or without microglia depletion by PLX5622. Data shown as mean ± SEM. N.S., not significant by two-tailed Student's t-test.

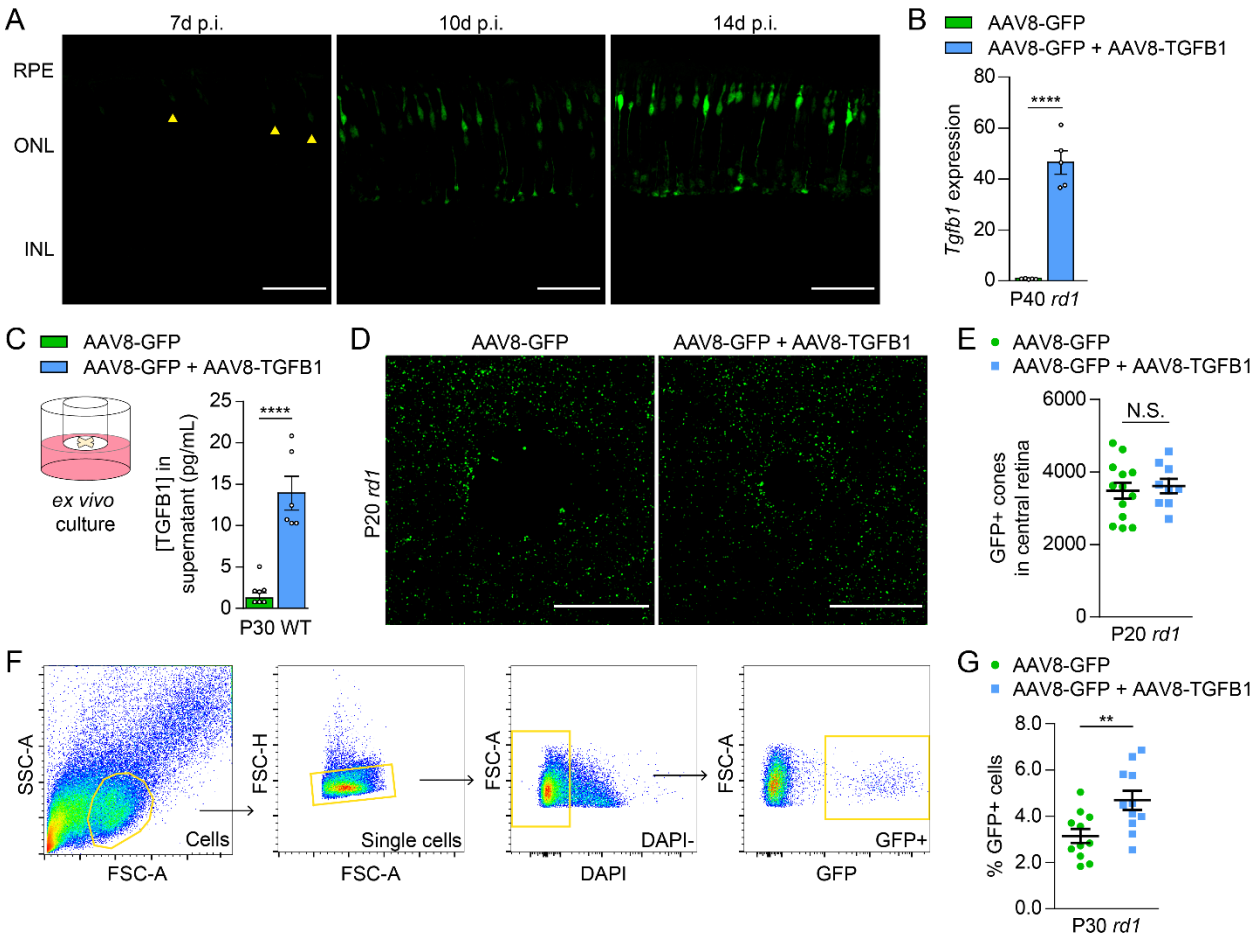

Supplemental Figure 2. (**A**) Kinetics of GFP expression in cones after subretinal delivery of AAV8-GFP. Arrowheads indicate faint GFP expression. Scale bar, 50 µm. (**B**) mRNA expression of *Tgfb1* in FVB (*rd1*) retinas (n = 4-5) after treatment with AAV8-GFP plus AAV8-TGFB1 relative to AAV8-GFP only. (**C**) Quantification of TGFB1 secreted during *ex vivo* culture from WT (CD-1) retinas (n = 6-7) treated with AAV8-GFP or AAV8-GFP plus AAV8-TGFB1. (**D**, **E**) Representative images (D) and quantification (E) of cone survival in central retinas of P20 *rd1* mice (n = 9-13) treated with AAV8-GFP or AAV8-GFP plus AAV8-TGFB1. Scale bar, 500 µm. (**F**, **G**) Representative gating (F) and quantification (G) by flow cytometry of GFP-positive cones from P30 FVB (*rd1*) retinas (n = 11) treated with AAV8-GFP or AAV8-GFP plus AAV8-TGFB1. Data shown as mean ± SEM. ** P<0.01, **** P<0.0001 by two-tailed Student's t-test. RPE, retinal pigmented epithelium; INL, inner nuclear layer; N.S., not significant.

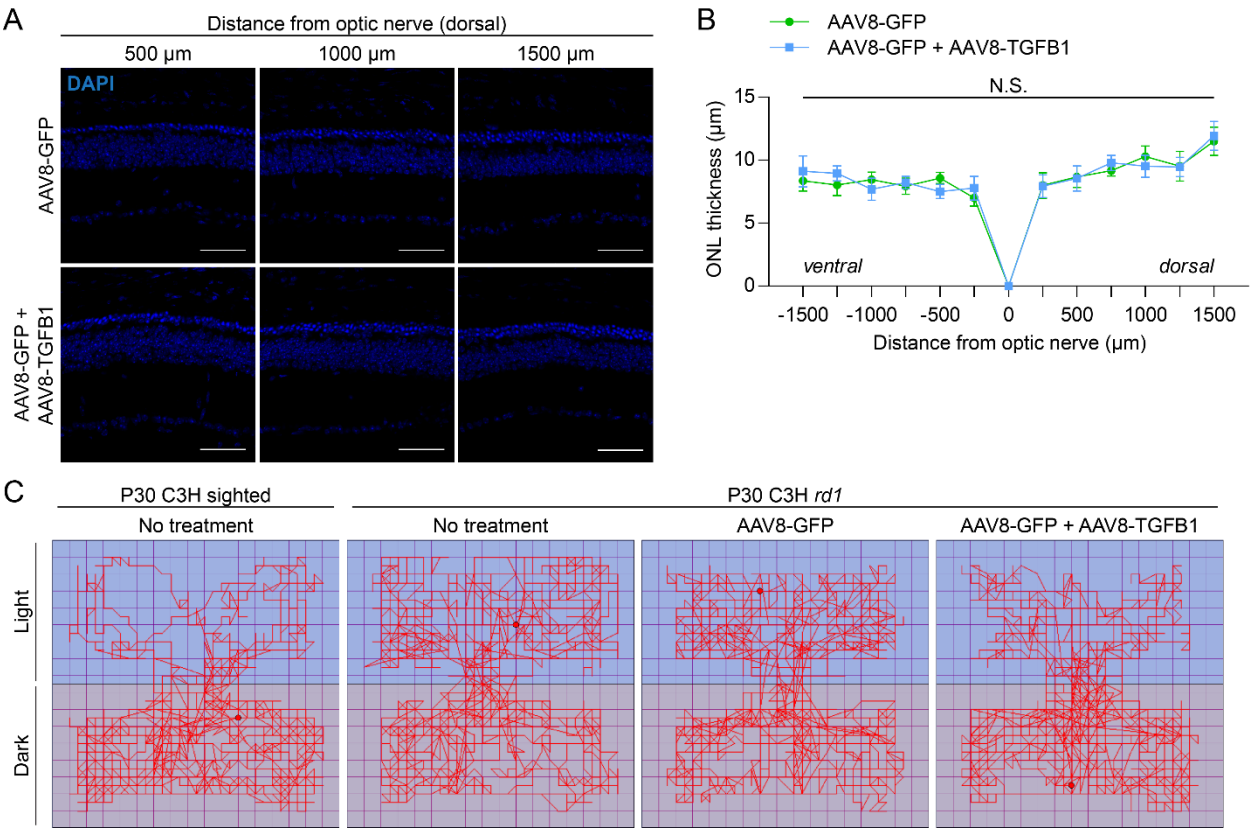

Supplemental Figure 3. (**A**, **B**) Representative cross-sections (A) and measurements of ONL thickness (B) at indicated distances from the optic nerve in P40 *rd10* retinas (*n* = 6) treated with AAV8-GFP or AAV8-GFP plus AAV8-TGFB1. Scale bar, 50 µm. (**C**) Representative movement tracks during light-dark box testing from untreated animals and C3H (*rd1*) mice treated with AAV8-GFP or AAV8-GFP plus AAV8-TGFB1. Data shown as mean ± SEM. N.S., not significant.

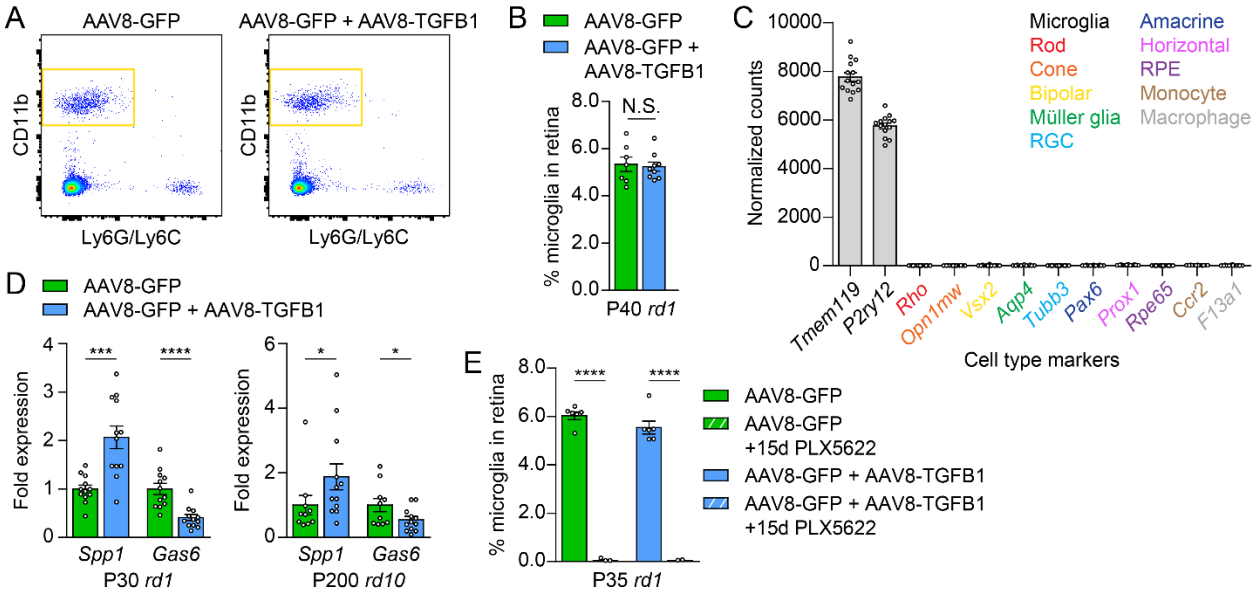

Supplemental Figure 4. (**A**, **B**) Representative gating (A) and quantification (B) by flow cytometry of microglia as a percentage of all retinal cells in P40 FVB (*rd1*) retinas (n = 7-9) treated with AAV8-GFP or AAV8-GFP plus AAV8-TGFB1. (**C**) Normalized RNA-seq counts for indicated cell type markers in microglia sorted from P30 *rd1* retinas (n = 14). (**D**) mRNA expression of *Spp1* and *Gas6* in sorted microglia from P30 *rd1* retinas (n = 12) and P200 *rd10* retinas (n = 10-12) after treatment with AAV8-GFP plus AAV8-TGFB1 relative to AAV8-GFP only. (**E**) Quantification by flow cytometry of retinal microglia from P35 *rd1* retinas (n = 2-6) treated with AAV8-GFP or AAV8-GFP plus AAV8-TGFB1 after 15 days of microglia depletion. Data shown as mean ± SEM. * P<0.05, *** P<0.001, **** P<0.0001 by two-tailed Student's t-test. RGC, retinal ganglion cell; RPE, retinal pigmented epithelium; N.S., not significant.

References

1. Daiger SP, Sullivan LS, Bowne SJ. Genes and mutations causing retinitis pigmentosa. Clin Genet. 2013 Aug;84(2):132–41.
2. Merin S, Auerbach E. Retinitis pigmentosa. Surv Ophthalmol. 1976 Mar;20(5):303–46.
3. Hartong DT, Berson EL, Dryja TP. Retinitis pigmentosa. Lancet. 2006 Nov 18;368(9549):1795–809.
4. Narayan DS, Wood JPM, Chidlow G, Casson RJ. A review of the mechanisms of cone degeneration in retinitis pigmentosa. Acta Ophthalmol. 2016 Dec;94(8):748–54.
5. N. Sahni J, Angi M, Irigoyen C, Angi M, Semeraro F, R. Romano M, et al. Therapeutic Challenges to Retinitis Pigmentosa: From Neuroprotection to Gene Therapy. Curr Genomics. 2011 Jun 1;12(4):276–84.
6. Huang X-F. Current Pharmacological Concepts in the Treatment of the Retinitis Pigmentosa. In: Advances in experimental medicine and biology. 2018. p. 439–45.
7. Russell S, Bennett J, Wellman JA, Chung DC, Yu Z-F, Tillman A, et al. Efficacy and safety of voretigene neparvovec (AAV2-hRPE65v2) in patients with RPE65 -mediated inherited retinal dystrophy: a randomised, controlled, open-label, phase 3 trial. Lancet. 2017 Aug 26;390(10097):849–60.
8. Trapani I, Banfi S, Simonelli F, Surace EM, Auricchio A. Gene Therapy of Inherited Retinal Degenerations: Prospects and Challenges. Hum Gene Ther. 2015 Apr;26(4):193–200.
9. Daiger SP, Bowne SJ, Sullivan LS. Perspective on genes and mutations causing retinitis pigmentosa. Arch Ophthalmol (Chicago, Ill 1960). 2007 Feb;125(2):151–8.
10. Byrne LC, Dalkara D, Luna G, Fisher SK, Clérin E, Sahel J-A, et al. Viral-mediated RdCVF and RdCVFL expression protects cone and rod photoreceptors in retinal degeneration. J Clin Invest. 2015 Jan 2;125(1):105–16.
11. Xiong W, Garfinkel AEM, Li Y, Benowitz LI, Cepko CL. NRF2 promotes neuronal survival in neurodegeneration and acute nerve damage. J Clin Invest. 2015;125(4):1433–45.
12. Wang SK, Xue Y, Rana P, Hong CM, Cepko CL. Soluble CX3CL1 gene therapy improves cone survival and function in mouse models of retinitis pigmentosa. Proc Natl Acad Sci. 2019 Apr 29;116(20):201901787.
13. Block ML, Zecca L, Hong J-S. Microglia-mediated neurotoxicity: uncovering the molecular mechanisms. Nat Rev Neurosci. 2007 Jan;8(1):57–69.
14. Subhramanyam CS, Wang C, Hu Q, Dheen ST. Microglia-mediated neuroinflammation in neurodegenerative diseases. Semin Cell Dev Biol. 2019 Oct;94:112–20.
15. Smith JA, Das A, Ray SK, Banik NL. Role of pro-inflammatory cytokines released from microglia in neurodegenerative diseases. Brain Res Bull. 2012 Jan 4;87(1):10–20.
16. Zhao L, Zabel MK, Wang X, Ma W, Shah P, Fariss RN, et al. Microglial phagocytosis of living photoreceptors contributes to inherited retinal degeneration. EMBO Mol Med. 2015 Sep;7(9):1179–97.
17. Peng B, Xiao J, Wang K, So K-F, Tipoe GL, Lin B. Suppression of Microglial Activation Is Neuroprotective in a Mouse Model of Human Retinitis Pigmentosa. J Neurosci. 2014 Jun 11;34(24):8139–50.
18. Kim W-K, Hwang S-Y, Oh E-S, Piao HZ, Kim K-W, Han I-O. TGF-beta1 represses activation and resultant death of microglia via inhibition of phosphatidylinositol 3-kinase activity. J Immunol. 2004 Jun 1;172(11):7015–23.
19. Taylor RA, Chang C-F, Goods BA, Hammond MD, Mac Grory B, Ai Y, et al. TGF-β1 modulates microglial phenotype and promotes recovery after intracerebral hemorrhage. J Clin Invest. 2017 Nov 3;127(1):280–92.
20. Elmore MRP, Najafi AR, Koike MA, Dagher NN, Spangenberg EE, Rice RA, et al. Colony-stimulating factor 1 receptor signaling is necessary for microglia viability, unmasking a microglia progenitor cell in the adult brain. Neuron. 2014 Apr 16;82(2):380–97.

21. Chang B, Hawes NL, Hurd RE, Davisson MT, Nusinowitz S, Heckenlively JR. Retinal degeneration mutants in the mouse. Vision Res. 2002 Feb;42(4):517–25.
22. Bennett ML, Bennett FC, Liddelow SA, Ajami B, Zamanian JL, Fernhoff NB, et al. New tools for studying microglia in the mouse and human CNS. Proc Natl Acad Sci. 2016 Mar 22;113(12):E1738–46.
23. Liddelow SA, Guttenplan KA, Clarke LE, Bennett FC, Bohlen CJ, Schirmer L, et al. Neurotoxic reactive astrocytes are induced by activated microglia. Nature. 2017 Jan 18;541(7638):481–7.
24. Wrana JL, Attisano L, Wieser R, Ventura F, Massagué J. Mechanism of activation of the TGF-β receptor. Nature. 1994 Aug 4;370(6488):341–7.
25. Zöller T, Schneider A, Kleimeyer C, Masuda T, Potru PS, Pfeifer D, et al. Silencing of TGFβ signalling in microglia results in impaired homeostasis. Nat Commun. 2018 Dec 1;9(1):4011.
26. Ma W, Silverman SM, Zhao L, Villasmil R, Campos MM, Amaral J, et al. Absence of TGFβ signaling in retinal microglia induces retinal degeneration and exacerbates choroidal neovascularization. Elife. 2019 Jan 22;8.
27. Li Q, Timmers AM, Guy J, Pang J, Hauswirth WW. Cone-specific expression using a human red opsin promoter in recombinant AAV. Vision Res. 2008 Feb;48(3):332–8.
28. Lem J, Krasnoperova N V, Calvert PD, Kosaras B, Cameron DA, Nicolò M, et al. Morphological, physiological, and biochemical changes in rhodopsin knockout mice. Proc Natl Acad Sci U S A. 1999 Jan 19;96(2):736–41.
29. Douglas RM, Alam NM, Silver BD, McGill TJ, Tschetter WW, Prusky GT. Independent visual threshold measurements in the two eyes of freely moving rats and mice using a virtual-reality optokinetic system. Vis Neurosci. 2005 Sep 6;22(5):677–84.
30. Maddaluno L, Rudini N, Cuttano R, Bravi L, Giampietro C, Corada M, et al. EndMT contributes to the onset and progression of cerebral cavernous malformations. Nature. 2013 Jun 27;498(7455):492–6.
31. Wang X, Spandidos A, Wang H, Seed B. PrimerBank: a PCR primer database for quantitative gene expression analysis, 2012 update. Nucleic Acids Res. 2012 Jan 1;40(D1):D1144–9.
32. Busskamp V, Duebel J, Balya D, Fradot M, Viney TJ, Siegert S, et al. Genetic Reactivation of Cone Photoreceptors Restores Visual Responses in Retinitis Pigmentosa. Science. 2010 Jul 23;329(5990):413–7.
33. Gaub BM, Berry MH, Holt AE, Reiner A, Kienzler MA, Dolgova N, et al. Restoration of visual function by expression of a light-gated mammalian ion channel in retinal ganglion cells or ON-bipolar cells. Proc Natl Acad Sci. 2014 Dec 23;111(51):E5574–83.
34. Rothe G, Gabriel H, Kovacs E, Klucken J, Stöhr J, Kindermann W, et al. Peripheral blood mononuclear phagocyte subpopulations as cellular markers in hypercholesterolemia. Arterioscler Thromb Vasc Biol. 1996 Dec;16(12):1437–47.

Chapter 4: AAV *cis*-regulatory sequences are correlated with ocular toxicity

Abstract

Adeno-associated viral (AAV) vectors have become popular for gene therapy given their many advantages, including a reduced inflammatory profile compared to other viral-derived vectors. Nonetheless, even in areas of immune privilege such as the eye, AAV vectors are capable of eliciting host-cell responses. To investigate the effects of such responses on several ocular cell types, we tested multiple vector genome structures and capsid types using subretinal injections in mice. Assays of morphology, inflammation, and physiology were performed. Pathological effects on photoreceptors and the retinal pigment epithelium (RPE) were observed. Müller glia and microglia were activated, and the proinflammatory cytokines TNF-α and IL-1β were upregulated. There was a strong correlation between *cis*-regulatory sequences and toxicity. AAV vectors with any one of three broadly active promoters, or an RPE-specific promoter, were toxic, while vectors with four different photoreceptor-specific promoters were not toxic at the highest doses tested. There was little correlation between toxicity and transgene, capsid type, preparation method, or cellular contaminants within a preparation. The toxic effect was dose-dependent, with the RPE being more sensitive than photoreceptors. Our results suggest that AAV vector toxicity in the eye is associated with certain *cis*-regulatory sequences and/or their activity and that retinal damage occurs due to responses by the RPE and/or microglia.

Contributions

Wenjun Xiong[1,2] *, David M. Wu[3,4] *, Yunlu Xue[3] *, Sean K. Wang[3], Michelle Chung[3,4,5], Xuke Ji[3], Parimal Rana[3], Sophia Zhao[3], Shuyi Mai[1,2], Constance L. Cepko[3,5]

[1] Department of Biomedical Sciences, City University of Hong Kong, Hong Kong, China

[2] City University of Hong Kong Shenzhen Research Institute, Shenzhen, China

[3] Departments of Genetics and Ophthalmology, Harvard Medical School, Boston, MA, USA

[4] Retina Service, Massachusetts Eye and Ear Infirmary, Boston, MA, USA

[5] Howard Hughes Medical Institute, Chevy Chase, MD, USA

* These authors contributed equally to work

W.X., D.M.W., Y.X., and C.L.C. conceived the study; W.X., D.M.W., Y.X., S.K.W., M.J.C., and C.L.C. designed research; W.X., D.M.W., Y.X., S.K.W., M.J.C., X.J., P.R., S.R.Z., and S.M. performed experiments; W.X., D.M.W., Y.X., S.K.W., M.J.C., and C.L.C. analyzed data; W.X., D.M.W., Y.X., and C.L.C. wrote the paper with contributions from S.K.W. and M.J.C.

Note: This work has been published. For brevity, some sections have been omitted. For full-text, please refer to:

Xiong W, Wu DM, Xue Y, Wang SK, Chung MJ, Ji X, et al. AAV *cis*-regulatory sequences are correlated with ocular toxicity. *Proc Natl Acad Sci*. 2019 Mar 4;116(12):5785–94.

Introduction

Adeno-associated viral (AAV) vectors are small, single-stranded (ss) DNA vectors derived from viruses in the *Parvoviridae* family that have several advantages as somatic gene therapy vectors. Recombinant AAV genomes typically lack viral genes and do not efficiently integrate into the host genome, reducing the risk of insertional mutagenesis. They establish as stable episomes and express transgenes indefinitely in postmitotic cells. Naturally existing AAV variants, together with an array of engineered variants, can infect a large variety of tissues and cell types in both animals and humans (1–3). These capsid variants can enable more targeted infection of a selected set of cell types, with transgene expression further specified through the use of transcription regulatory sequences. Finally, AAV vectors are non-pathogenic, which has predicted their safety for applications in gene therapy. Multiple clinical trials have indeed borne this out (4–7).

There are many recessive genes that cause ocular disease (sph.uth.edu/retnet/), and complementation by a vector-encoded gene can lead to an improvement in vision (8,9). The target cells for ocular gene therapy are most often the photoreceptors and retinal pigment epithelial (RPE) cells, as most genetic retinal diseases involve dysfunction and/or death of these cell types. There are two types of photoreceptors: rods, necessary for vision in dim light, and cones, required for color and daylight vision. Photoreceptor cells are supported by the RPE, a monolayer of epithelial cells with processes interdigitated with the outer segments (OS) of the photoreceptors. The subretinal space, the virtual space between the RPE and photoreceptors, is thus an effective injection delivery site for most ocular human gene therapy. In addition to these target cell types being very accessible for gene therapy, the eye offers several other advantages for somatic gene therapy. It is relatively immune-privileged (10) and anatomically compartmentalized and can be targeted by established clinical interventions. Furthermore, its target cells do not replicate and thus do not require integration. Given the cost of generating highly pure vectors, ocular AAV vectors also benefit from the fact that only a small volume is

needed for local administration. These advantages contributed to the approval of an AAV vector encoding the RPE65 gene (Luxturna) for Leber's congenital amaurosis 2 (LCA2) (4–6) and have motivated AAV-based clinical trials for other ocular diseases, such as choroideremia and retinitis pigmentosa (11,12).

Despite the safety of AAV vectors in humans to date, problems may be unmasked as use expands to more patients and additional indications. Current techniques for subretinal injection can only infect cells near the injection site, which comprise a small percentage of target cells. A more complete infection would likely result in a greater improvement in vision but would require a higher dose, possibly leading to toxicity. Toxicity associated with increasing doses of AAV vectors has been seen in preclinical models including nonhuman primates (NHPs), both in ocular and non-ocular tissues. An early indication came from treatment of hemophilia B by AAV-mediated factor IX expression. Infection in the liver triggered memory T cells reactive with the capsid, which cleared the infected cells and resulted in only transient expression of factor IX (13). More recently, systemic delivery of high doses of an AAV vector to NHPs and pigs led to neurotoxicity due to an uncharacterized mechanism (14). Specifically in the eye, AAV-induced toxicity has been observed in both small and large animal models (15–17). For example, following use of AAV2-CNGA3 to treat color blindness (achromatopsia) in sheep, two animals had loss of photoreceptors and RPE while another developed retinal atrophy and lymphocytic infiltration (18). In a different study, subretinal injection of AAV8-CNGA3 into NHP eyes resulted in activation of both innate and adaptive immune responses despite concomitant steroid treatment (19). In one of the LCA2 gene therapy trials, strong evidence of an inflammatory response emerged. Five out of eight subjects injected with the higher dose of AAV2-RPE65 (1E12 vector genomes [vg] per eye) developed various degrees of intraocular inflammation (20). One significant adverse event was reported in the Alberta choroideremia gene therapy trial, in which presumed intraretinal inflammation led to permanent structural and functional impairment of the patient's treated retina (21).

Our group has been studying gene therapy for degenerative retinal diseases in hope of creating vectors that are able to prolong photoreceptor survival and function. We found that subretinal delivery of some, but not all, AAV vectors in mice consistently induced cone OS shortening, reduction of the outer nuclear layer (ONL) where rods and cones reside, and dysmorphic RPE. We began tracking many details about our vectors but found no link between ocular toxicity and preparation methods, endotoxin level, cellular protein contaminants, or whether they were made in-house or at various core facilities. To search for the source of toxicity, we tested vector stocks with different *cis*-regulatory sequences, transgenes, and capsids. We found a strong correlation between the *cis*-regulatory sequences and toxicity. Vectors incorporating broadly active promoters, including cytomegalovirus immediate-early promoter (CMV) (22), human ubiquitin C promoter (UbiC) (23,24), and chicken beta actin promoter (CAG) (25), as well as an RPE-specific promoter (Best1) (26), were toxic. In contrast, vectors with photoreceptor-specific promoters, including human red opsin (RedO) (25, 26), human rhodopsin (Rho) (27,28), human rhodopsin kinase (RK) (29), and mouse cone arrestin (CAR) (30), were not toxic. As might be expected, damage from toxic AAV vectors was associated with dose. However, high-dose administration of photoreceptor-specific vectors did not lead to toxicity. The RPE was more sensitive to vector toxicity than photoreceptors. Moreover, microglial activation and inflammatory cytokine expression were triggered by the toxic vectors. These data highlight the need to develop sensitive assays for toxicity specific to the organs and cell types being targeted for gene therapy. Such assays will enable the design of AAV vectors that can be safely used at higher doses, potentially improving treatment efficacy.

Results

Photoreceptor toxicity is correlated with the specificity of vector promoters

Serotype 8 AAV vectors (AAV8) expressing either GFP or no transgene (“null”) under the control of different promoters were injected subretinally into neonatal mice (CD-1). Neonatal

mice were used as we have been able to achieve complete infection of the RPE and retina using animals of this age (31). In addition, less tissue damage is induced by injection at this early stage compared with the mature stage. The retinas and RPE were harvested for histological analysis at 30 days post-infection (or as indicated). The CMV promoter/enhancer sequence drives robust transgene expression in cone photoreceptors and the RPE, as well as other cell types (31). With AAV8-CMV-GFP, we saw photoreceptor toxicity and glial activation as indicated by cone OS shortening, ONL thinning, cone photoreceptor loss, and upregulation of GFAP in the Müller glia (Fig. 1*A*-*C*). In contrast, GFP driven by the photoreceptor-specific

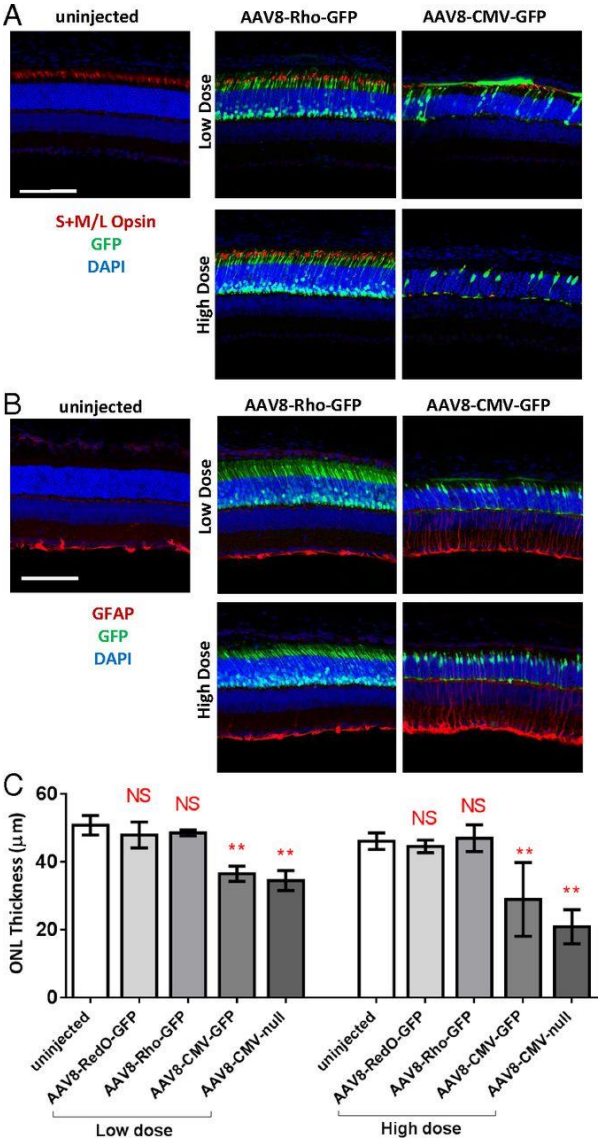

Figure 1. Ocular toxicity is induced by broadly active but not retinal cell-type-specific vector promoters.

(**A**, **B**) Wild-type retinas of CD-1 mice were infected at P0 with the indicated viruses at either high (3E9 vg per eye) or low dose (8E8 vg per eye) and harvested at P30 for histology. Retinal cross-sections were stained for short- and medium/long-wavelength opsins (red) (*A*) and for GFAP (red) (*B*). Loss of opsin staining and upregulated expression of GFAP were observed in the retinas infected with AAV8-CMV-GFP. Scale bar, 100 µm.

(**C**) Quantification of ONL thickness at 1 mm from optic nerve head (ONH). Data shown as mean ± SD. n = 3–17 per group. ** P<0.01 by one-way ANOVA analysis with Tukey test. NS, not significant between the designated group and the uninjected group.

promoters, including RedO, Rho, RK, and CAR, induced no retinal toxicity or glial activation (Fig. 1*A*-*C* and data not shown). To determine if toxicity was due to protein expression, AAV8-CMV-null, which did not express any transgene, was tested. By these assays, AAV8-CMV-null was just as toxic as AAV8-CMV-GFP (Fig. 1*C* and data not shown).

RPE toxicity is induced by AAV vectors with broadly active or RPE-specific promoters

Promoter-specific AAV toxicity also was observed in the RPE, which is efficiently transduced by subretinally delivered AAV. We developed a semi-quantitative assay to measure the RPE toxicity level to compare among vectors. Whole RPE flat-mounts were stained with phalloidin, which labels the F-actin borders of the hexagonal RPE array. These were imaged with a spinning-disk microscope and scored for the morphology using a grading system with six grades that we devised. Grade 0 indicates completely normal RPE morphology and grade 5 indicates complete RPE loss (Fig. 2*A*). Four representative areas in the midperiphery of each flat-mount were imaged and evaluated by four independent scorers blinded to the vector identity and dose, with the average score for each flat-mount shown in Fig. 2*B*. With this scoring system, we found that AAV vectors containing broadly active promoters (CMV, CAG, and UbiC) induced strong RPE toxicity while none containing photoreceptor-specific promoters did (Fig. 2*B*). The Best1 promoter was also tested for toxicity as it can drive strong expression in the RPE at a level comparable to that of CMV or CAG (26). Interestingly, AAV8 with Best1 promoter also induced RPE toxicity in the RPE (Fig. 2*B*).

Vector toxicity occurs independently of vector preparation

To determine if the method of vector preparation contributed to ocular toxicity, several different AAV8 preparation and purification protocols were tested. In addition, stocks of the same genomes and capsids were obtained from three different core facilities. For all vectors with a broadly active or RPE-specific promoter, toxicity was observed. Furthermore, we

examined toxic and non-toxic preparations on protein gels to examine the level of contamination by cellular proteins. We found that the level of cellular protein contaminants and endotoxin levels did not correlate with toxicity (data not shown).

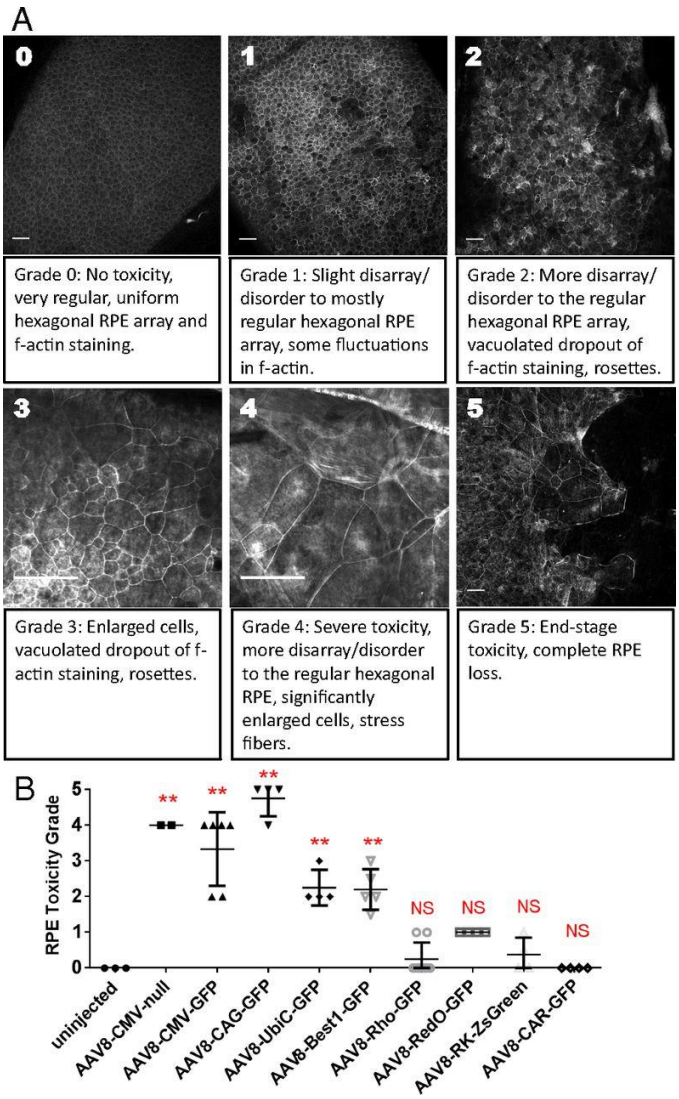

Figure 2. RPE toxicity from AAV vectors is induced by promoters with RPE activity.

(**A**) Grading criteria of RPE toxicity, with grade 0 representing completely healthy RPE and grade 5 representing the most severe RPE damage. The typical phenotypes of each grade are described below each image. Scale bar, 50 μm.

(**B**) Scatter dot plot of RPE toxicity grades. All viruses were tested at a dose of 8E8 vg per eye except for AAV8-CAR-GFP (3E9 vg per eye) in CD-1 mice injected at P0 and harvested at P30. Data are presented as mean ± SD. n = 2–8 per group. ** P<0.01 by one-way ANOVA analysis with Tukey test. NS, not significant between the designated group and the uninjected group.

Severity of photoreceptor and RPE toxicity correlate with vector dose

In clinical trials, AAV vectors are subretinally administered at a wide range of doses (20,21,32,33). To investigate whether vector-induced toxicity was dose-dependent, we thus injected AAV8-CMV-GFP into neonatal CD-1 mice at three doses (5E8, 1E9, and 2E9 vg per eye). RPE toxicity was evaluated at 30 days post-infection. There was a clear correlation

between the severity of RPE toxicity and vector dose. A lower dose of 5E8 vg per eye induced RPE cell enlargement with some loss of RPE cells (approximately grade 3), while a higher dose of 2E9 vg per eye caused nearly complete RPE loss (approximately grade 5) (Fig. 3*A*–*C*).

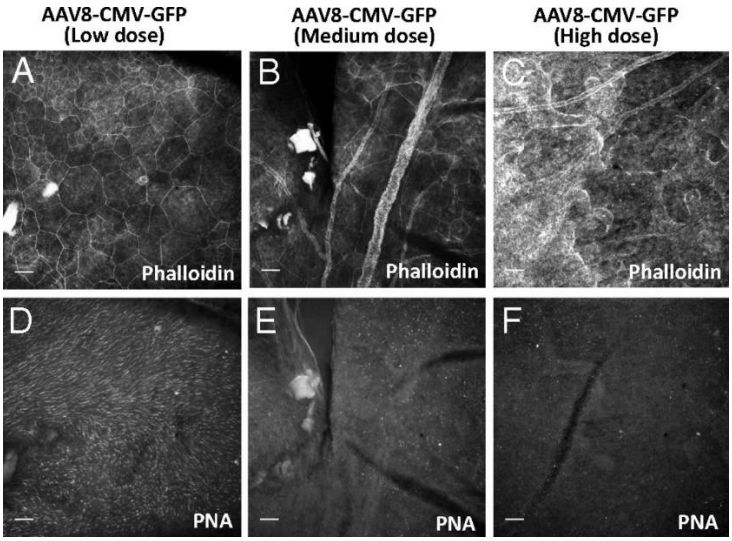

Figure 3. RPE and retina damage are dependent on the dose of the vector.
(**A**-**C**) Representative images of RPE (labeled with phalloidin) from P30 CD-1 mice following infection at P0 with low dose (5E8 vg per eye), medium dose (1E9 vg per eye) and high dose (2E9 vg per eye) of AAV8-CMV-GFP. Scale bar, 50 μm.
(**D**-**F**) Corresponding images of photoreceptors (labeled with PNA) from the same eyes depicted in A-C. Scale bar, 50 μm.

Photoreceptor toxicity was examined in preparations where the RPE and retina were kept together, so that neighboring RPE and photoreceptor cells could be inspected for local effects. Cone OS were stained by peanut agglutinin (PNA), a proxy for photoreceptor health. Severe photoreceptor toxicity was seen at the doses of 1E9 and 2E9 vg per eye such that cone OS were largely absent (Fig. 3*E* and *F*). However, photoreceptors were less sensitive to vector toxicity than RPE, as low-dose (5E8 vg per eye) AAV8-CMV-GFP caused clear abnormalities in RPE morphology while neighboring cone OS were largely normal (Fig. 3*A* and *D*). RPE and cone OS loss were usually found in the same area, which could have resulted from higher local infection or an amplifying effect between compromised RPE and photoreceptors. Damage to the RPE and retina was always restricted to the infected area. When the entire eye was not infected, toxicity did not spread beyond GFP-positive areas. These results show that the severity of RPE and photoreceptor toxicity are positively correlated with the dose of toxic vector, and that photoreceptors are more tolerant of vectors than the RPE. AAV vectors with photoreceptor-specific promoters did not induce toxicity even at the highest doses injected.

Assessment of vector toxicity using clinical measures of visual activity

Human vision can be assayed physiologically using electroretinography (ERG) under lighting conditions that assess for either rod or cone function. Vision in animals can additionally be measured by a behavioral test, the optomotor assay. These assays were applied to C57BL/6J mice injected with AAV8-CMV-GFP at P0. As a non-toxic control, mice were injected with a 5:1 ratio of AAV8-RedO-GFP and AAV8-Best1-GFP to mimic the expression pattern of CMV. For ERG recordings of rods and cones, scotopic (low light levels without background light) and photopic conditions (with background light to saturate rods) were used, respectively. The a-wave provides a measure of photoreceptor function, while the b-wave provides a measurement of signaling between photoreceptors and their synaptic partners, the bipolar cells. Injection of high-dose AAV8-CMV-GFP resulted in a significant drop in the a-wave (−84%, $P<0.001$) and b-wave amplitudes (−71%, $P<0.0001$) in scotopic conditions (Fig. 4*A* and *B*), suggesting a severe functional deficit in rods and the rod pathway. Under photopic conditions, the AAV8-CMV-GFP likewise showed a 50–70% decrease in b-wave amplitudes at all light intensities (Fig. 4*C* and *D*) compared with the combination of AAV8-RedO-GFP and AAV8-Best1-GFP, and approximately a five-fold increase in $I_{1/2}$ (Fig. 4*D*), a measure of the flash intensity giving 50% maximal response (34). These observations indicate that the cone pathway in animals injected with AAV8-CMV-GFP were much less sensitive to light as they required five-fold more photons to reach the 50% maximal response.

Injected mice were also tested in the optomotor assay, which measures visual acuity by assessing the motor response of mice to a virtual rotation of stripes of different widths (35). Consistent with the outcomes of ERG, optomotor showed a deterioration in visual acuity by 30% ($P<0.05$) in the high-dose AAV8-CMV-GFP group (Fig. 4*E*). Together, these results suggest that the retinal damage induced by toxic vectors such as AAV8-CMV-GFP can result in visual deficits.

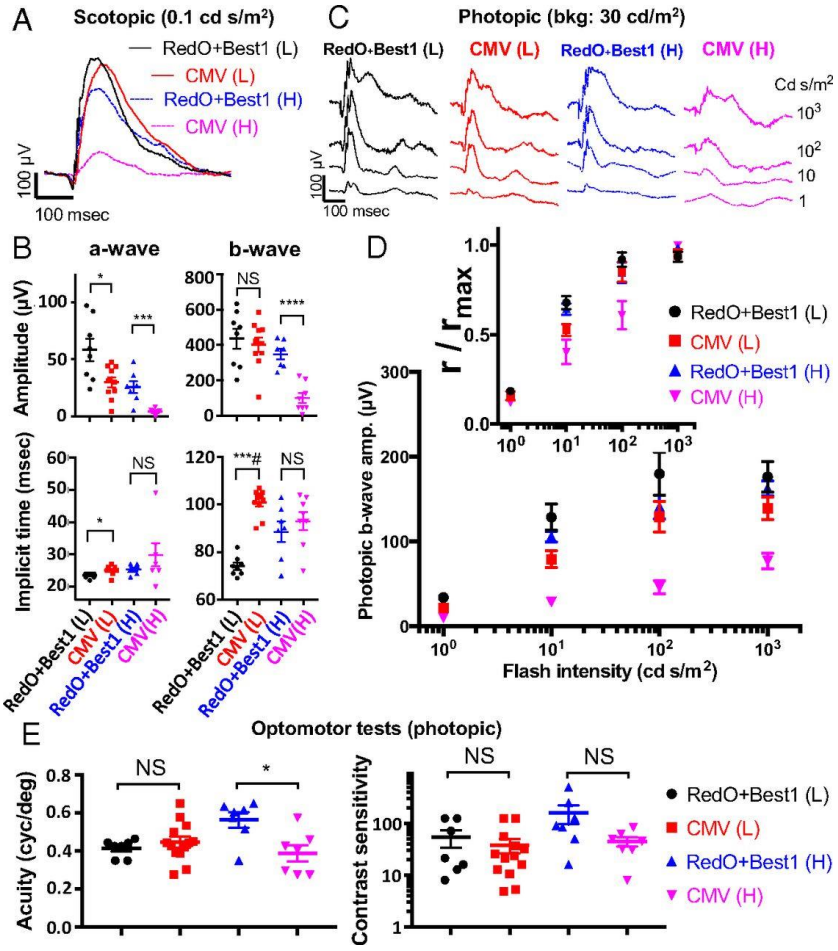

Figure 4. Toxic AAV vectors worsen clinical measures of visual acuity in mice. (**A**) Representative scotopic ERG traces (flash intensity: 0.1 cd s/m^2, wavelength: 530 nm) from P30 C57BL/6J mice injected at P0 with AAV8-RedO-GFP + AAV8-Best1-GFP (5:1 ratio, RedO+Best1) or AAV8-CMV-GFP (CMV) at a low (8E8 vg per eye, L) or high (3E9 vg per eye, H) dose. (**B**) Comparison of scotopic a- and b-wave amplitudes and implicit times from (A). *n* = 7-10 per group. (**C**) Representative photopic ERG traces from P30 C57BL/6J mice injected at P0 with RedO+Best1 or CMV. (**D**) Comparison of photopic b-wave amplitudes from (C). Inset depicts the photopic b-wave intensity-response (r/r_{max}) curves normalized to RedO+Best1. *n* = 7-10 per group. (**E**) Optomotor responses from P35 C57BL/6J mice injected with either RedO+Best1 or CMV. *n* = 7-13 per group. All data shown as mean ± SEM. * P<0.05, *** P<0.001, **** P<0.0001, *# P<1×10^{-6}, ***# P<1×10^{-8} by two-tailed Student's t-test. NS, not significant.

Vector toxicity is associated with microglial activation

Microglia are the main innate immune cell type in the retina (36). We thus examined whether microglia were activated in retinas infected with toxic AAV vectors. Iba1 is a marker of microglia and increases in intensity with activation (37). At 30 days post-infection, there were significantly more Iba1-positive microglia in the retina after infection with high-dose (3E9 vg per eye) AAV8-CMV-GFP (Fig. 5*A*). These microglia migrated to the ONL and subretinal space,

where they adopted an activated amoeboid morphology (Fig. 5*A*). In contrast, microglial number, localization, and morphology did not change significantly in retinas infected with non-toxic vectors such as AAV8-RedO-GFP (Fig. 5*A* and *B*). Microglia were very sensitive to toxic vectors, as their activation was evident even with low-dose (8E8 vg per eye) AAV8-CMV-GFP (Fig. 5*B*). To confirm that microglia numbers were increased, we utilized transgenic Cx3cr1-GFP mice in which microglia are marked by GFP (38). This strain was injected with AAV8-CMV-TdTomato (3E8 vg per eye), which utilizes the same CMV enhancer/promoter as the toxic AAV8-CMV-GFP. The percent of all live retinal cells that were GFP-positive microglia was analyzed using flow cytometry. A three-fold increase of GFP-positive microglia was observed with AAV8-CMV-TdTomato compared to uninjected or PBS-injected retinas (Fig. 5*C*).

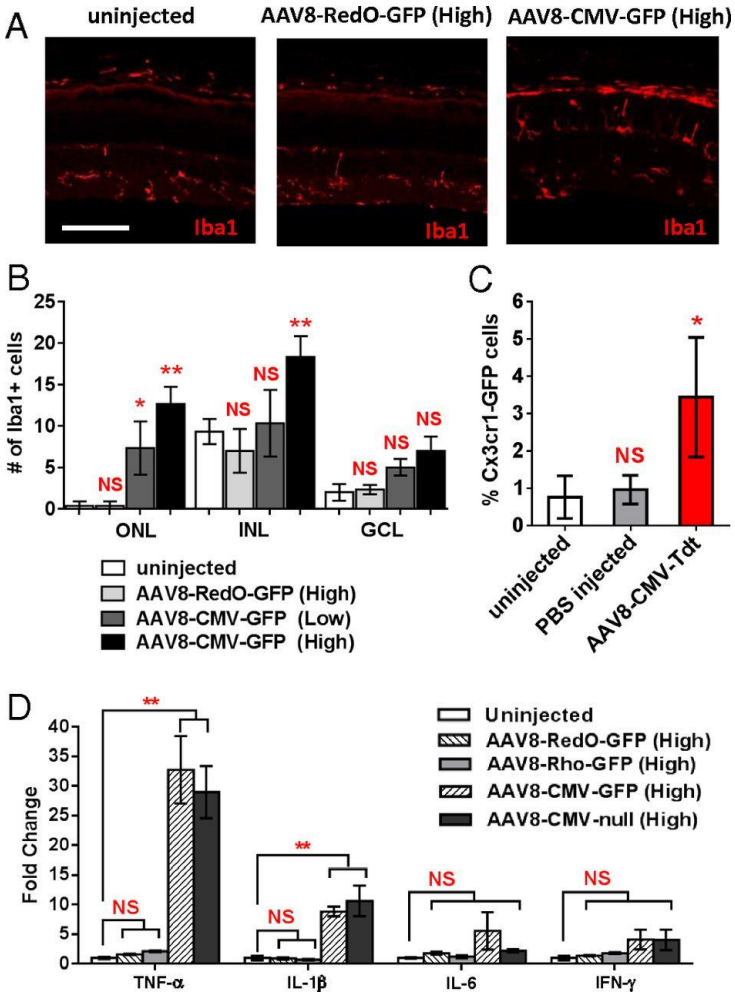

Figure 5. Activation of microglia and innate immune responses by toxic AAV vectors.

(**A**) Iba1 staining in retinal sections from P30 CD-1 mice infected at P0 with the indicated vectors (3E9 vg per eye). Scale bar, 50 μm.

(**B**) Quantification of displaced Iba1-positive cells by cell layer. High = 3E9 vg per eye, Low = 8E8 vg per eye. Data shown as mean ± SD. *n* = 4 per group.

(**C**) Quantification by flow cytometry of retinal microglia from P20 Cx3cr1-GFP mice injected with PBS or AAV8-CMV-TdTomato (3E8 vg per eye). *n* = 3–4 per group. Data shown as mean ± SD.

(**D**) mRNA levels of TNF-α, IL-1β, IL-6, and IFN-γ in retinas from P30 CD-1 mice infected at P0 with the indicated vectors (3E9 vg per eye). Expression levels were normalized to the housekeeping gene *Gapdh*. Data shown as mean ± SEM. *n* = 4–8 per group.

* *P*<0.05, ** *P*<0.01 by one-way ANOVA analysis with Tukey test. NS, not significant between the designated group and the uninjected group.

Upon activation, microglia can increase expression of proinflammatory cytokines, such as TNF-α, IL-1β, IL-6, and IFN-γ. We tested this possibility by examining mRNA levels of these genes by RT-PCR in dissociated retinas at 30 days post-infection. mRNAs for TNF-α and IL-1β were highly upregulated in retinas infected with toxic compared to non-toxic vectors, while levels of IL-6 and IFN-γ were not significantly changed (Fig. 5*D*). The increase in TNF-α and IL-1β mRNAs in these retinas correlated with the dose of the toxic vectors (Fig. 5*D*).

Discussion

Ocular delivery of AAV vectors is relatively safe as shown by the results of several clinical trials (4,6,7,39–41). However, the sensitive assays that we were able to conduct in mice have shown that there can be several manifestations of toxicity from subretinal injections of AAV. Toxicity was seen with multiple vectors and did not correlate with preparation methods, endotoxin level, non-viral protein contamination, or mouse strain. Rather, the two variables showing the strongest association to toxicity were the promoter and the viral dose. It is likely that other variables can in some cases contribute to toxicity (e.g., stocks with a high degree of endotoxin or empty capsids). Nonetheless, our results demonstrate the importance of sensitive and organ-specific assays for different manifestations of toxicity. For ophthalmologists, we anticipate that standard examination equipment and the grading scales developed for clinical studies of uveitis could be employed to measure vector-induced ocular toxicity (42). Moreover, optical coherence tomography (OCT), autofluorescence, and microperimetry are routinely used in preoperative planning for human gene therapy in the eye. In the post-treatment follow-up period, these modalities could be similarly used to quantify changes from baseline across many parameters including retinal layer thickness, infiltration of inflammatory cells, RPE stress, and retinal sensitivity (43,44). These strategies would allow for the development of safer ocular gene therapy vectors, reducing the likelihood of problems as a greater number of patients are treated.

In human clinical trials, the dose of AAV vectors used in subretinal injections ranges from 1E10 to 1E12 vg per eye (20,21,32,33). So far, most ocular gene therapy trials have used AAV2, and thus less is known about the safety and efficacy of AAV8 or other capsid types. However, AAV8, and likely other capsid types under development, offer advantages in terms of number of cells and the cell types infected. In our study, AAV8 encapsidated genomes were toxic at a dose of 5E8 vg per eye or higher. A recent study, also testing subretinal injections in mice, reported similar dose-dependent retinal toxicity with AAV8-CAG-GFP at 5E9 vg per eye and above (17). Across studies, it is often difficult to extrapolate and compare results as different subjects, injection routes, and ages are used. We chose the somewhat unusual time point of P0 for our injections, but this is unlikely to be the cause of the toxicity that we observed. In collaborative studies using pigs, where injections were done to animals at 2 to 3 months of age, toxicity also was seen using AAV8-CMV-GFP (see Chapter 5). Moreover, other studies reporting ocular toxicity used injections in adults (15–20). Another variable complicating comparisons among studies is the issue of vector titer. Different groups use different methods to titer, and even for a given stock, differences of up to 100-fold have been reported (45). Overall, our results, and those of others (14,15,17), emphasize the importance of testing the dose of specific vectors with sensitive assays relevant to the infected cell types. Most assays conducted to date examine only a few parameters, such as neutralizing antisera or gross inflammation and tissue damage.

In light of clinical trials conducted in the eye, it is interesting that two promoters shown to be toxic in our studies have been used safely in humans. The Best1 (also called VMD2) promoter has been used to express the RPE gene, MERTK, to treat one form of retinitis pigmentosa (11,46). The AAV2-VMD2-hMERTK vector, when administered at 4E8 or 4E9 vg per eye in Sprague-Dawley rats, did not cause any obvious retinal damage compared with the saline-injected eyes, although RPE morphology was not examined (46). In the follow-up clinical trial, none of the six patients who received either 5.9E10 vg or 1.8E11 vg of AAV2-VMD2-

hMERTK vector developed severe complications (11). However, in patients with MERTK mutations, there is defective RPE phagocytosis with geographic atrophy at baseline, making it difficult to attribute RPE damage to the vector. In addition to the Best1 promoter, the CAG promoter is used in the LCA2 vector, Luxturna, approved by the Food and Drug Administration (6). Still, since subretinal infections of human eyes result in local infection of ~10% of retinal or RPE cells, the clinical benefits are more limited than what would be ideal. If safer vectors could be developed to transduce a greater number of cells, it would likely benefit many patients.

A key observation in our study is that toxicity correlated with promoter type, with broadly active and RPE promoters leading to toxicity and photoreceptor-specific promoters being benign. Toxicity has also been seen with broadly active promoters in other tissues, including the heart (47,48) and the central nervous system (49,50). However, a systematic investigation of toxicity with these promoters has not been reported. One mechanism that might explain vector toxicity is that the broadly active promoters tend to drive higher expression of transgenes than cell-type–specific promoters. Indeed, GFP protein has been shown to be toxic via reactive oxygen species and apoptosis (51,52). Nonetheless, toxicity cannot be solely attributed to GFP or a protein transgene as AAV8-CMV-null was as toxic as AAV8-CMV-GFP. Another hypothesis is that the CMV sequence, present in both the CMV and CAG vectors, stimulates an innate immune response, as CMV is a virus that naturally activates the innate immune system (53). Arguing against this, the UbiC and Best1 promoters are human in origin but were also toxic. A third possibility is that there is a common sequence motif among the toxic vectors. Toll-like receptor 9 (TLR9), which senses unmethylated CpG DNA, can detect the AAV genome and set off innate and adaptive immune responses (54), and CpG-depleted AAV vectors can evade TLR9-mediated immune detection (55). In examining the vectors tested, we failed to find any correlated sequence motifs. A search for toxic sequences using deletions and chimeric viral genomes may be better able to detect toxic and/or protective sequences.

It is of interest to consider the cell types that might be responsible for vector toxicity. The RPE is situated between the rich vascular bed of the choriocapillaris and the retina, constitutes a portion of the blood-retinal barrier, and expresses at least several genes of the innate immune system, including the TLRs (56). Furthermore, our observations favor the RPE as a primary sensor of toxic vectors, as all toxic vectors had promoters that were active within the RPE, including the RPE-specific promoter, Best1. Two other glial cell types in the retina, Müller glia and astrocytes, can also respond to inflammatory stimuli (57–59). However, Müller glia are not yet born at P0 when we perform our injections, and astrocytes are just beginning to migrate into the retina at this time (60). Microglia also can sense and respond to viruses (61), and given their activation by the toxic but not by the non-toxic vectors, it is likely that they are involved. We did not see GFP in microglia following infection with any vector, but it has been reported that they are difficult to infect *in vivo* (62). The other cell types at the injection site, the photoreceptors, generally do not express genes encoding sensors of innate immunity (61). We thus would not expect these cells to react directly to transcription or vector RNA.

What is being sensed in the RPE and/or microglia? Our data are most consistent with transcription from a non-chromosomal genome or some form of viral RNA. The ITRs in AAV vectors have been shown to possess promoter activity (63,64). If an ITR generates an antisense transcript, it could hybridize to a sense transcript, creating double-stranded RNA, which might then trigger for innate immunity (65). Future analyses of RNA changes following infection with toxic and non-toxic vectors might reveal the primary responders as well as secondary effects. Follow-up studies using genetics in mice may further delineate the responsible pathways and cell types. Although not all studies conducted in mice can be extrapolated to other species, these data can provide a starting point for experiments that are more difficult to conduct in large animals and may be predictive of safer vector structures for human gene therapy.

Materials and Methods

Mice. CD-1 and C57BL/6J mice were purchased from Charles River Laboratories and kept on a 12-h light/12-h dark cycle. All animal procedures performed were approved by the Institutional Animal Care and Use Committee of Harvard University and by Hong Kong Department of Health under Animals Ordinance Chapter 340.

Plasmids. pAAV-CMV-GFP and pAAV-CMV-null vector plasmids were obtained from the Harvard DF/HCC DNA Resource Core. pAAV-UbiC-GFP was made by replacing the CMV promoter in AAV-CMV-GFP with that of human UbiC from Addgene no. 11155 (23,24). pAAV-CAG-GFP (from the E. Boyden laboratory) was obtained from Addgene (no. 37825). pAAV-RedO-GFP, pAAV-Rho-GFP, and pAAV-CAR-GFP were gifts from B. Roska (Friedrich Miescher Institute for Biomedical Research, Basel, Switzerland) (28). pAAV-RK-ZsGreen was a gift from T. Li (National Eye Institute, Bethesda, MD) (29). pAAV-Best1-GFP was cloned by replacing the CMV promoter of the pAAV-CMV-GFP-BGHpA vector with the −585/+39 bp region of human Best1 promoter (26). pAAV-CMV-TdTomato was cloned by replacing GFP with the TdTomato coding sequence. pAAV rep/Cap 2/8 and adenovirus helper plasmids were obtained from University of Pennsylvania Vector Core, Philadelphia.

Vector production and delivery. Recombinant AAV8 vectors were produced, titered, and subretinally injected into P0 mouse eyes as described in Chapter 2.

Histology. For whole eye mounts, enucleated eyes were dissected from tendons and extraocular muscles and fixed in 4% paraformaldehyde for 2 hours at room temperature. The anterior segment, lens, and vitreous were next removed. The posterior segment eye cups were blocked with 4% heat-inactivated goat serum and 1% Triton X-100 in PBS for 1 hour at room temperature. If applicable, eye cups were then incubated with 1:100 of rabbit anti-cone arrestin (EMD Millipore AB15282) in the blocking buffer for 2 days, rinsed three times in PBS for 30 min each, and stained with 1:100 of donkey anti-rabbit Alexa Fluor 647 (Jackson ImmunoResearch) and 1:100 of Alexa Fluor 568-conjugated phalloidin (ThermoFisher) in PBS for 2 days. Following

staining, radial cuts were made to enable flat-mounting of the eyes. Whole-eye mounts were imaged on a Nikon T1 W1 Yokogawa spinning-disk microscope using a 20× objective.

For retinal cross-sections, dissected retinas were fixed and cryo-sectioned as described in Chapter 2. Tissues were blocked in 5% bovine serum albumin in PBS with 0.1% Triton X-100 for one hour at room temperature, followed by staining with primary antibodies at 4 °C overnight. Primary antibodies included rabbit anti-red/green opsin (1:300, AB5405, EMD Millipore); goat anti-blue opsin (1:100, sc-14365, Santa Cruz Biotechnology Inc.); rabbit anti-GFAP (1:500, Z0344, DAKO); rabbit anti-Iba1 (1:1000, PA5-21274, ThermoFisher); and rhodamine-conjugated and FITC-conjugated PNA (1:1000, Vector Laboratories). Sections were subsequently stained with 1:1000 of a secondary antibody from Jackson ImmunoResearch and nuclei visualized with 4′,6-diamidino-2-phenylindole (DAPI) (Thermo Fisher Scientific). Images of retinal cross-sections were acquired as *z*-stacks on a Zeiss LSM780 confocal microscope using a 40× objective. Images used for comparison between groups were taken side-by-side at the same confocal settings.

Assessment of vision. ERG recordings and optomotor responses were measured using the Espion E3 System (Diagonsys LLC) and OptoMotry System (Cerebral Mechanics), respectively, as described in Chapter 2.

Flow cytometry. Retinas from adult Cx3cr1^{GFP} (#005582, The Jackson Laboratory), in which microglia are GFP-positive, were analyzed by flow cytometry as described in Chapter 2.

Statistics. Data are shown as mean ± SD for Figs. 1*C*, 2*B*, 5*B,* and 5*C* and mean ± SEM for Fig. 5D. Two-tailed Student's t-tests were performed to compare two groups and one-way ANOVA with Tukey test for multiple groups. Statistics were performed in GraphPad Prism.

References

1. Gao G, Vandenberghe LH, Alvira MR, Lu Y, Calcedo R, Zhou X, et al. Clades of Adeno-Associated Viruses Are Widely Disseminated in Human Tissues. J Virol. 2004;78(12):6381–8.
2. Dalkara D, Byrne LC, Klimczak RR, Visel M, Yin L, Merigan WH, et al. In Vivo-Directed Evolution of a New Adeno-Associated Virus for Therapeutic Outer Retinal Gene Delivery from the Vitreous. Sci Transl Med. 2013 Jun;5(189):189ra76-189ra76.
3. Zinn E, Pacouret S, Khaychuk V, Turunen HT, Carvalho LS, Andres-Mateos E, et al. In silico reconstruction of the viral evolutionary lineage yields a potent gene therapy vector. Cell Rep. 2015;12(6):1056–68.
4. Bainbridge JWB, Smith AJ, Barker SS, Robbie S, Henderson R, Balaggan K, et al. Effect of gene therapy on visual function in Leber's congenital amaurosis. N Engl J Med. 2008;358:2231–9.
5. Hauswirth WW, Aleman TS, Kaushal S, Cideciyan A V, Schwartz SB, Wang L, et al. Treatment of leber congenital amaurosis due to RPE65 mutations by ocular subretinal injection of adeno-associated virus gene vector: short-term results of a phase I trial. Hum Gene Ther. 2008 Oct;19(10):979–90.
6. Maguire AM, Simonelli F, Pierce EA, Pugh EN, Mingozzi F, Bennicelli J, et al. Safety and Efficacy of Gene Transfer for Leber's Congenital Amaurosis. N Engl J Med. 2008;358:2240–8.
7. Dixon CM, Kusek JW, Ph D, Lepor H, Mcvary KT, Nyberg LM, et al. Adenovirus-Associated Virus Vector–Mediated Gene Transfer in Hemophilia B. Engl J Med. 2011;365:2357–65.
8. Acland GM, Aguirre GD, Ray J, Zhang Q, Aleman TS, Cideciyan a V, et al. Gene therapy restores vision in a canine model of childhood blindness. Nat Genet. 2001;28:92–5.
9. Aguirre GD. Concepts and strategies in retinal gene therapy. Investig Ophthalmol Vis Sci. 2017;58(12):5399–411.
10. Taylor AW. Ocular Immune Privilege and Transplantation. Front Immunol. 2016;7(37):1–7.
11. Ghazi NG, Abboud EB, Nowilaty SR, Alkuraya H, Alhommadi A, Cai H, et al. Treatment of retinitis pigmentosa due to MERTK mutations by ocular subretinal injection of adeno-associated virus gene vector: results of a phase I trial. Hum Genet. 2016;135(3):327–43.
12. MacLaren RE, Groppe M, Barnard AR, Cottriall CL, Tolmachova T, Seymour L, et al. Retinal gene therapy in patients with choroideremia: Initial fi ndings from a phase 1/2 clinical trial. Lancet. 2014;383(9923):1129–37.
13. Mingozzi F, High K a. Immune responses to AAV vectors : overcoming barriers to successful gene. Blood. 2013;122(1):23–36.
14. Hinderer C, Katz N, Buza EL, Dyer C, Goode T, Bell P, et al. Severe toxicity in nonhuman primates and piglets following high-dose intravenous administration of an AAV vector expressing human SMN. Hum Gene Ther. 2018;29(3):hum.2018.015.
15. Vandenberghe LH, Bell P, Maguire AM, Cearley CN, Xiao R, Calcedo R, et al. Dosage thresholds for AAV2 and AAV8 photoreceptor gene therapy in monkey. Sci Transl Med. 2011 Jun;3(88):88ra54.
16. Ramachandran PS, Lee V, Wei Z, Song JY, Casal G, Cronin T, et al. Evaluation of Dose and Safety of AAV7m8 and AAV8BP2 in the Non-Human Primate Retina. Vol. 28, Human Gene Therapy. 2017. 154–167 p.
17. Khabou H, Cordeau C, Pacot L, Fisson S, Dalkara D. Dosage thresholds and influence of transgene cassette in AAV-related toxicity. Hum Gene Ther. 2018;hum.2018.144.
18. Gootwine E, Ofri R, Banin E, Obolensky A, Averbukh E, Ezra-Elia R, et al. Safety and Efficacy Evaluation of rAAV2tYF-PR1.7-hCNGA3 Vector Delivered by Subretinal Injection in CNGA3 Mutant Achromatopsia Sheep. Hum Gene Ther Clin Dev. 2017;28(2):96–107.
19. Reichel FF, Dauletbekov DL, Klein R, Peters T, Ochakovski GA, Seitz IP, et al. AAV8 Can Induce Innate and Adaptive Immune Response in the Primate Eye. Mol Ther. 2017 Dec 6;25(12):2648–60.
20. Bainbridge JWB, Mehat MS, Sundaram V, Robbie SJ, Barker SE, Ripamonti C, et al. Long-Term

Effect of Gene Therapy on Leber's Congenital Amaurosis. N Engl J Med. 2015;372(20):1887–97.

21. Dimopoulos IS, Hoang SC, Radziwon A, Binczyk NM, Seabra MC, MacLaren RE, et al. Two-Year Results After AAV2-Mediated Gene Therapy for Choroideremia: The Alberta Experience. Am J Ophthalmol. 2018;193:130–42.
22. Boshart M, Weber F, Jahn G, Dorsch-Häsler K, Fleckenstein B, Schaffner W. A very strong enhancer is located upstream of an immediate early gene of human cytomegalovirus. Cell. 1985 Jun;41(2):521–30.
23. Schorpp M, Jäger R, Schellander K, Schenkel J, Wagner EF, Weiher H, et al. The human ubiquitin C promoter directs high ubiquitous expression of transgenes in mice. Nucleic Acids Res. 1996;24(9):1787–8.
24. Lois C, Hong EJ, Pease S, Brown EJ, Baltimore D. Germline Transmission and Tissue-Specific Expression of Transgenes Delivered by Lentiviral Vectors. Science. 2002;295:868–72.
25. Niwa H, Yamamura K, Miyazaki J. Efficient selection for high-expression transfectants with a novel eukaryotic vector. Gene. 1991 Dec;108:193–200.
26. Esumi N, Oshima Y, Li Y, Campochiaro PA, Zack DJ. Analysis of the *VMD2* Promoter and Implication of E-box Binding Factors in Its Regulation. J Biol Chem. 2004 Apr 30;279(18):19064–73.
27. Allocca M, Mussolino C, Garcia-Hoyos M, Sanges D, Iodice C, Petrillo M, et al. Novel adeno-associated virus serotypes efficiently transduce murine photoreceptors. J Virol. 2007 Oct;81(20):11372–80.
28. Busskamp V, Duebel J, Balya D, Fradot M, James T, Viney TJ, et al. Genetic reactivation of cone photoreceptors restore visual responses in Retinitis pigmentosa. Science. 2010;329(July):413–7.
29. Khani SC, Pawlyk BS, Bulgakov O V., Kasperek E, Young JE, Adamian M, et al. AAV-Mediated Expression Targeting of Rod and Cone Photoreceptors with a Human Rhodopsin Kinase Promoter. Invest Ophthalmol Vis Sci. 2007 Sep;48(9):3954–61.
30. Zhu X, Ma B, Babu S, Murage J, Knox BE, Craft CM. Mouse cone arrestin gene characterization: Promoter targets expression to cone photoreceptors. FEBS Lett. 2002;524(1–3):116–22.
31. Xiong W, Garfinkel AEM, Li Y, Benowitz LI, Cepko CL. NRF2 promotes neuronal survival in neurodegeneration and acute nerve damage. J Clin Invest. 2015;125(4):1433–45.
32. Constable IJ, Lai CM, Magno AL, French MA, Barone SB, Schwartz SD, et al. Gene Therapy in Neovascular Age-related Macular Degeneration: Three-Year Follow-up of a Phase 1 Randomized Dose Escalation Trial. Am J Ophthalmol. 2017;177:150–8.
33. Maguire AM, High KA, Auricchio A, Wright JF, Pierce EA, Testa F, et al. Age-dependent effects of RPE65 gene therapy for Leber's congenital amaurosis: a phase 1 dose-escalation trial. Lancet. 2009;374:1597–605.
34. Vinberg F, Wang T, De Maria A, Zhao H, Bassnett S, Chen J, et al. The Na(+)/Ca(2+), K(+) exchanger NCKX4 is required for efficient cone-mediated vision. Rieke F, editor. Elife. 2017 Jun;6:e24550.
35. Prusky GT, Alam NM, Beekman S, Douglas RM. Rapid quantification of adult and developing mouse spatial vision using a virtual optomotor system. Invest Ophthalmol Vis Sci. 2004 Dec;45(12):4611–6.
36. Silverman SM, Wong WT. Microglia in the Retina: Roles in Development, Maturity, and Disease. Annu Rev Vis Sci. 2018 Sep 15;4(1):45–77.
37. Ito D, Imai Y, Ohsawa K, Nakajima K, Fukuuchi Y, Kohsaka S. Microglia-specific localisation of a novel calcium binding protein, Iba1. Mol Brain Res 57. 1998;57:1–9.
38. Jung S, Aliberti J, Graemmel P, Sunshine MJ, Kreutzberg GW, Sher A, et al. Analysis of fractalkine receptor CX(3)CR1 function by targeted deletion and green fluorescent protein reporter gene insertion. Mol Cell Biol. 2000 Jun;20(11):4106–14.
39. Cideciyan A V., Aleman TS, Boye SL, Schwartz SB, Kaushal S, Roman AJ, et al. Human gene therapy for RPE65 isomerase deficiency activates the retinoid cycle of vision but with slow rod kinetics. Proc Natl Acad Sci. 2008;105(39):15112–7.

40. Feuer WJ, Schiffman JC, Davis JL, Porciatti V, Gonzalez P, Koilkonda RD, et al. Gene Therapy for Leber Hereditary Optic Neuropathy: Initial Results. Ophthalmology. 2016 Mar;123(3):558–70.
41. Cukras C, Wiley HE, Jeffrey BG, Sen HN, Turriff A, Zeng Y, et al. Retinal AAV8-RS1 Gene Therapy for X-Linked Retinoschisis: Initial Findings from a Phase I/IIa Trial by Intravitreal Delivery. Mol Ther. 2018 Sep 5;26(9):2282–94.
42. Jabs DA, Nussenblatt RB, Rosenbaum JT, Atmaca LS, Becker MD, Brezin AP, et al. Standardization of uveitis nomenclature for reporting clinical data. Results of the first international workshop. Am J Ophthalmol. 2005 Sep 1;140(3):509–16.
43. Xue K, Groppe M, Salvetti AP, MacLaren RE. Technique of retinal gene therapy: Delivery of viral vector into the subretinal space. Eye. 2017 Sep 1;31(9):1308–16.
44. Li Y, Lowder C, Zhang X, Huang D. Anterior chamber cell grading by optical coherence tomography. Investig Ophthalmol Vis Sci. 2013 Jan;54(1):258–65.
45. Ayuso E, Blouin V, Lock M, McGorray S, Leon X, Alvira MR, et al. Manufacturing and Characterization of a Recombinant Adeno-Associated Virus Type 8 Reference Standard Material. Hum Gene Ther. 2014;25(11):977–87.
46. Conlon TJ, Deng W-T, Erger K, Cossette T, Pang J, Ryals R, et al. Preclinical Potency and Safety Studies of an AAV2-Mediated Gene Therapy Vector for the Treatment of *MERTK* Associated Retinitis Pigmentosa. Hum Gene Ther Clin Dev. 2013;24(1):23–8.
47. Ai J, He Y, Zheng M, Wen Y, Zhang H, Huang F, et al. Characterization of Recombinant Adeno-Associated Viral Transduction and Safety Profiles in Cardiomyocytes. Cell Physiol Biochem. 2018;48(5):1894–900.
48. Merentie M, Lottonen-Raikaslehto L, Parviainen V, Huusko J, Pikkarainen S, Mendel M, et al. Efficacy and safety of myocardial gene transfer of adenovirus, adeno-associated virus and lentivirus vectors in the mouse heart. Gene Ther. 2016;23(3):296–305.
49. Klein RL, Dayton RD, Leidenheimer NJ, Jansen K, Golde TE, Zweig RM. Efficient neuronal gene transfer with AAV8 leads to neurotoxic levels of tau or green fluorescent proteins. Mol Ther. 2006;13(3):517–27.
50. Watakabe A, Ohtsuka M, Kinoshita M, Takaji M, Isa K, Mizukami H, et al. Comparative analyses of adeno-associated viral vector serotypes 1, 2, 5, 8 and 9 in marmoset, mouse and macaque cerebral cortex. Neurosci Res. 2015;93:144–57.
51. Ansari AM, Ahmed AK, Matsangos AE, Lay F, Born LJ, Marti G, et al. Cellular GFP Toxicity and Immunogenicity: Potential Confounders in in Vivo Cell Tracking Experiments. Stem Cell Rev Reports. 2016;12(5):553–9.
52. Liu H-S, Jan M-S, Chou C-K, Chen P-H, Ke N-J. Is Green Fluorescent Protein Toxic to the Living Cells? Biochem Biophys Res Commun. 1999;260(3):712–7.
53. Loewendorf A, Benedict CA. Modulation of host innate and adaptive immune defenses by cytomegalovirus: timing is everything. J Intern Med. 2010;267(5):483–501.
54. Zhu J, Huang X, Yang Y. The TLR9-MyD88 pathway is critical for adaptive immune responses to adeno- associated virus gene therapy vectors in mice. J Clin Invest. 2016;119(8):2388–98.
55. Faust SM, Bell P, Cutler BJ, Ashley SN, Zhu Y, Rabinowitz JE, et al. CpG-depleted adeno-associated virus vectors evade immune detection. J Clin Invest. 2013;123(7):2994–3001.
56. Kumar MV, Nagineni CN, Chin MS, Hooks JJ, Detrick B. Innate immunity in the retina: Toll-like receptor (TLR) signaling in human retinal pigment epithelial cells. J Neuroimmunol. 2004;153(1–2):7–15.
57. Jiang G, Ke Y, Sun D, Wang Y, Kaplan HJ, Shao H. Regulatory role of TLR ligands on the activation of autoreactive T cells by retinal astrocytes. Investig Ophthalmol Vis Sci. 2009;50(10):4769–76.
58. Jiang G, Sun D, Kaplan HJ, Shao H. Retinal astrocytes pretreated with NOD2 and TLR2 ligands activate uveitogenic t cells. PLoS One. 2012;7(7):1–9.
59. Kumar A, Shamsuddin N. Retinal muller glia initiate innate response to infectious stimuli via toll-like receptor signaling. PLoS One. 2012;7(1).

60. Kautzman AG, Keeley PW, Nahmou MM, Luna G, Fisher SK, Reese BE. Sox2 regulates astrocytic and vascular development in the retina. Glia. 2018;66(3):623–36.
61. Lannes N, Eppler E, Etemad S, Yotovski P, Filgueira L. Microglia at center stage: a comprehensive review about the versatile and unique residential macrophages of the central nervous system. Oncotarget. 2017;8(69):114393–413.
62. Rosario AM, Cruz PE, Ceballos-Diaz C, Strickland MR, Siemienski Z, Pardo M, et al. Microglia-specific targeting by novel capsid-modified AAV6 vectors. Mol Ther - Methods Clin Dev. 2016;3:16026.
63. Haberman RP, McCown TJ, Samulski RJ. Novel Transcriptional Regulatory Signals in the Adeno-Associated Virus Terminal Repeat A/D Junction Element. J Virol. 2000 Sep 15;74(18):8732–9.
64. Flotte TR, Afione SA, Solow R, Drumm ML, Markakis D, Guggino WB, et al. Expression of the cystic fibrosis transmembrane conductance regulator from a novel adeno-associated virus promoter. J Biol Chem. 1993;268(5):3781–90.
65. Schlee M, Hartmann G. Discriminating self from non-self in nucleic acid sensing. Vol. 16, Nature Reviews Immunology. Nature Publishing Group; 2016. p. 566–80.

Chapter 5: Engineering adeno-associated viral vectors to evade innate immune and inflammatory responses

Abstract

Nucleic acids are utilized in many therapeutic modalities, including gene therapy, but as discussed in Chapter 4, their ability to trigger host immune responses *in vivo* can lead to decreased safety and efficacy. In the case of adeno-associated viral (AAV) vectors, studies have shown that the DNA genome of the vector activates Toll-like receptor 9 (TLR9), a pattern recognition receptor that senses foreign DNA. TLR9 signaling activates inflammatory and innate immune defenses that subsequently promote the development of adaptive T cell responses against the AAV capsid protein. As AAV gene therapy begins to see success in the clinic, a wealth of data indicates that inflammation and T cell responses can not only hamper therapeutic benefit, but in some cases, permanently worsen outcomes. Here, we engineered AAV vectors to be intrinsically less immunogenic by incorporating short DNA oligonucleotides that antagonize TLR9 activation directly into the vector genome. The engineered vectors elicited markedly reduced innate immune and T cell responses and enhanced gene expression in clinically relevant animal models across different tissues. In particular, we demonstrated that subretinal administration of higher dose AAV vectors in a large animal model resulted in photoreceptor pathology with infiltration by microglia and T cells, which were avoided in contralateral eyes that received the engineered vectors. Our results highlight the vector genome as a key source of immunogenicity in AAV gene therapy and demonstrate the concept of linking specific immunomodulatory non-coding sequences to much longer therapeutic nucleic acids to “cloak” the vector from inducing unwanted immune responses. This “coupled immunomodulation” strategy may widen the therapeutic window for the numerous AAV therapies being explored as well as other DNA-based gene transfer methods.

Contributions

Ying Kai Chan[1,2], Sean K. Wang[2], Colin J. Chu[3], David, A. Copland[3], Alexander J. Letizia[1,2], Helena Costa Verdera[4,5], Jessica J. Chiang[1,2], Meher Sethi[1,2], Yingleong Chan[1,2], Elaine T. Lim[1,2], Amanda R. Graveline[1], Melinda Sanchez[1], Priscilla J. Alphonse[4,5], Yunlu Xue[2], Lindsey R. Robinson-McCarthy[1,2], Jenny M. Tam[1,2], Maha H. Jabbar[6], Bhubanananda Sahu[6], Janelle F. Adeniran[6], Manish Muhuri[7,8,9], Phillip W.L. Tai[7,8,9], Jun Xie[7,8,9], Tyler B. Krause[2], Andyna Vernet[1], Matthew Pezone[1], Ru Xiao[10,11], Tina Liu[1,2], Wei Wang[6], Henry J. Kaplan[6], Guangping Gao[7,8,9], Andrew D. Dick[3,12], Federico Mingozzi[4,5], Maureen A. McCall[6,13], Constance L. Cepko[2,14], George M. Church[1,2]

[1] Wyss Institute for Biologically Inspired Engineering, Harvard University, Boston, MA, USA

[2] Departments of Genetics and Ophthalmology, Harvard Medical School, Boston, MA, USA

[3] Academic Unit of Ophthalmology, Translational Health Sciences, University of Bristol, Bristol, United Kingdom

[4] Inserm U974, Sorbonne Universite, Paris, France

[5] Inserm S951 and Genethon, Evry, France

[6] Department of Ophthalmology and Visual Sciences, University of Louisville, Louisville, KY, USA

[7] Horae Gene Therapy Center, University of Massachusetts Medical School, Worcester, MA, USA

[8] Li Weibo Institute for Rare Diseases Research, University of Massachusetts Medical School, Worcester, MA, USA

[9] Department of Microbiology and Physiological Systems, University of Massachusetts Medical School, Worcester, MA, USA

[10] Grousbeck Gene Therapy Center, Schepens Eye Research Institute and Massachusetts Eye and Ear Infirmary, Boston, MA, USA

[11] Ocular Genomics Institute, Department of Ophthalmology, Harvard Medical School, Boston, MA, USA

[12] Institute of Ophthalmology and the National Institute for Health Research Biomedical Research Centre, Moorfields Eye Hospital and University College London, London, United Kingdom

[13] Department of Anatomical Sciences and Neurobiology, University of Louisville, Louisville, KY

[14] Howard Hughes Medical Institute, Harvard Medical School, Boston, MA, USA

Y.K.C. and G.M.C. conceived the study; Y.K.C., S.K.W., C.J.C., D.A.C., A.J.L., H.C.V., J.J.C., M.S., Y.C., E.T.L., A.R.G., M.S., P.J.A., Y.X., L.R.R., J.M.T., M.H.J., B.S., J.F.A., M.M., P.W.T., J.X., T.B.K., A.V., M.P., R.X. and W.W. designed research, performed experiments, and analyzed data; Y.K.C. and G.M.C. wrote the paper with contributions from S.K.W., C.J.C., D.A.C., and M.A.M.

Note: This work has been submitted for publication and is currently in revision at *Nature*. For brevity, some sections have been omitted.

Introduction

Gene therapy holds exciting promise for treating multiple genetic disorders, but host immune responses pose a major challenge for *in vivo* gene transfer (1). While adeno-associated viral (AAV) vectors are known to be much less immunogenic than other viral vectors such as adenoviruses, preclinical and clinical studies have demonstrated dose-dependent inflammation, which can reduce efficacy and lead to dose-limiting toxicity (2–6). These include examples such as ocular AAV therapies leading to a permanent reduction in visual acuity following intraocular inflammation (7–9), and liver-directed therapies resulting in liver transaminase elevations which coincide with decreased factor IX (FIX) transgene expression, likely due to AAV capsid-specific cytotoxic T cells destroying transduced hepatocytes (5,6).

Several studies have demonstrated a central role for Toll-like receptor 9 (TLR9), an immune sensor of DNA, in detecting AAV genomes and triggering innate immune and CD8+ T cell responses that inhibit AAV gene therapy (10–12). TLRs are a family of innate immune sensors conserved across mammalian species that are found on endosomal or plasma membranes of immune cells (13). TLR9 normally senses DNA from pathogenic viruses and bacteria that contains unmethylated cytosine-phosphate-guanine (CpG) motifs, which are also present in AAV genomes. CpG binding to TLR9 promotes its dimerization and activates TLR9 signaling via the signaling adaptor MyD88, leading to induction of type I interferons (IFNs) and pro-inflammatory cytokines. Innate immune responses like interferon induction trigger an antiviral state among cells, while inflammation recruits other immune cells to the site of infection and primes adaptive immune responses (10,11).

One strategy for blocking TLR9 activation is the administration of specific short single-stranded DNA oligonucleotides (typically 12-24 nucleotide [nt]) that antagonize TLR9 activation (hereby termed “TLR9i” for TLR9-inhibitory). Structural studies recently described two different TLR9i sequences that formed stem-loop structures that fit snugly into the interior of the ring structure of TLR9, preventing dimerization and activation (15). Furthermore, the binding site of

TLR9i oligonucleotides on TLR9 partially overlapped with that of CpG DNA, and the TLR9i oligonucleotide tested possessed higher binding affinity for TLR9 than CpG DNA. TLR9i sequences have been tested extensively in the literature as a standalone agent co-administered with inflammatory DNA ligands, but this strategy likely requires a large amount of oligonucleotide to inhibit all TLR9 molecules, which may not be feasible especially in the context of an organism. Here, we hypothesized that the immune-inhibitory activity of short TLR9i sequences remain functional in a much longer strand of DNA and can be utilized for dampening immune responses to AAV vectors by directly incorporating them in the vector genome.

Results and Discussion

We first selected multiple TLR9i sequences described in the literature and individually linked each of them directly to a 24 nt-long highly inflammatory oligodeoxyribonucleotide (ODN), ODN *2006*, which contains 4 CpG sites (16), resulting in fusion constructs hereafter termed "ODN *2006*-TLR9i". Using a TLR9 reporter cell assay, we observed that treatment of cells with ODN *2006*-TLR9i oligonucleotides resulted in markedly reduced NF-kB response compared to ODN *2006* linked to two separate control sequences not expected to stimulate or inhibit TLR9 (*control1* or *control2*), demonstrating that TLR9i sequences are able to function *in cis* (Supplemental Fig. 1). Insertion of a 5 nt intervening sequence (AAAAA) between ODN *2006* and TLR9i sequences yielded similar results, as well as when the order of ODN *2006* and the TLR9i sequence was reversed (Supplemental Fig. 1). We identified a condition in which ODN *2006*-*control2* (*in cis*) gave comparable NF-kB response as ODN *2006* and *control2* co-administered at the same concentration (*in trans*) and observed that ODN *2006*-*TTAGGG* blocked ~80% of induced NF-kB response, while co-administration of ODN *2006* and *TTAGGG* only inhibited ~35% of it (Supplemental Fig. 1). Thus, incorporation of a TLR9i sequence within the same molecule as an inflammatory DNA sequence can be more effective at dampening inflammation than administering it as a separate molecule. ODN *TTAGGG*, a well-known TLR9i

sequence derived from mammalian telomeres (17), did not inhibit the activation of TLR7 or TLR2/6 (sensors of microbial RNA and lipoproteins, respectively) even at high concentration, supporting its specificity for TLR9 (Supplemental Fig. 1).

Next, we evaluated the ability of TLR9-inhibitory sequences incorporated within AAV genomes to reduce innate and adaptive immune responses to gene therapy *in vivo*. We used multiple clinically relevant target tissues and routes of administration in both small and large animal models: 1) liver following an intravenous injection in mice, 2) skeletal muscle via direct intramuscular injection in mice, 3) retina following an intravitreal injection in mice, and 4) retina following a subretinal injection in outbred pigs. In addition, we tested primary human immune cells for innate immune responses *in vitro.*

We first inserted an oligonucleotide consisting of three copies of ODN *TTAGGG* separated by short AAAAA linkers (Fig. 1*A*, "io1" for "inflammation-inhibiting oligonucleotide 1") into the 5' untranslated region (UTR) of a self-complementary (sc) AAV vector plasmid encoding human FIX under the control of a liver-specific transthyretin (TTR) promoter (11). We chose scAAV vectors for proof-of-concept as they have been shown to trigger TLR9-dependent innate immune responses in the liver of mice efficiently after intravenous administration (11).

As expected, systemic administration of 1 x 10^{11} vector genomes (vg) (equivalent to ~4x 10^{12} vg/kg, a therapeutically relevant dose in the clinic) of scAAV8.FIX in mice stimulated moderate type I interferon (*Ifnb1* and *Ifna13*) gene expression in the liver at 2 hours post-injection (hpi), the peak time point as previously described (11). In contrast, the same dose of scAAV8.FIX.io1 elicited no detectable innate immune responses in the liver (Fig. 1*B*). scAAV8.FIX.io1 treatment also did not elevate interferon gene expression compared to phosphate-buffered saline (PBS) 4 hpi (data not shown). Administration of 10-fold lower doses (1 x 10^{10} vg) of either scAAV8.FIX or scAAV8.FIX.io1 did not trigger interferon responses in the liver, consistent with the immune response being AAV-dose dependent (Fig. 1*C*). We confirmed with *Myd88*$^{-/-}$ mice that the innate immune response was indeed dependent on the TLR9/MyD88

pathway (Fig. 1*D*), as shown in the literature (10–12). While scAAV8.FIX stimulated macrophage infiltration of the liver, scAAV.FIX.io1 avoided immune cell infiltration (Fig. 1*E*).

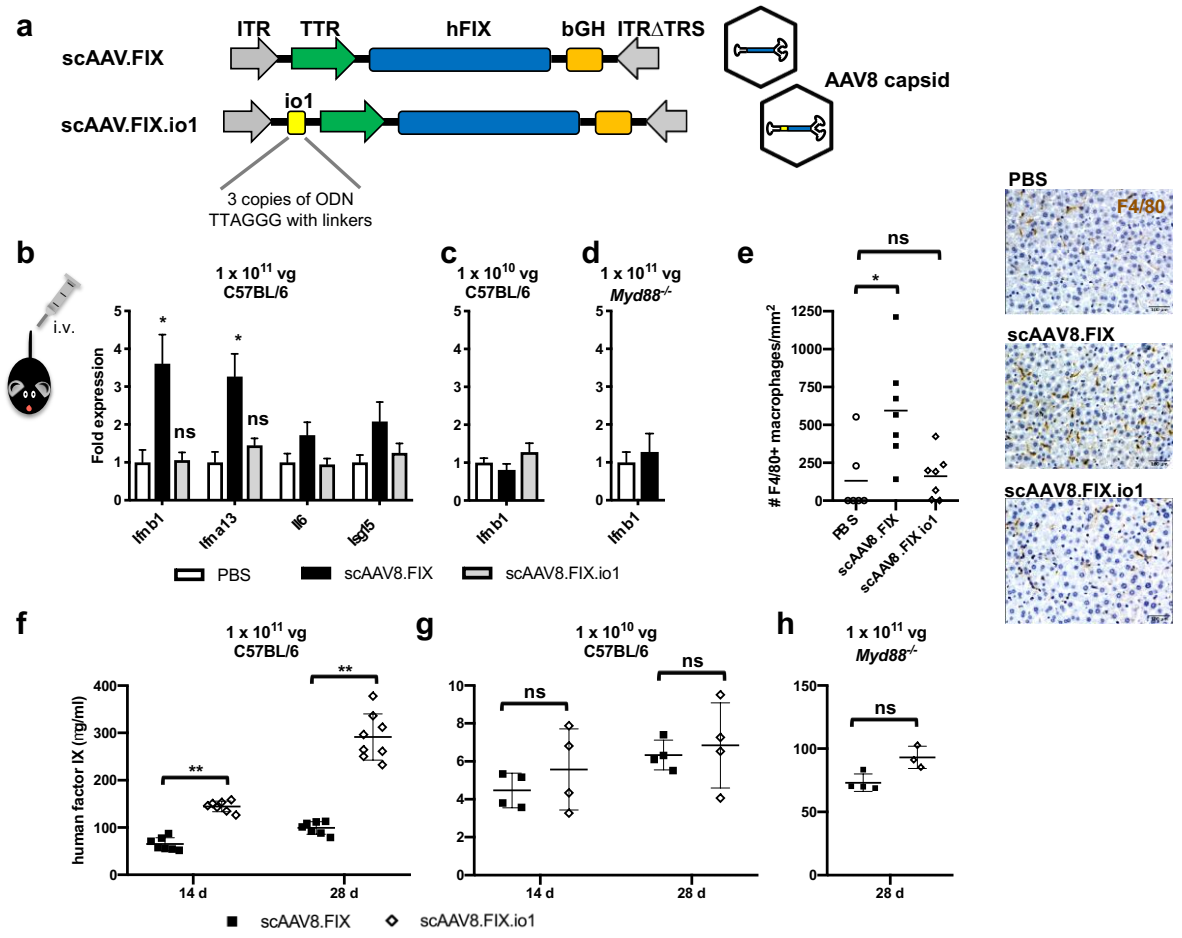

Figure 1. Innate immune response and human FIX expression in mice following intravenous AAV8 administration. (**A**) Schematic diagram of scAAV.FIX and scAAV.FIX.io1. The io1 sequence is not expected to be transcribed or translated due to its placement in an untranslated region upstream of the promoter. (**B-D**) Innate immune response in liver assayed by RT-PCR 2 hours after AAV8 administration. Fold changes are relative to PBS injection. *n* = 4-7 animals per group. * *P*<0.05 by two-tailed Mann-Whitney test compared to PBS. (**E**) F4/80+ macrophage infiltration in liver 2 hours after AAV8 administration. Scale bar, 100 μm. *n* = 6-7 animals per group. * *P*<0.005 by two-tailed Mann-Whitney test. (**F-H**) hFIX levels in plasma of mice at indicated time points. *n* = 3-8 animals per group. ** *P*<0.005 by two-tailed Mann-Whitney test. Data shown as mean ± SEM for (B-D), mean ± SD for (F-H). ITR, inverted terminal repeat; TTR, transthyretin promoter; hFIX, human factor IX; bGH, bovine growth hormone poly(A) signal; TRS, terminal resolution site; ns, not significant.

When we studied transgene expression, we observed that scAAV8.FIX.io1 enhanced human FIX levels in plasma nearly three-fold compared to scAAV8.FIX 28 days post-injection (dpi) (Fig. 1*F*), consistent with published findings that *Tlr9*$^{-/-}$ mice expressed higher FIX levels than wild-type mice after AAV treatment and substantiating an important role for TLR9-mediated

immune responses in AAV transgene expression (11). In experimental settings where an innate immune response was not triggered (using 10-fold lower doses of vector or *Myd88*$^{-/-}$ mice), scAAV8.FIX.io1 did not lead to an enhancement in FIX expression (Fig. 1*G* and *H*), suggesting that the two vectors do not have inherently different potencies. We observed the development of comparable amounts of neutralizing antibody (NAb) titers at 28 dpi against AAV8 for both scAAV8.FIX and scAAV8.FIX.io1 (data not shown), in agreement with previous observations that *Tlr9*$^{-/-}$ and wild-type mice develop similar antibody titers (11). Together, these results indicate that incorporation of io1 into an scAAV vector evades innate immune responses in the liver and enhances transgene expression following intravenous administration.

While dose-dependent immune responses are well-appreciated following systemic AAV vector delivery in humans, robust T cell responses are generally not observed by this route in mice. Similarly, we were unable to detect appreciable CD8+ T cell responses against AAV8 capsid via an IFN-gamma enzyme-linked immune absorbent spot (ELISpot) assay in our intravenous scAAV8.FIX experiments (data not shown). To test the effect of our strategy on anti-capsid T cell responses, we modeled a more immunogenic condition in mice by utilizing intramuscular delivery and AAVrh32.33 capsid (rh32.33), a uniquely immunogenic capsid in mice. This combination has been shown to elicit robust CD8+ T cell responses against rh32.33 capsid and local infiltration of cytotoxic T cells into muscle in a TLR9-dependent manner (12,18). We tested single-stranded AAV vectors, which are more widely used because of their larger coding capacity. We observed that at a dose of 1 x 10^{10} vg injected into the quadriceps muscle, rh32.33.GFP triggered a range of CD8+ T cell responses against an immunodominant capsid epitope via ELISpot at 21 dpi, with 7 of 10 animals showing positive T cell reactivity (Fig. 2*A*). In contrast, rh32.33.GFP.io2, which harbors inflammation-inhibiting oligonucleotide 2 (io2) designed for single-stranded vectors (Supplemental Fig. 2), showed almost no CD8+ T cell response (1 of 10 animals positive) and was not statistically different from PBS treatment. We confirmed with *Myd88*$^{-/-}$ mice that development of CD8+ T cell responses against rh32.33 capsid

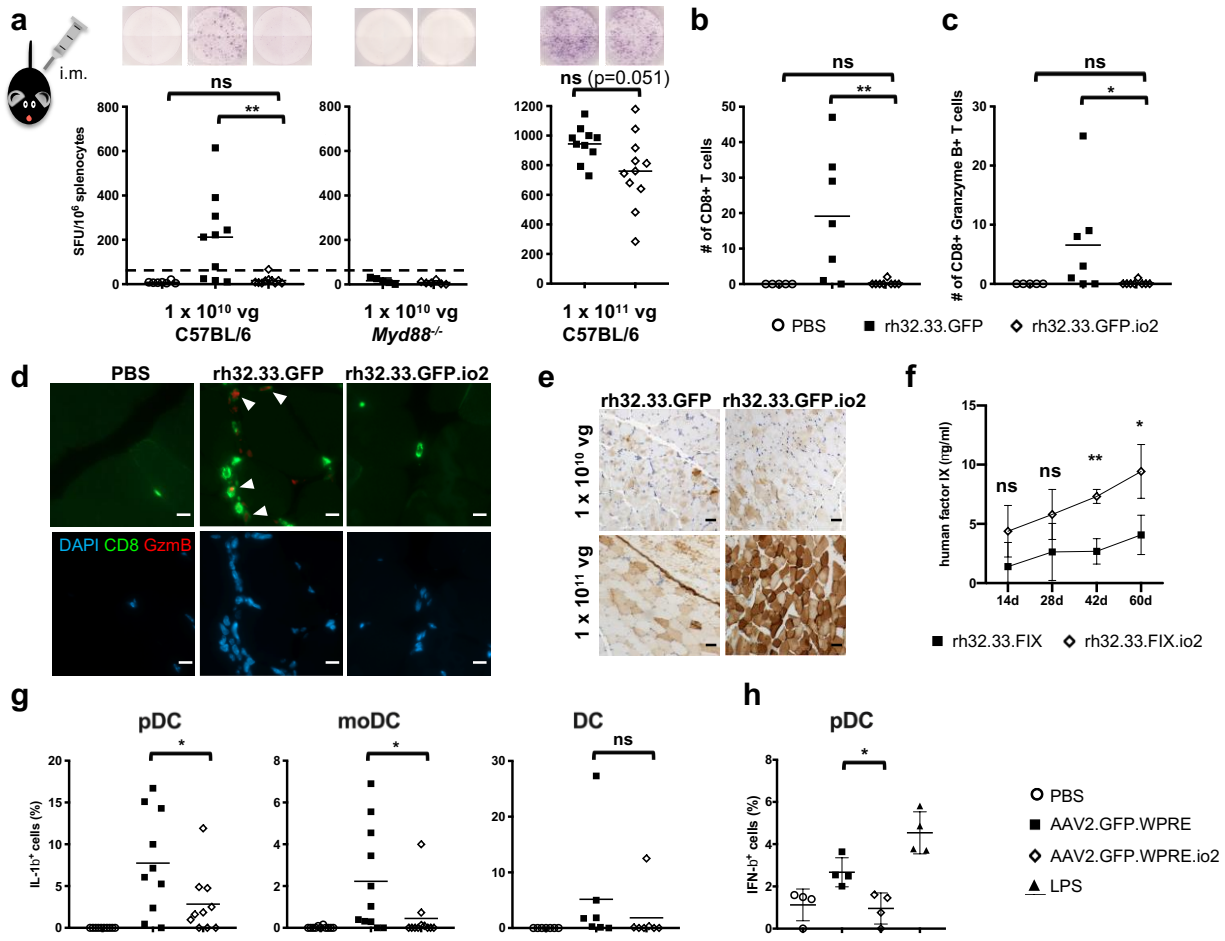

Figure 2. Immune responses to single-stranded vectors in mouse skeletal muscle *in vivo* and human PBMCs *in vitro*. (**A**) CD8+ T cell responses to rh32.33 capsid 21 days after intramuscular injections. Representative images of the ELISpot well are shown. Dotted line (50 SFU/10^6 splenocytes) indicates cutoff for a positive T cell response. (**B-D**) Number of CD8+ T cells and CD8+ Granzyme B+ T cells in the muscle sections (four fields per sample) for PBS and 10^{10} vg rh32.33 vectors. White arrows indicate double positive cells. Scale bar, 10 μm. (**E**) Representative images of GFP expression (brown) by immunohistochemistry staining in muscle sections. Scale bar, 50 μm. (**F**) Human FIX levels in plasma of mice at indicated time points following 1x 10^{11} vg rh32.33 vector administration. *n* = 4 animals per group. Data shown as mean ± SD. (**G-H**) Intracellular cytokine staining of IL-1β (*n* = 7-13) or IFN-β (*n* = 4-7) in specific dendritic cell (DC) populations 24 hours after infection of primary human peripheral blood mononuclear cells (PBMCs) from different donors. * *P*<0.05, ** *P*<0.005 by two-tailed Mann-Whitney test for (A-D), two-way ANOVA with Sidak's post-hoc test for (F), two-tailed Wilcoxon matched-pairs signed ranked test for (G), and two-tailed Student's t-test for (H). not significant; SFU, spot forming units.

was dependent on the TLR9/MyD88 pathway (10,12) (Fig. 2*A*). Cytotoxic T cell infiltrates have been observed in muscle biopsies of patients receiving intramuscular AAV gene therapy (19–21). Thus, we further characterized immune cell infiltration into the local tissue environment. We observed robust CD8+ T cell infiltration in muscle samples from rh32.33.GFP-injected animals with approximately one-third positive for granzyme B, a marker for activated cytotoxic T cells,

while no CD8+ T cell infiltration was observed in any of the eight rh32.33.GFP.io2-injected muscle samples (Fig. 2*B*-*D*). These findings strongly suggest that the presence of io2 prevented capsid-directed CD8+ T cell responses and infiltration.

At a higher dose of 1 x 10^{11} vg, both vectors elicited extremely high capsid-directed T cell responses (~800-1000 spot forming units [SFU]/million splenocytes). While not statistically significant, the engineered vector elicited a modestly weaker T cell capsid response than the unmodified vector, consistent with TLR9i sequences functioning in a vector dose-dependent manner (Fig. 2*A*). Although io2 was only partially protective at the higher dose, rh32.33.GFP.io2 muscle sections exhibited higher GFP expression than those with the unmodified vector by immunohistochemistry (Fig. 2*E*). To facilitate quantification of transgene expression, we tested a similar dose of a single-stranded vector expressing human FIX with a ubiquitous CAG promoter (rh32.33.FIX or rh32.33.FIX.io2) intramuscularly and likewise observed that the engineered vector augmented human FIX levels *in vivo* (Fig. 2*F*). Together, these results indicate that incorporation of io2 into a single-stranded AAV vector reduces CD8+ T cell responses and infiltration and enhances transgene expression following intramuscular AAV delivery.

Plasmacytoid dendritic cells (pDCs) are critical for TLR9/MyD88-dependent early innate immune responses to AAV vectors and subsequently orchestrate anti-capsid CD8+ T cell responses *in vivo* by activating conventional DCs to cross-present capsid antigen (22). To evaluate our approach on human innate immune responses, we tested primary human peripheral blood mononuclear cells (PBMCs) from thirteen healthy donors with single-stranded AAV2 vectors (AAV2.GFP.WPRE and AAV2.GFP.WPRE.io2) *in vitro* (Supplemental Fig. 2). AAV2.GFP.WPRE.io2 elicited lower IL-1β cytokine responses than the unmodified vector in pDCs from nine out of ten donors, and in monocyte-derived dendritic cells (moDCs) from nine out of eleven donors (Fig. 2*G*). Furthermore, AAV2.GFP.WPRE.io2 elicited reduced IFN-β cytokine responses (Fig. 2*H*). These results underscore the value of our approach in evading innate immune responses in human pDCs, suggesting relevance for human patients.

The eye is often described as immune privileged due to the presence of a blood-retina barrier that limits the entry of immune cells and a microenvironment rich in immunosuppressive factors. However, intraocular inflammation and a few instances of persistent loss of visual acuity have been independently reported in clinical trials following subretinal AAV vector administration with dose-dependent severity, in spite of prophylactic immunosuppression (8,9,23). Beyond safety considerations, ocular inflammation may also reduce efficacy directly due to undesirable immune responses in the retina, or indirectly by mandating the use of lower sub-optimal doses. To test if our TLR9-inhibitory strategy could be beneficial for ocular gene therapy, we started with intravitreal administration in mice, a more immunogenic route of administration in the eye compared to subretinal administration, but sparsely studied for immune responses beyond neutralizing antibody formation. Following intravitreal injection of 1×10^{10} vg of AAV2 vectors, *in vivo* retinal imaging with non-invasive optical coherence tomography (OCT) detected local inflammation ~10 dpi, featuring optic disc swelling, retinal vascular changes and cellular infiltration of the vitreous cavity (Fig. 3*A*). This inflammatory response has not been reported before in mice, yet is consistent with the anatomical distribution and phenotype seen in ocular clinical trials (7). We subjected eye tissues to flow cytometry analysis and surprisingly observed CD3+ T cell and CD8+ T cell infiltration, suggesting adaptive T cell responses in the eye. We took advantage of this model to test our strategy and found that while AAV2.GFP.WPRE.io2 did not completely abolish the inflammatory response, it reduced ocular T cell numbers compared to AAV2.GFP.WPRE (Fig. 3*B*). Crucially, incorporation of io2 resulted in earlier and more extensive levels of GFP transgene *in vivo* observable by longitudinal intravital retinal imaging (Fig. 3*C*). Flow cytometry analysis of dissociated retinas confirmed a multi-fold boost in the number of GFP+ retinal cells and further revealed that GFP mean fluorescence intensity was higher on a per cell basis (Fig. 3*D*), implying that evasion of TLR9-mediated immune responses enhanced transduction and/or survival of transduced retinal cells. Together, our results indicate that intravitreal AAV vectors stimulate T cell infiltration in mice, and that incorporation of io2

diminishes local T cell numbers while allowing greater transgene expression by boosting both the number of GFP+ cells and the degree of GFP expression per transduced cell.

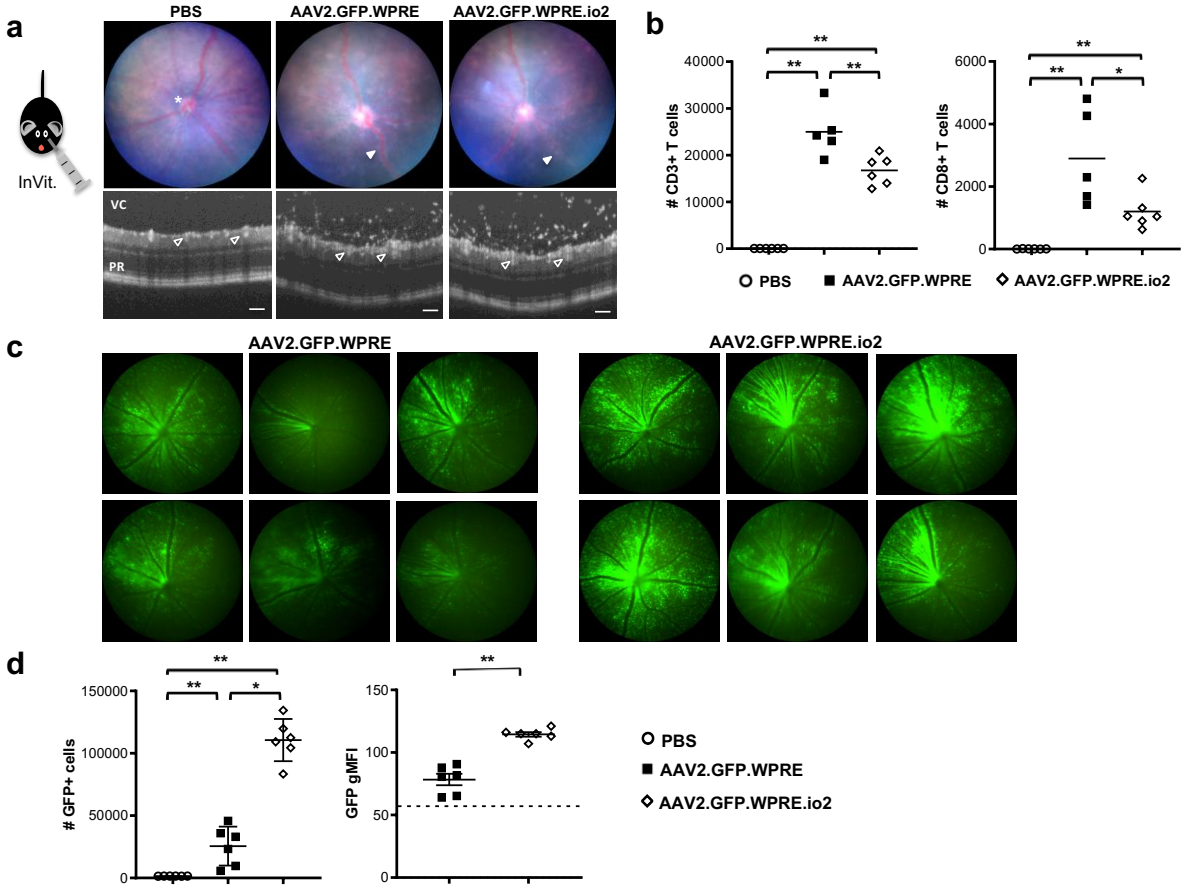

Figure 3. Engineered vector suppresses retinal infiltration and achieves greater GFP transgene levels following intravitreal injection in mice. (**A**) Representative fundal and optical coherence tomography (OCT) scans of the retina 10 days after intravitreal injection with AAV2.GFP.WPRE, AAV2.GFP.WPRE.io2, or PBS control. Scale bar, 100 μm. Image annotations: optic disc (*), vasculitis (solid white arrow), vitreous cavity (VC), retinal vessels (open white arrow), photoreceptor layer (PR). (**B**) Quantification by flow cytometry of CD45+CD3+ and CD45+CD3+CD8+ T cell populations from retinas at 11 dpi. (**C**) Standardized fluorescent *in vivo* retinal images from mice injected with AAV2.GFP.WPRE or AAV2.GFP.WPRE.io2 groups at 10 dpi. (**D**) Quantification of GFP+ cells and geometric mean of GFP fluorescence intensity (gMFI) by flow cytometry in retinas from eyes injected with AAV2.GFP.WPRE, AAV2.GFP.WPRE.io2, or PBS control. Dotted line indicates gMFI from PBS-injected eyes. Data shown as mean ± SD. *n* = 5-6 animals per group. * *P*<0.05, ** *P*<0.005 by two-tailed Mann-Whitney test.

Next, we studied subretinal delivery of the vector, which is a more commonly used route of administration in ocular gene therapy programs. In the mouse eye, subretinal AAV vectors have been regarded as minimally immunogenic; hence we used a pig model, as large animal studies recapitulate intraocular inflammation observed in clinical trials (24,25) and pig and

human eyes share similarities in size and morphology (26). We injected a single-stranded AAV8 vector, AAV8.GFP or AAV8.GFP.io2 and selected an intermediate dose of 4 x 10^{11} vg per eye, based on published reports showing inflammation in patients at 10^{11} to 10^{12} vg per eye (8,9,23). No systemic steroid treatment was used in this study to model a more immunogenic condition.

At 6 weeks post-injection (wpi) in all five AAV-injected outbred pigs, we observed marked loss, shortening, or altered morphology of cone outer segments with AAV.GFP (Fig. 4*A*), suggesting AAV-induced pathology in cone photoreceptors. In contrast, contralateral eyes injected with AAV8.GFP.io2 showed substantially better preservation of cone outer segments and appeared more morphologically similar to uninjected or vehicle-injected eyes, which was verified by quantification of the length of GFP+ cones (Supplemental Fig. 3). We further confirmed these findings by performing cone arrestin staining which labels the entire cone photoreceptor (Supplemental Fig. 3). In addition, we observed in two of five animals (23585 and 23586) substantial loss or retraction with AAV8.GFP of cone pedicles, the synaptic terminals of cones important for signaling visual information (Fig. 4*A* and Supplemental Fig. 3). No such loss was observed in eyes injected with AAV8.GFP.io2.

We analyzed retinal images from *in vivo* OCT b-scans to assess the extent of damage to outer retinal lamination. The vehicle-injected eye (Supplemental Fig. 4) showed a small area of non-severe damage surrounding a similarly sized area of severe damage around the retinotomy site, and the areas of damage were reduced between 2 wpi and 6 wpi. For two AAV-injected animals (23586 and 23587), we observed similar damage between the two eyes at 2 wpi (Supplemental Fig. 4). However, at 6 wpi, the area of severe damage was largely reduced for AAV8.GFP.io2-injected eyes, but not AAV8.GFP-treated eyes. Animal 23585 also experienced severe vitritis at 2 wpi in the AAV8.GFP-treated eye but not the contralateral eye treated with AAV8.GFP.io2 (data not shown). Together, these findings demonstrate that subretinal administration of higher dose AAV vectors can trigger photoreceptor pathology that is significantly reduced with the engineered vector.

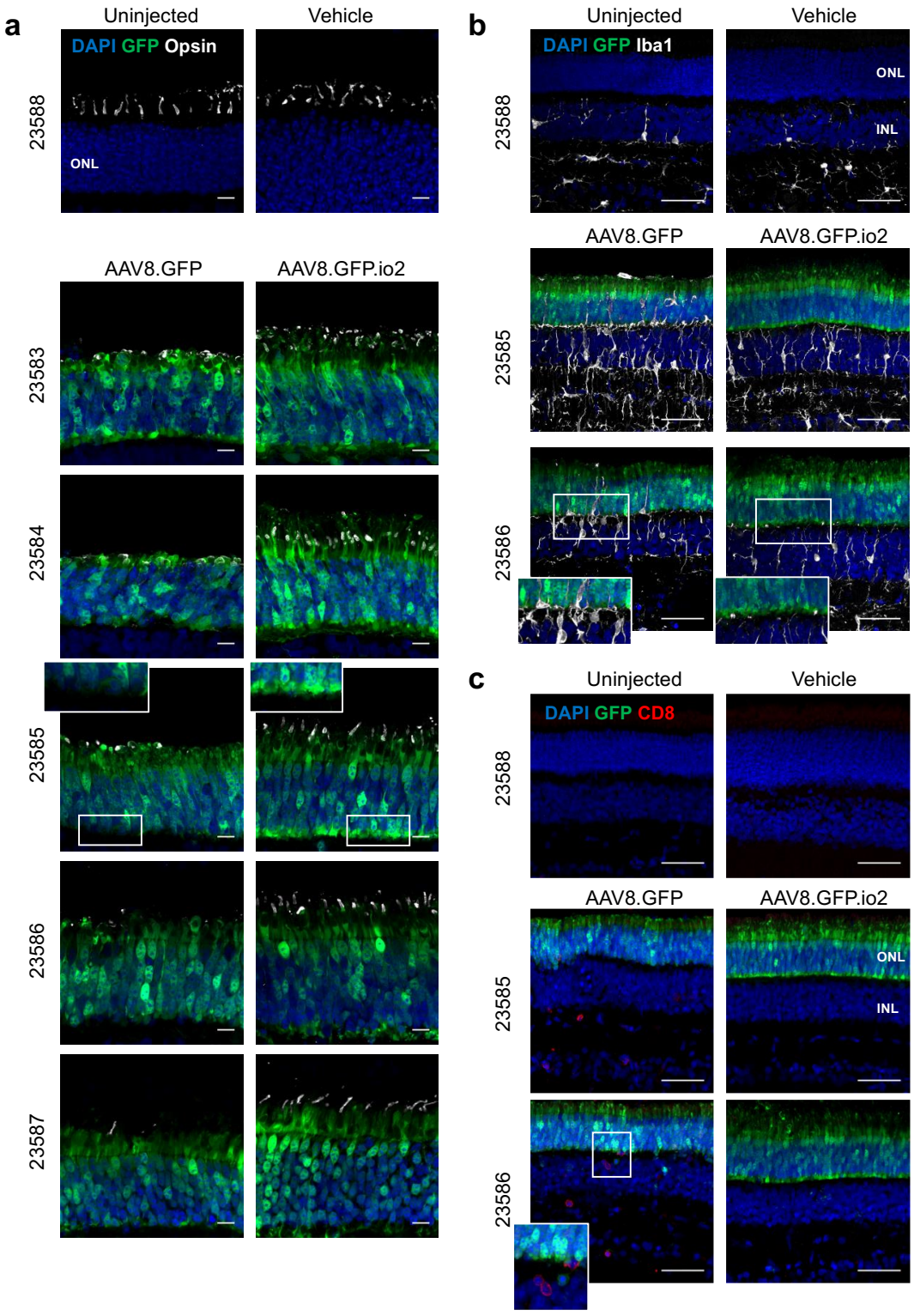

Figure 4. Engineered vector evades photoreceptor pathology and immune responses in subretinal-injected pig eyes. (**A**) Representative images of the outer nuclear layer (ONL) of the retina 6 weeks after subretinal injections. Cone outer segments were visualized with anti-red-green cone opsin. Scale bar, 10 μm. (**B**) Microglial activation and proliferation in the retina visualized with anti-Iba1. Scale bar, 50 μm. (**C**) Cytotoxic T cell infiltration in the retina visualized with anti-CD8. Scale bar, 50 μm. Each animal is indicated by an identification number. Iba1, ionized calcium-binding adaptor protein 1.

We next undertook a detailed analysis of immune responses at the cellular level in the pig retina at 6 wpi. Microglia are the resident innate immune cells of the retina and have been reported to respond to CpG ligands (27). In uninjected and vehicle-injected eyes, staining for microglia with Iba1 showed a ramified pattern outside the outer nuclear layer (ONL) where the photoreceptors reside, consistent with resting microglia (Fig. 4*B*). In contrast, Iba1 signal was significantly increased in all AAV-injected eyes (Fig. 4*B*), suggesting microglial activation and proliferation. Notably, the unmodified vector AAV8.GFP stimulated robust infiltration of microglia into the ONL in animals 23585 and 23586, which was not observed for the engineered vector AAV8.GFP.io2 in the contralateral eyes (Fig. 4*B* and Supplemental Fig. 3). In these same animals, we detected elevated numbers of infiltrating CD8+ T cells in eyes that received AAV8.GFP, but not in contralateral eyes receiving AAV8.GFP.io2 (Fig. 4*B* and Supplemental Fig. 3). We did not observe enhanced GFP expression in photoreceptors of AAV8.GFP.io2-treated eyes compared to AAV8.GFP (Supplemental Fig. 3), though it is possible that a longer in-life study may yield different results. Interestingly, while both AAV8.GFP-treated eyes in animals 23585 and 23586 showed substantial numbers of microglia and T cells in the retina via histology, only the former presented with vitritis during clinical examinations, implying that clinical manifestations of ocular inflammation incompletely capture the extent of inflammation, particularly tissue-localized immune responses in the retina. Taken together, our data suggest that, unlike the unmodified vector, the engineered vector carrying TLR9-inhibitory sequences can avoid eliciting undesirable innate and adaptive immune cell responses in the retina.

Recent successes in AAV gene therapy in the clinic (4,28) highlight the potential for *in vivo* gene therapy to treat multiple genetic disorders. However, as the field moves beyond the most devastating diseases as well as newer applications such as direct vector administration into the CNS and the use of high dose systemic vectors to treat neuromuscular conditions, there is a pressing need to address host immune responses. In this study, we sought to develop AAV vectors that are intrinsically less immunogenic by exploiting the linkage of specific

immunomodulatory non-coding sequences to much longer therapeutic nucleic acids to “cloak” the AAV genome from immune responses. We directly compared AAV vectors with or without TLR9i sequences in experiments encompassing different capsid serotypes, genome configurations, promoters and transgenes, target tissues, routes of administration and animal models, and showed marked reduction of immune responses without changing any other sequences. This “coupled immunomodulation” strategy may offer a versatile, broadly applicable solution for different AAV therapies without impacting capsid or vector genome elements such as promoter choice. Our approach may widen the therapeutic window of gene therapy, enable novel gene therapy applications, and guide the design of future nucleic acid-based therapeutics.

Materials and Methods

Mice. C57BL/6J and *Myd88*$^{-/-}$ mice [B6.129P2(SJL)-Myd88$^{tm1.1Defr}$/J] were purchased from The Jackson Laboratory or Charles River Laboratories and maintained at Harvard Medical School or the University of Bristol. All mouse experimental protocols were approved by the Harvard Medical School Institutional Animal Care and Use Committee and the University of Bristol Animal Welfare and Ethical Review Group.

In vitro testing of DNA oligonucleotides. A HEK293-based reporter cell line stably expressing human TLR9 and an inducible SEAP (secreted embryonic alkaline phosphatase) reporter gene was obtained (HEK-Blue hTLR9, Invivogen). The SEAP gene is under the control of the IFN-β minimal promoter fused to five NF-kB and AP-1 binding sites. Stimulation with a potent TLR9 ligand such as ODN 2006, which contains 4 CpG sites, activates NF-kB and AP-1, inducing the production of SEAP. SEAP activity can subsequently be measured to quantify the amount of NF-kB response, indicating inflammation. All single-stranded DNA oligonucleotides were synthesized with a phosphorothioate backbone for increased stability (IDT). ODN 2006 was directly linked to the indicated sequence with no intervening nucleotides or with an AAAAA linker sequence. ODN Control1 (15 nt) and ODN Control2 (24 nt) were selected to match the

approximate range of lengths of the various TLR9 inhibitory oligonucleotides and were not expected to inhibit or stimulate TLR9. Indicated concentrations of oligonucleotides were incubated with 6 x 10^4 HEK293-TLR9 cells in 200 μl of DMEM growth media per well in 96-well flat bottom plates for 18 hours. 50 μl media was aspirated and incubated with 150 ul HEK-Blue Detection media (Invivogen) for 1-6 hours at 37°C to allow sufficient color change. Absorbance was then read at 630 nm on a Synergy HT microplate reader (BioTek). SEAP activity was similarly measured in HEK293 reporter cell lines (Invivogen) stably expressing the inducible SEAP reporter and either human TLR7 (1 x 10^5 cells) or TLR2 (6 x 10^4 cells). These cells were stimulated, respectively, with 1 μg/ml of Gardiquimod or 100 ng/ml of FSL-1 for 18 hours with or without oligonucleotides. For IL-8 production, supernatant was analyzed using an ELISA kit for human IL-8 (BMS204-3INST, Thermo Fisher).

***Vector production*.** Self-complementary (sc) or single-stranded (ss) AAV vectors were used in this study and all vector genomes were flanked by AAV2 ITRs. scAAV vectors lack the terminal resolution sequence in one ITR and allow earlier and increased transgene expression compared to ssAAV vectors. Unless indicated as self-complementary, all vectors were single-stranded. scAAV.FIX was a kind gift from R. Herzog (Indiana University) and has been described previously (11). AAV.GFP (ss) was obtained from the Harvard DF/HCC DNA Resource Core (clone ID: EvNO00061595). AAV.GFP.WPRE (ss) was a kind gift from L. Vandenberghe (Massachusetts Eye and Ear Infirmary). To distinguish the two single-stranded GFP vectors, we have denoted the former as AAV.GFP and the latter as AAV.GFP.WPRE. ssAAV.FIX vector was constructed by replacing the CMV promoter and GFP in AAV.GFP.WPRE with a CAG promoter and human FIX.

To engineer scAAV.FIX, sequences were inserted into the unique KpnI site found immediately 5' of the TTR promoter. Three copies of ODN TTAGGG (**T**TTAGGGTTAGGGTTAG GGTTAGGG) were inserted, separated by AAAAA linkers (termed "io1" for inflammation-

inhibiting oligonucleotide 1). We used 3 copies of ODN TTAGGG as pilot experiments suggested the use of 3 copies was superior to 1 or 2 copies for blocking innate immune responses (data not shown). A widely used ODN TTAGGG (Invivogen, tlrl-ttag) harbored an additional T (in bold) compared to published studies and thus was included in the sequence. To engineer AAV.GFP, KpnI – [3 copies of ODN TTAGGG with linkers (positive sense)] – [3 copies of INH18 with linkers (negative sense)] – NheI (termed "io2" for inflammation-inhibiting oligonucleotide 2) was inserted immediately 5' of the XbaI site upstream of the right ITR. AAAAA was used as a linker between copies of ODN TTAGGG and INH18. Similarly, to engineer AAV.GFP.WPRE and AAV.FIX, KpnI-io2 was inserted immediately 5' of the XhoI site just upstream of the right ITR. As single-stranded AAV vectors have an equal chance of packaging positive or negative strands of the vector genome, we added both sense and anti-sense TLR9-inhibitory sequences to ensure that all packaged AAV genomes carried copies of TLR9-inhibitory sequences in the right orientation.

AAV vectors were packaged into AAV2, AAV8 and AAVrh32.33 capsids and were purified by the viral vector core facility Gene Transfer Vector Core (GTVC) at Massachusetts Eye and Ear Infirmary/Harvard unless noted otherwise. Briefly, adenoviral helper plasmid, rep2-cap packaging plasmid, and transgene plasmid were transfected at a ratio of 2:1:1 into ~80% confluent HEK293 cells with polyethylenimine in ten-layer HYPERFlasks (Corning). PEI Max (Polysciences)/DNA ratio was maintained at 1.375:1. The supernatant and cells were collected 72 hours after transfection and cell lysates were formed by three sequential freeze-thaw cycles. The viral solution was incubated with 25 U/ml Benzonase (EMD Millipore) at 37°C for 1 hour, and NaCl was added to a final concentration of 650 mM, then the viral solution was kept at 4 ºC for overnight. Cell debris was removed by high speed centrifugation. The collected supernatant was run through Tangential Flow Filtration to concentrate to a volume of 10 mL and then run on an iodixanol gradient. Recovered AAV vectors were washed 3 times with final formulation buffer (FFB: 1x PBS + 35 mM NaCl + 0.001% PF68) using Amicon 100K columns (EMD Millipore) and

concentrated to ~600-1000 μl. Vector titers were determined by digital droplet PCR (ddPCR) using primers directed against the promoter or poly-adenylation signal regions of the transgene cassette. The purity of vector preps was evaluated by running 1 x 10^{10} vg (vector genomes) on an SDS-PAGE gel. Vector preps had <1EU/ml of endotoxin using a limulus amebocyte lysate assay (Genscript). No significant differences in yield (titer x volume) were observed between unmodified and engineered vectors for >20 purifications, suggesting that insertion of the described sequences do not hamper packaging.

AAV2.GFP.WPRE and AAV2.GFP.WPRE.io2 were run on an iodixanol gradient as above and recovered vectors underwent an additional purification step using a heparin column and two washes of 25 ml of PBS plus 0.1 M NaCl as previously described (29). The eluate was then washed with FFB and concentrated as above. The percent of full and empty capsids for AAV8.GFP and AAV8.GFP.io2 was determined by negative stain electron microscopy. Formvar/carbon-coated copper mesh grids (Electron Microscopy Sciences) were glow discharged and loaded with 5 x 10^{10} vg of AAV8.GFP or AAV8.GFP.oligo in PBS for 5 minutes. Grids were washed twice in dH_2O and stained with 0.5% uranyl acetate. After drying, grids were imaged on a FEI Tecnai T12 transmission electron microscope (FEI) equipped with a Gatan UltraScan 895 4k CCD. Ten images for each sample were acquired and particles counted as empty or full based on the intensity of uranyl acetate staining in the center of the capsid.

Mouse liver studies. Adult C57BL/6J or *Myd88*$^{-/-}$ mice were injected intravenously with 100 μl PBS or AAV8 self-complementary viruses (1 x 10^{10} vg or 1 x 10^{11} vg per animal) by tail vein injection as previously described (11). For innate immune responses, the animals were sacrificed 2 hours later. A portion of the right median lobe of the liver was saved in RNAlater solution (Thermo Scientific) and a portion of the left median lobe was fixed in 10% formalin overnight and transferred to 70% ethanol. For RT-PCR, total RNA was extracted from 10-30 mg of mechanically disrupted liver using an RNA extraction kit (OMEGA Bio-Tek). Similar amounts

of RNA were reverse transcribed into cDNA with a high-capacity RNA-to-cDNA kit (Thermo Scientific). cDNA was assayed using TaqMan Fast Advanced Master Mix (Thermo Scientific) and commercially available probes with FAM reporter dye for the indicated target genes (IDT). Expression levels were calculated by normalizing to the housekeeping genes *Actb* or *Gapdh* using the ΔΔCT method and expressed as fold levels compared to saline-injected mice. Reactions were run on a realplex MasterCycler (Eppendorf).

For histology, samples were processed at Beth Israel Deaconess Medical Center (BIDMC) histology core facility. Immunohistochemistry staining was performed on paraffin embedded sections that were cut, deparaffinized and hydrated before use. Antigen retrieval was performed by boiling slides for 10 minutes in 10mM sodium citrate in a pressure cooker. Samples were stained for F4/80+ macrophages (1:50, Abcam) overnight at 4^{o}C and incubated with goat anti-rabbit IgG conjugated with HRP polymer (Abcam) for an hour at room temperature. Slides were developed using DAB (Diaminobenzidine) metal enhanced kit (Vector Lab), counter-stained with hematoxylin (Thermo Fisher) and mounted in Permount mounting media. Slides were observed under the Zeiss Axio Zoom V16 microscope under a 1x/0.25 objective. Five random 25x brightfield images per sample slide were captured with an AxioCam 506 digital camera using Zeiss Zen Pro imaging software.

For hFIX expression, plasma samples were obtained 14 and 28 days after vector delivery. hFIX expression was quantified by analyzing diluted plasma samples using an ELISA kit specific for human factor IX (Abcam). The kit had a sensitivity of at least 0.78 ng/ml. *In vitro* neutralizing antibody (NAb) assays were performed on plasma samples 28 days after PBS or 1 x 10^{11} vg AAV8 administration as previously described (30).

Mouse muscle studies. Adult C57BL/6J or *Myd88*$^{-/-}$ mice were injected intramuscularly with 50 μl PBS or AAVrh32.33 single-stranded viruses (1 x 10^{10} or 1 x 10^{11} vg per animal) encoding GFP or hFIX in the left quadriceps muscle. Animals were sacrificed 21 days later and a portion of the quadriceps was fixed in 10% formalin overnight and transferred to 70% ethanol.

For histology, muscle samples were processed at Dana-Farber/Harvard Cancer Center Specialized Histopathology Services (SHS) and BIDMC histology core facilities, embedded in paraffin, and stained for CD8 (1:500, CST) and granzyme B (1:500, R&D). Muscle sections were also stained for GFP (1:800, Abcam). For rh32.33.FIX injected mice, plasma samples were obtained 14, 28, 42 and 60 days after 1 x 10^{11} vg vector administration with hFIX expression was measured by ELISA as described above.

For IFN-gamma T cell ELISpot assays, spleens were harvested at 21 days post-injection, dissociated, passed through a 70 μm cell strainer, and spun down. The cell pellet was treated with 1 mL of ACK lysing buffer (Life Technologies) to lyse red blood cells. To determine the number of cells secreting IFN-gamma in response to antigenic stimulation, an IFN-gamma ELISpot assay was used (R&D Systems). Briefly, 96-well plates were pre-blocked with RPMI growth media for 2 hours at room temperature and rinsed twice with PBS. 5 x 10^5 splenocytes were seeded per well in T cell medium for 18 hours with 2 μg/mL of a CD8+ h2-k^b restricted dominant epitope of AAVrh32.33 capsid (Genemed Synthesis) or PMA/ionomycin as a non-specific positive control, followed by staining. ELISpot plates were evaluated in blinded fashion (ZellNet Consulting, Inc.) with an automated ELISpot reader system (KS ELISpot reader, Zeiss).

Human PBMCs studies. Cryopreserved peripheral blood mononuclear cells (PBMCs) from de-identified healthy donors were purchased from Cellular Technology Limited. Briefly, PBMCs were thawed for 5 minutes at 37°C, and the content of each cryovial was transferred to a 15 mL Falcon tube. Tubes were filled with 10 mL AIM-V Glutamax medium (Gibco) containing benzonase (Millipore Sigma). Cells were washed and resuspended at a final concentration of 10^7 cells/mL in AIM-V medium with plasmocin (InvivoGen). For dendritic cell (DC) stimulation, PBMCs were seeded at 5 × 10^6 cells per well in a 24-well plate with AAV2.GFP.WPRE or AAV2.GFP.WPRE.io2 at 3 × 10^{10} vg/well. LPS (InvivoGen) was used as positive control at 5 μg/ml. PBMCs from 13 donors were used and cells were incubated for 24 hours prior to harvest

and staining. Before staining, cytokine secretion was blocked for 5 hours with a mix of Brefeldin A and Monensin (BD Biosciences). Wells were then washed with AIM-V medium to remove non-adherent cells. A cell scraper was used to recover the activated, adherent DCs, which were treated with FcR binding inhibitor (Thermo Fisher). DC-surface staining was performed with anti-human CD3 (Beckman Coulter), CD19 (Beckman Coulter), CD14 (BD Horizon), CD11c (Thermo-Fisher) and HLA-DR (BD Biosciences). Dead cells were stained with Zombie Yellow Fixable Viability kit (BioLegend). Fixation and permeabilization of cells were performed with Cytofix/Cyto-perm (BD Biosciences). DCs were intracellularly stained with antibodies against human IL-1β (511710, BioLegend) and IL-6 (17-7069, Thermo Fisher). Fluorescence was measured on a Cytoflex S flow cytometer (Beckman Coulter), and results analyzed with the FlowJo software (Tree Star). Intracellular IFN- β staining of PBMCs from 7 donors was performed as above with an anti-human IFN-β antibody (MBS531514, MyBiosource).

Mouse eye studies. Adult mice were anesthetized by intraperitoneal injection of ketamine/xylazine and pupils dilated with a drop of 1% tropicamide. 2 µL of AAV vector at 5 x 10^{12} vg/mL was then delivered intravitreally via the pars plana using a 33-gauge needle on a microsyringe under direct visualization (Hamilton Company). The contralateral eye of each animal received a control injection of PBS. Immediately following injection, 1% chloramphenicol ointment (Martindale Pharma) was topically applied, and the animals warmed on a heating pad for recovery. Laterality of injected eyes was randomized with investigators blinded to the vector type throughout intervention and analysis. On selected days post-injection, mice were anesthetized with 2% isofluorane and pupils dilated for clinical assessment. A Micron IV retinal imaging microscope (Phoenix Research Laboratories) was used to capture OCT scans and color and fluorescence fundal images.

For flow cytometry**,** eyes were dissected as described in Chapter 2 to isolate mouse retinas. Tissues were then mechanically dissociated before straining cells through a 60 µm filter and centrifuging at 1200 rpm for 5 minutes. The cell pellet was resuspended in FACS buffer and

incubated with rat anti-mouse CD16/32 Fc block (1:50, BD Biosciences) for 10 minutes at 4°C before incubation with fluorochrome-conjugated antibodies against CD45 (1:1500, BD Biosciences), CD3 (1:40, BioLegend), CD4 (1:100, BD Biosciences), and CD8 (1:200, BioLegend) at 4°C for 20 minutes. Cells were washed and resuspended in 7-aminoactinomycin D (7AAD, Thermo Fisher) for dead cell exclusion. Cell suspensions were acquired using a 4-laser Fortessa X20 flow cytometer (BD Cytometry Systems) and analyzed using FlowJo software (Tree Star).

Pig eye studies. Surgeries were performed at the University of Louisville with approval from the University of Louisville Institutional Animal Care and Use Committee. Six 50-day-old wild-type domestic female pigs were purchased (Oak Hill Genetics). After a one-week acclimatization period, surgery to subretinally inject AAV vectors was performed. Animals were sedated with intravenous ketamine (10 mg/kg) and dexmedetomidine (0.04 mg/kg) and treated with atropine (0.25 mg/kg). An endotracheal tube was inserted, and 1-3% of isoflurane was administered to achieve a surgical plane of anesthesia. An IV line inserted in the ear vein delivered 10-15 mL/kg/h Lactated Ringers Solution with or without 5% dextrose to maintain blood pressure and normal glycemic levels. Body temperature was monitored with a rectal thermometer and maintained via a heated procedure table. Heart and respiration rates and oxygen saturation were recorded throughout the procedures and anesthesia adjusted to maintain a physiological range. A vitreoretinal approach was used to access the subretinal space. A lateral canthotomy was performed to increase exposure in the surgical field. After insertion of an eyelid speculum, two 25-gauge trocars were placed at 1.5 mm posterior to the limbus; one in superior-nasal and the other in inferior-nasal quadrant. An anterior chamber fluid paracentesis was performed to make space for the injected volume. A light pipe was inserted into one trochar to help visualize the retina. A 41-gauge subretinal cannula needle was placed through the other trochar and used to make a local retinal detachment (bleb), which included injection of inoculum (~75 μl). The inoculum contained either AAV8.GFP.io2 or AAV8.GFP in

final formulation buffer (FFB) or FFB alone (vehicle). We injected either AAV8.GFP.io2 or AAV8.GFP into OD or OS of two pigs in each of three surgery sessions (total of 10 AAV-treated eyed, 1 FFB-injected eye and 1 uninjected control eye). After the injection, the light pipe, needle and the trochars were removed. The lateral canthotomy was sutured closed with 4-0 nylon and antibiotic and steroid ointment topically administered.

A complete clinical examination of the eye was performed at weekly intervals in anesthetized pigs from 2 to 6 weeks post-injection (wpi). This included a slit lamp examination to inspect the anterior segment of the eye, indirect ophthalmoscopy to inspect the fundus, and fundus photography to document the state of the retina. In addition, each eye was scored for inflammation using the SUN classification (31). The surgeon performing injections was blinded to the test article, and similarly, clinical examinations were performed blinded. Prior to surgery and at 2 and 6 wpi, OCT (Bioptigen/Leica Biosciences) was performed to image the retinal layers *in vivo*. Pupils were dilated and accommodation relaxed with topical 2.5% phenylephrine hydrochloride and 1% tropicamide. Lid specula held the eyelids open and corneas were wet throughout imaging with artificial tears (OcuSoft). Using OCT b-scans, we identified the retinotomy site and characterized the lamination pattern of hypo- and hyper-reflective bands as a function of distance from that area in both the axial and lateral dimensions. We defined two types of damage: severe damage represented areas where hyper-reflective bands representing the retinal pigment epithelium and photoreceptor inner/outer segments were disrupted. Non-severe damage were areas where at least one of these hyper-reflective bands was present, but one or both were thinner and less well-defined than areas without damage. The shape, location and size of these two types of damage were measured. These areas were then superimposed on the fundus image and the areas of damage compared to GFP expression.

At 6 wpi, pigs were sacrificed with a 1 mL/5 kg solution of Beuthanasia (390 mg pentobarbital sodium, 50 mg phenytoin sodium/ml) and eyes enucleated. The cornea and lens were removed, and the eyecup was dissected and fixed in 4% paraformaldehyde in PBS for 1

hour at room temperature. Wholemount retinas were examined using a fluorescent microscope (Olympus MVX10) and the region of GFP+ expression located. The retina was dissected such that the piece used for histology included all of the GFP+ region, as well as flanking GFP- regions. Pig retinal tissue was cryoprotected in graded sucrose solutions up to 30% sucrose in PBS, then embedded in a 1:1 mixture of 30% sucrose and optimal cutting temperature (Tissue-Tek) followed by cryosectioning on a Leica CM3050S (Leica Microsystems). Transverse sections of retinal tissue were cut at 20 μm. For immunohistochemistry, tissue sections were blocked with 5% donkey or goat serum in PBS with 0.1% Triton X-100 for 1 hour at room temperature and stained overnight at 4 °C in blocking solution with primary antibodies against red-green opsin (1:600, EMD Millipore), human cone arrestin (1:10000, a gift from C. Craft, University of Southern California), Iba1 (1:200, Abcam) and CD8 (1:200, Bio-Rad). Sections were then stained with 1:1000 of the appropriate secondary antibody (Jackson ImmunoResearch) for 2 hours at room temperature followed by 4',6-diamidino-2-phenylindole (DAPI) for 5 minutes. Mounted slides were examined using a LSM710 laser scanning confocal microscope (Zeiss) with a 40x oil-immersion objective. For sections from AAV-injected eyes, care was taken to acquire representative images of GFP+ regions near, but not directly at, the retinotomy scar. Similar laser settings were used when acquiring images of the two eyes of each animal. To quantify the morphology of infected photoreceptors, we measured the inner segment plus outer segment (IS+OS) length of GFP+ cones, defined as the distance from the apex of the cone outer segment to the proximal edge of the nucleus. For each eye, the mean IS+OS length was calculated from a minimum of 30 GFP+ cones over at least three different 20 μm sections. The number of Iba1+ processes extending into the ONL and CD8+ cells infiltrating the retina were also quantified as described.

Statistics. Two-tailed Student's t-tests were used for testing oligonucleotides in HEK293-TLR9 reporter cells *in vitro*. A two-tailed Mann-Whitney test, two-way ANOVA with

Sidak's post-hoc test, or two-tailed Student's t-test was used for *in vivo* studies, as indicated. A two-tailed Wilcoxon matched pairs signed ranked test was used for human PBMC IL-1β/IL-6 experiments and a two-tailed Student's t-test for IFN-β experiments. A *P* value of <0.05 was considered statistically significant. No pre-specified effect size was assumed. Three to ten replicates or animals or donors for each condition were used.

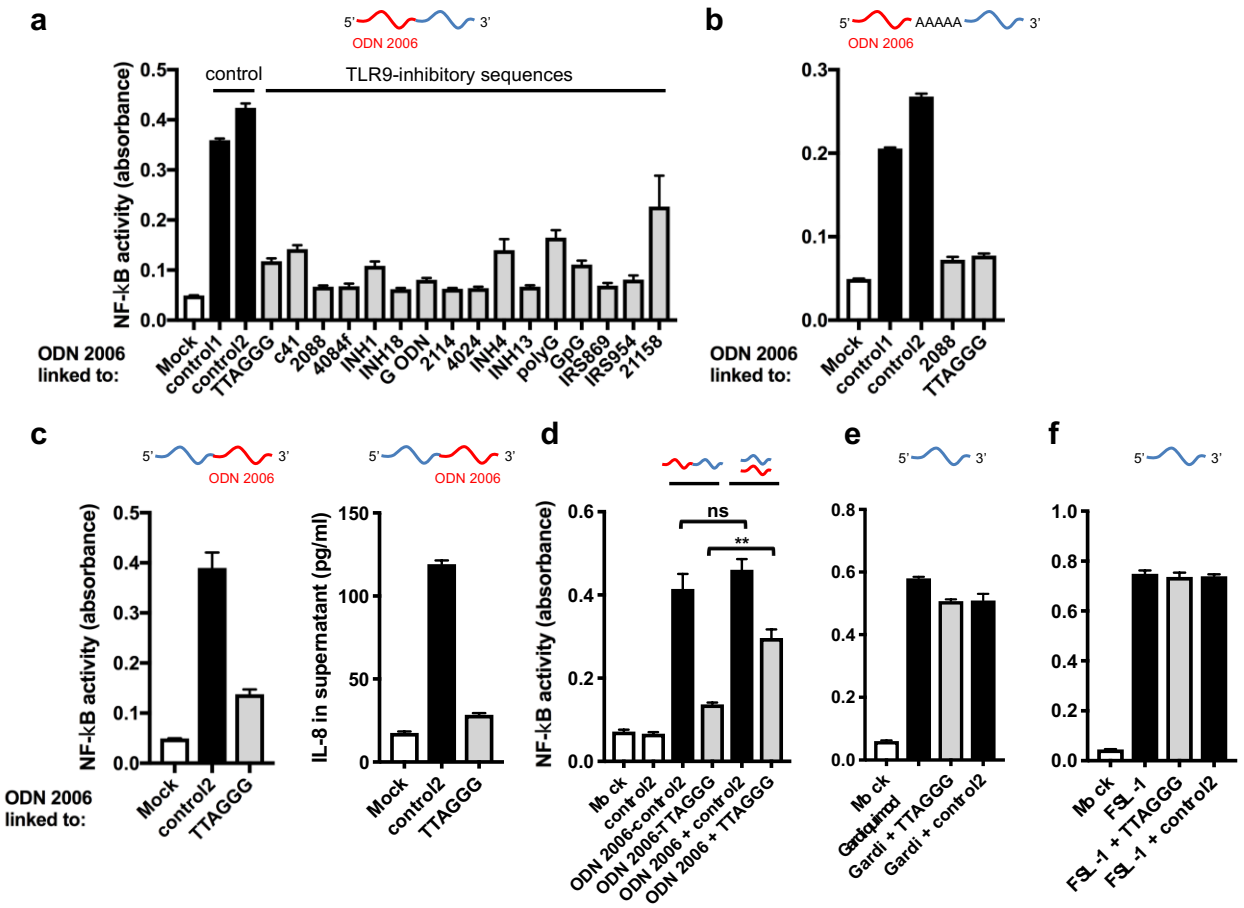

Supplemental Figure. 1. NF-kB response to single-stranded DNA oligonucleotides in reporter cells *in vitro*. (**A-C**) NF-kB response (A-C) or IL-8 response (C) by HEK293-TLR9 reporter cells after treatment with indicated oligonucleotides at 0.5 μM. (**D**) NF-kB response by HEK293-TLR9 reporter cells after treatment with 0.02 μM of linked oligonucleotides or unlinked oligonucleotides. (**E, F**) NF-kB response by HEK293-TLR7 (E) or HEK293-TLR2 (F) reporter cells after treatment with Gardiquimod (E) or FSL-1 (F) with or without oligonucleotides at 5 μM. *n* = 3 biological replicates for all experiments. Data shown as mean ± SD. ** *P*<0.005 by two-tailed Student's t-test. ns, not significant.

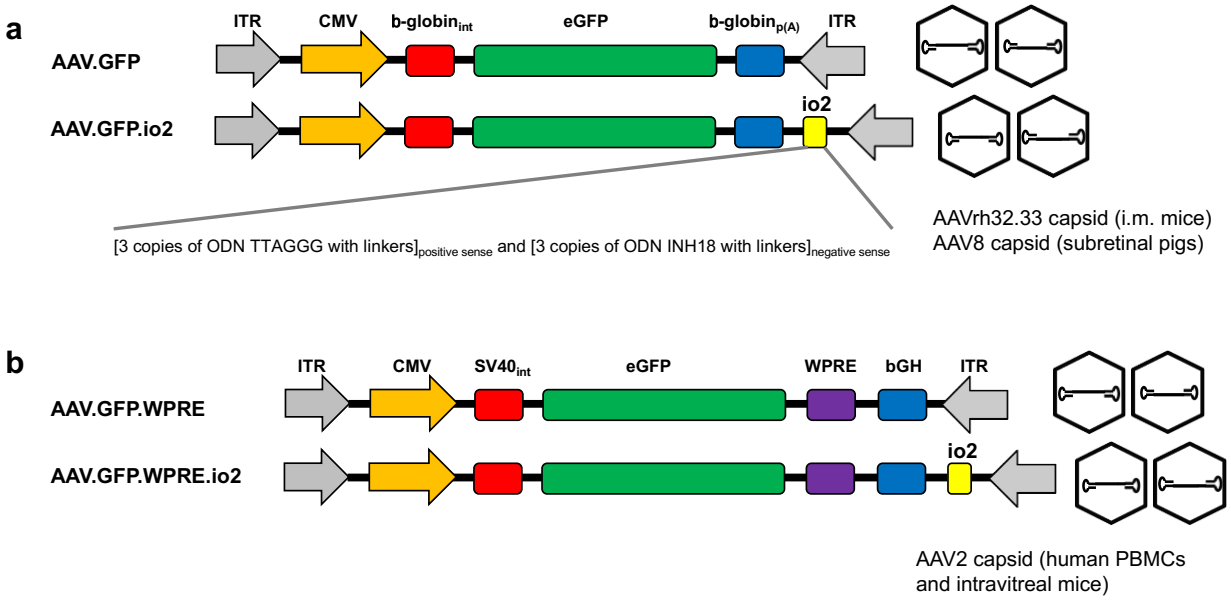

Supplemental Figure 2. Engineered single-stranded vectors. (**A**) Schematics of AAV.GFP (unmodified vector) and AAV.GFP.io2 (engineered vector). Vectors were packaged in rh32.33 capsid for intramuscular injections in mice *in vivo*, and in AAV8 for subretinal injections in pigs *in vivo*. (**B**) Schematics of AAV.GFP.WPRE (unmodified vector) and AAV.GFP.WPRE.io2 (engineered vector). Vectors were packaged in AAV2 capsid for human PBMCs *in vitro* and intravitreal injections in mice *in vivo.* In both (A) and (B), the io2 sequence is not expected to be transcribed or translated due to its placement in an untranslated region of the vector downstream of the poly(A) signal. As single-stranded AAV vectors have an equal chance of packaging positive or negative strands of the viral genome, io2 is designed to include both sense and anti-sense TLR9-inhibitory sequences, ensuring that all packaged AAV genomes carry copies of TLR9-inhibitory sequences in the right orientation. ITR, inverted terminal repeat; CMV, cytomegalovirus promoter; b-globin$_{int}$, beta-globin intron; b-globin$_{p(A)}$, beta-globin poly(A) signal SV40$_{int}$, SV40 intron; WPRE, Woodchuck Hepatitis Virus Posttranscriptional Regulatory Element; bGH, bovine growth hormone poly(A) signal.

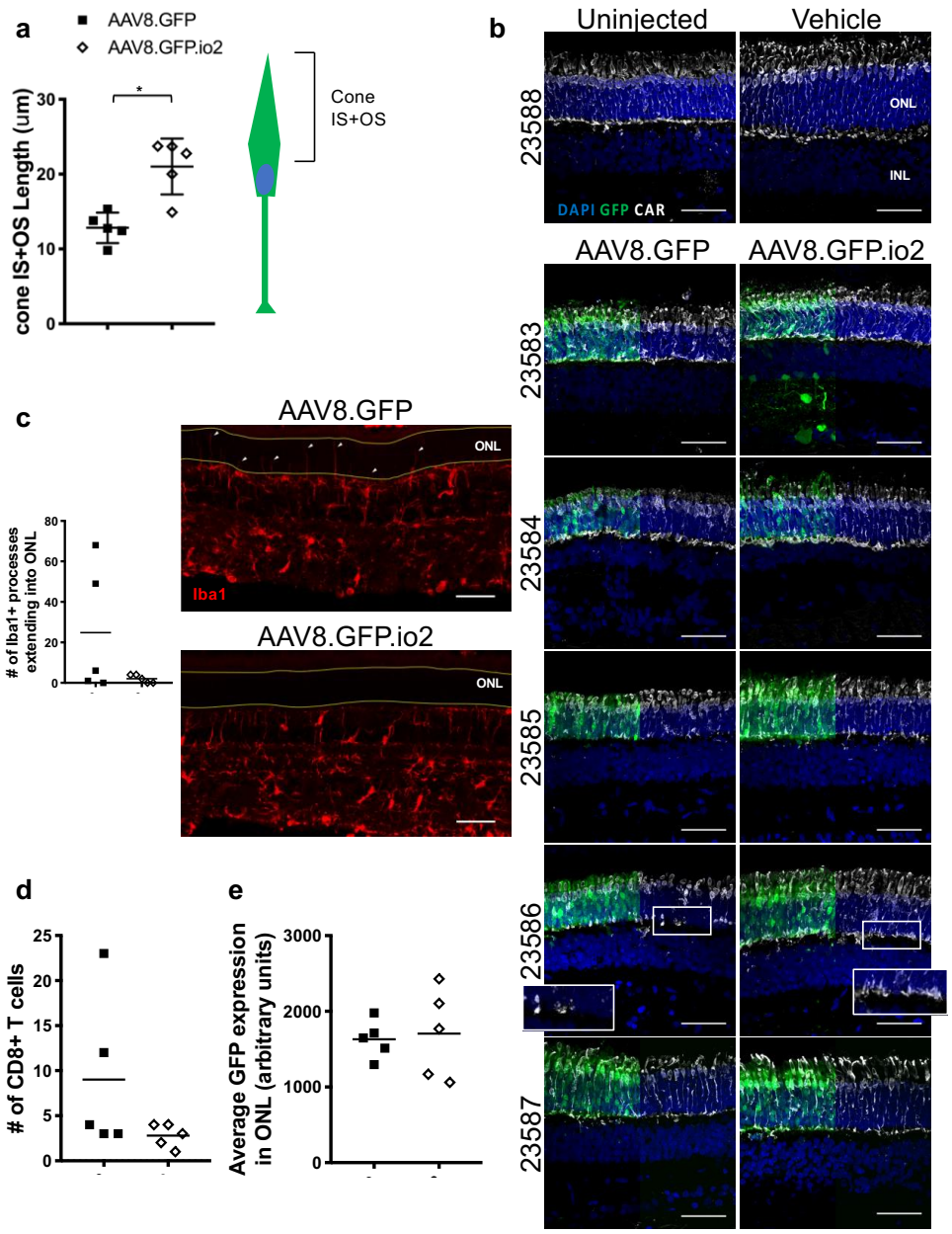

Supplemental Figure 3. Engineered vector evades photoreceptor pathology in subretinal-injected pig eyes. (**A**) Quantification of inner segment plus outer segment (IS+OS) length of GFP+ cones, defined as the distance from the apex of the cone outer segment to the proximal edge of the nucleus. For each eye, mean IS+OS length was calculated from a minimum of 30 GFP+ cones over at least three different 20 μm sections. * *P*<0.05 by two-tailed Mann-Whitney test. (**B**) Representative images of retinas 6 weeks after subretinal injections. Cone photoreceptors were visualized with anti-human cone arrestin. Scale bar, 50 μm. GFP signal from the right half of each image was digitally removed to allow better visualization of arrestin staining. (**C**) Quantification of Iba1+ processes extending into the ONL. For each eye, images of three GFP+ fields of view (20x) from separate 20 μm sections were acquired and the number of Iba1+ processes counted. Example Iba1+ processes (white arrows) in the ONL (yellow lines) from animal 23586 are shown. Scale bar, 50 μm. (**D**) Quantification of CD8+ cells in retinas. For each eye, CD8+ cells were counted in ten separate GFP+ fields of view (20x) from at least three separate 20 μm sections. (**E**) Quantification of GFP expression in the ONL. For each eye, two GFP+ sections were imaged and intensity values obtained and averaged from the field of view (20x) with the highest GFP signal in each section. ONL, outer nuclear layer; CAR, cone arrestin; Iba1, ionized calcium-binding adaptor protein 1.

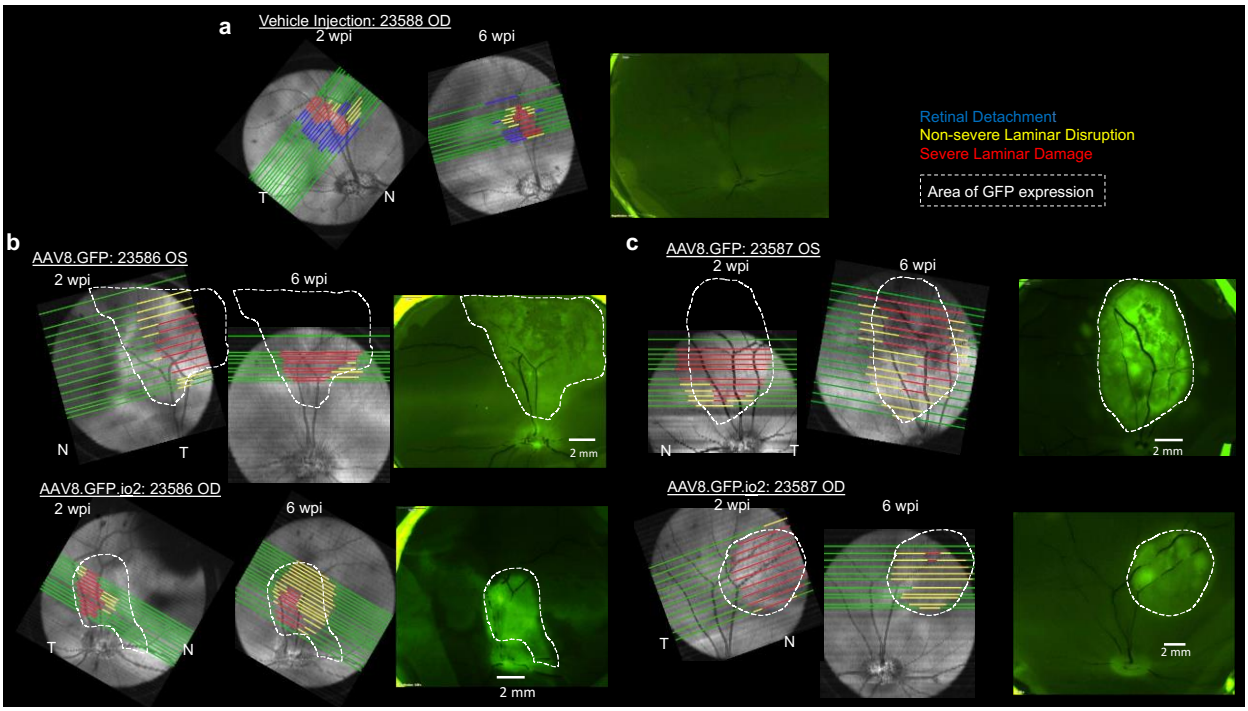

Supplemental Figure 4. Engineered vector ameliorates outer retina laminar pathology in subretinal-injected pig eyes. (**A-C**) Extent of each type of damage determined by optical coherence tomography (OCT) superimposed on fundus images for eyes injected subretinally with vehicle (A), AAV8.GFP (B, C, top), or AAV8.GFP.io2 (B, C, bottom). Areas were defined as severe damage (red), non-severe damage (yellow), normal (green), or retinal detachment (blue). Severe damage always surrounded the retinotomy and was defined as loss of the hyper-reflective outer retinal bands that represent the retinal pigment epithelium and photoreceptor inner/outer segments. Non-severe damage (yellow) was usually found surrounding areas of severe damage and was defined as areas where the outer retinal hyper-reflective bands were thinner and/or more poorly defined. Dashed white lines denote the GFP+ regions as determined by fluorescence images of each eye cup. In eyes injected with AAV8.GFP.io2, the area of severe damage decreased up to 84% between 2 and 6 wpi. In contrast, in eyes injected with AAV8.GFP, the area with severe damage remained approximately constant. A meaningful statistical analysis could not be performed with the small number of eyes in the study.

References

1. Verma IM, Somia N. Gene therapy - Promises, problems and prospects. Vol. 389, Nature. 1997. p. 239–42.
2. Hinderer C, Katz N, Buza EL, Dyer C, Goode T, Bell P, et al. Severe toxicity in nonhuman primates and piglets following high-dose intravenous administration of an AAV vector expressing human SMN. Hum Gene Ther. 2018;29(3):hum.2018.015.
3. Hordeaux J, Wang Q, Katz N, Buza EL, Bell P, Wilson JM. The Neurotropic Properties of AAV-PHP.B Are Limited to C57BL/6J Mice. Mol Ther. 2018;26(3):664–8.
4. Mendell JR, Al-Zaidy S, Shell R, Arnold WD, Rodino-Klapac LR, Prior TW, et al. Single-Dose Gene-Replacement Therapy for Spinal Muscular Atrophy. N Engl J Med. 2017 Nov 2;377(18):1713–22.
5. Manno CS, Arruda VR, Pierce GF, Glader B, Ragni M, Rasko J, et al. Successful transduction of liver in hemophilia by AAV-Factor IX and limitations imposed by the host immune response. Nat Med. 2006 Mar;12(3):342–7.
6. Nathwani AC, Tuddenham EGD, Rangarajan S, Rosales C, McIntosh J, Linch DC, et al. Adenovirus-associated virus vector-mediated gene transfer in hemophilia B. N Engl J Med. 2011 Dec 22;365(25):2357–65.
7. Cukras C, Wiley HE, Jeffrey BG, Sen HN, Turriff A, Zeng Y, et al. Retinal AAV8-RS1 Gene Therapy for X-Linked Retinoschisis: Initial Findings from a Phase I/IIa Trial by Intravitreal Delivery. Mol Ther. 2018 Sep 5;26(9):2282–94.
8. Bainbridge JWB, Mehat MS, Sundaram V, Robbie SJ, Barker SE, Ripamonti C, et al. Long-Term Effect of Gene Therapy on Leber's Congenital Amaurosis. N Engl J Med. 2015;372(20):1887–97.
9. Dimopoulos IS, Hoang SC, Radziwon A, Binczyk NM, Seabra MC, MacLaren RE, et al. Two-Year Results after AAV2-Mediated Gene Therapy for Choroideremia: The Alberta Experience. Am J Ophthalmol. 2018;193:130–42.
10. Zhu J, Huang X, Yang Y. The TLR9-MyD88 pathway is critical for adaptive immune responses to adeno- associated virus gene therapy vectors in mice. J Clin Invest. 2016;119(8):2388–98.
11. Martino AT, Suzuki M, Markusic DM, Zolotukhin I, Ryals RC, Ertl HCJ, et al. The genome of self-complementary adeno-associated viral vectors increases Toll-like receptor 9 – dependent innate immune responses in the liver. Blood. 2011;117(24):6459–68.
12. Faust SM, Bell P, Cutler BJ, Ashley SN, Zhu Y, Rabinowitz JE, et al. CpG-depleted adeno-associated virus vectors evade immune detection. J Clin Invest. 2013;123(7):2994–3001.
13. Beutler BA. TLRs and innate immunity. Vol. 113, Blood. 2009. p. 1399–407.
14. Hösel M, Broxtermann M, Janicki H, Esser K, Arzberger S, Hartmann P, et al. Toll-like receptor 2-mediated innate immune response in human nonparenchymal liver cells toward adeno-associated viral vectors. Hepatology. 2012;55(1):287–97.
15. Ohto U, Shibata T, Tanji H, Ishida H, Krayukhina E, Uchiyama S, et al. Structural basis of CpG and inhibitory DNA recognition by Toll-like receptor 9. Nature. 2015 Apr 30;520(7549):702–5.
16. Hartmann G, Krieg AM. Mechanism and function of a newly identified CpG DNA motif in human primary B cells. J Immunol. 2000 Jan 15;164(2):944–53.
17. Gursel I, Gursel M, Yamada H, Ishii KJ, Takeshita F, Klinman DM. Repetitive elements in mammalian telomeres suppress bacterial DNA-induced immune activation. J Immunol.

2003 Aug 1;171(3):1393–400.

18. Mays LE, Vandenberghe LH, Xiao R, Bell P, Nam H-J, Agbandje-McKenna M, et al. Adeno-associated virus capsid structure drives CD4-dependent CD8+ T cell response to vector encoded proteins. J Immunol. 2009 May 15;182(10):6051–60.
19. Flotte TR, Trapnell BC, Humphries M, Carey B, Calcedo R, Rouhani F, et al. Phase 2 clinical trial of a recombinant adeno-associated viral vector expressing α 1-antitrypsin: Interim results. Hum Gene Ther. 2011 Oct 1;22(10):1239–47.
20. Mingozzi F, Meulenberg JJ, Hui DJ, Basner-Tschakarjan E, Hasbrouck NC, Edmonson SA, et al. AAV-1-mediated gene transfer to skeletal muscle in humans results in dose-dependent activation of capsid-specific T cells. Blood. 2009;114(10):2077–86.
21. Ferreira V, Petry H, Salmon F. Immune responses to AAV-vectors, The Glybera example from bench to bedside. Front Immunol. 2014;5(MAR).
22. Rogers GL, Shirley JL, Zolotukhin I, Kumar SRP, Sherman A, Perrin GQ, et al. Plasmacytoid and conventional dendr1. Blood. 2017;129(24):3184–95.
23. Xue K, Jolly JK, Barnard AR, Rudenko A, Salvetti AP, Patrício MI, et al. Beneficial effects on vision in patients undergoing retinal gene therapy for choroideremia. Vol. 24, Nature Medicine. Nature Publishing Group; 2018. p. 1507–12.
24. Ramachandran PS, Lee V, Wei Z, Song JY, Casal G, Cronin T, et al. Evaluation of Dose and Safety of AAV7m8 and AAV8BP2 in the Non-Human Primate Retina. Vol. 28, Human Gene Therapy. 2017. 154–167 p.
25. Reichel FF, Dauletbekov DL, Klein R, Peters T, Ochakovski GA, Seitz IP, et al. AAV8 Can Induce Innate and Adaptive Immune Response in the Primate Eye. Mol Ther. 2017 Dec 6;25(12):2648–60.
26. Sanchez I, Martin R, Ussa F, Fernandez-Bueno I. The parameters of the porcine eyeball. Graefes Arch Clin Exp Ophthalmol. 2011 Apr;249(4):475–82.
27. Olson JK, Miller SD. Microglia Initiate Central Nervous System Innate and Adaptive Immune Responses through Multiple TLRs. J Immunol. 2004 Sep 15;173(6):3916–24.
28. Russell S, Bennett J, Wellman JA, Chung DC, Yu Z-F, Tillman A, et al. Efficacy and safety of voretigene neparvovec (AAV2-hRPE65v2) in patients with RPE65 -mediated inherited retinal dystrophy: a randomised, controlled, open-label, phase 3 trial. Lancet. 2017 Aug 26;390(10097):849–60.
29. Auricchio A, Hildinger M, O'Connor E, Gao GP, Wilson JM. Isolation of highly infectious and pure adeno-associated virus type 2 vectors with a single-step gravity-flow column. Hum Gene Ther. 2001 Jan 1;12(1):71–6.
30. Calcedo R, Vandenberghe LH, Gao G, Lin J, Wilson JM. Worldwide epidemiology of neutralizing antibodies to adeno-associated viruses. J Infect Dis. 2009 Feb 1;199(3):381–90.
31. Jabs DA, Nussenblatt RB, Rosenbaum JT, Atmaca LS, Becker MD, Brezin AP, et al. Standardization of uveitis nomenclature for reporting clinical data. Results of the first international workshop. Am J Ophthalmol. 2005 Sep 1;140(3):509–16.

Chapter 6: *In situ* detection of AAV genomes with DNA SABER-FISH

Abstract

Gene therapy with recombinant adeno-associated viral (AAV) vectors is a promising modality for the treatment of genetic disorders with multiple recent successes in human patients. Despite these advances, a number of therapeutically relevant concepts regarding AAV vectors remain incompletely understood, due in part to the lack of readily adoptable methods to track vector particles or genomes. Here, we describe a novel application of DNA signal amplification by exchange reaction fluorescence *in situ* hybridization (SABER-FISH) that enables the visualization and quantification of individual AAV genomes. Using highly sensitive SABER-FISH probes, we found that AAV genomes could be detected within retinal cells as early as 3 hours after subretinal delivery of AAV vectors in mice. We subsequently quantified these AAV genomes in rod photoreceptors, cone photoreceptors, and the retinal pigment epithelium (RPE) and observed a direct correlation between the number of genomes in a cell and its level of vector-mediated transgene expression. Our findings show that SABER-FISH can be used to visualize AAV genomes *in situ*, allowing for the identification and tracking of vector-transduced cells in tissues receiving AAV gene therapy.

Contributions

Sean K. Wang[1], Sylvain W. Lapan[1], Christin M. Hong[1], Constance L. Cepko[1,2]

[1] Departments of Genetics and Ophthalmology, Harvard Medical School, Boston, MA 02115, USA

[2] Howard Hughes Medical Institute, Chevy Chase, MD 20815, USA

S.K.W., S.W.L., and C.L.C. conceived the study; S.K.W., S.W.L., and C.L.C. designed research; S.K.W. and C.M.H. performed experiments and analyzed data; S.K.W. and C.L.C. wrote the paper.

Note: This work has not been submitted for publication and is currently in preparation.

Introduction

First described more than 35 years ago, recombinant adeno-associated viral (AAV) vectors derived from non-enveloped and replication-defective adeno-associated viruses have become the vector of choice for gene therapy due to their long-term expression of transgenes and relative lack of pathogenicity (1–4). AAV vectors consist of a small (~25 nm) protein capsid surrounding either a positive- or negative-sense single-stranded DNA (ssDNA) genome, which are packaged with equal frequency and can accommodate up to 4.7 kb of exogenous DNA (3,5,6). At the 5' and 3' ends of the vector genome lie palindromic sequences called inverted terminal repeats (ITRs), which form hairpin structures and initiate synthesis of the complementary second strand through a self-priming mechanism (7,8). Although capable of integration into the host genome (9), AAV vectors in infected cells are thought to predominantly exist as extrachromosomal episomes in the nucleus (10). These episomes are diluted and subsequently lost in actively dividing cells, but can be effectively maintained in post-mitotic cell types such as those of the brain, retina, muscle, and heart.

In recent years, use of AAV vectors in human patients has grown tremendously, highlighted by the advent of gene therapy treatments for Leber's congenital amaurosis and spinal muscular atrophy (11,12). The translational potential of AAV vectors has now led to over 200 phase I, II, and III clinical trials (clinicaltrials.gov). Despite these advances, a number of therapeutically relevant concepts regarding AAV vectors remain incompletely understood, due in part to the lack of readily adoptable methods to visualize vector particles or genomes. For instance, it is still unknown in most cell types whether one or multiple transduction events are required for AAV transgenes to be expressed. Likewise, for vectors without a reporter gene such as those administered in patients, it is often challenging to determine the identities of infected cells and distinguish them from uninfected cells in the same region. One strategy for tracking AAV vectors in animal models has been to tag capsid proteins with radioactive or fluorescent labels (13–15). While this approach allows for the detection of vectors shortly after

delivery, it can only provide information prior to viral uncoating and be applied to tissue samples that receive the specially labeled capsids. To address the concerns above, an alternative option could be to visualize AAV vectors by targeting the vector genome with fluorescence *in situ* hybridization (FISH). However, the sensitivity of conventional FISH for DNA sequences below 5-10 kb is limited, a drawback that has precluded broader use of this technique in AAV and gene therapy research.

Signal amplification by exchange reaction (SABER) is a method that uses a strand-displacing polymerase and catalytic DNA hairpin to generate FISH probes containing long arrays of binding sites for fluorescent oligonucleotides (16). Compared to probes used in conventional FISH, SABER-FISH probes result in a 5- to 450-fold amplification of DNA and RNA signals, allowing for highly sensitive detection of nucleic acid-based molecules (16). Here, we describe a novel application of SABER-FISH that enables the visualization and quantification of individual AAV genomes in tissues. Using this technique, we examined AAV genomes in mice following subretinal injection of AAV vectors and demonstrate a direct relationship between the number of vector genomes inside a cell and its corresponding level of transgene expression. Our findings illustrate the versatility of SABER-FISH as a tool to study AAV vectors with the potential to expedite both preclinical and clinical efforts to develop AAV gene therapy.

Results

SABER-FISH detects fluorescent DNA puncta after subretinal delivery of AAV vectors

SABER-FISH probes were first synthesized to target the genome of AAV8-CMV-GFP, a serotype 8 AAV vector employing the commonly used cytomegalovirus (CMV) promoter to drive expression of GFP (Fig. 1*A* and *B*). AAV vectors possess a linear ssDNA genome that converts to double-stranded DNA before being processed to generate mRNA and protein (3). Probes were thus designed to recognize only the negative-sense strand of the AAV8-CMV-GFP genome to avoid binding of mRNA transcribed from the vector. A total of 47 probes were made

in vitro as previously described (16) and hybridized to tissues infected with AAV8-CMV-GFP. To model *in vivo* gene therapy, subretinal injections were performed in neonatal mice. Delivery of AAV8-CMV-GFP by this route resulted in strong pan-retinal GFP signal by 3 weeks post-injection (p.i.) (Fig. 1*C*), consistent with prior reports on the kinetics of AAV-mediated transgene expression (17,18).

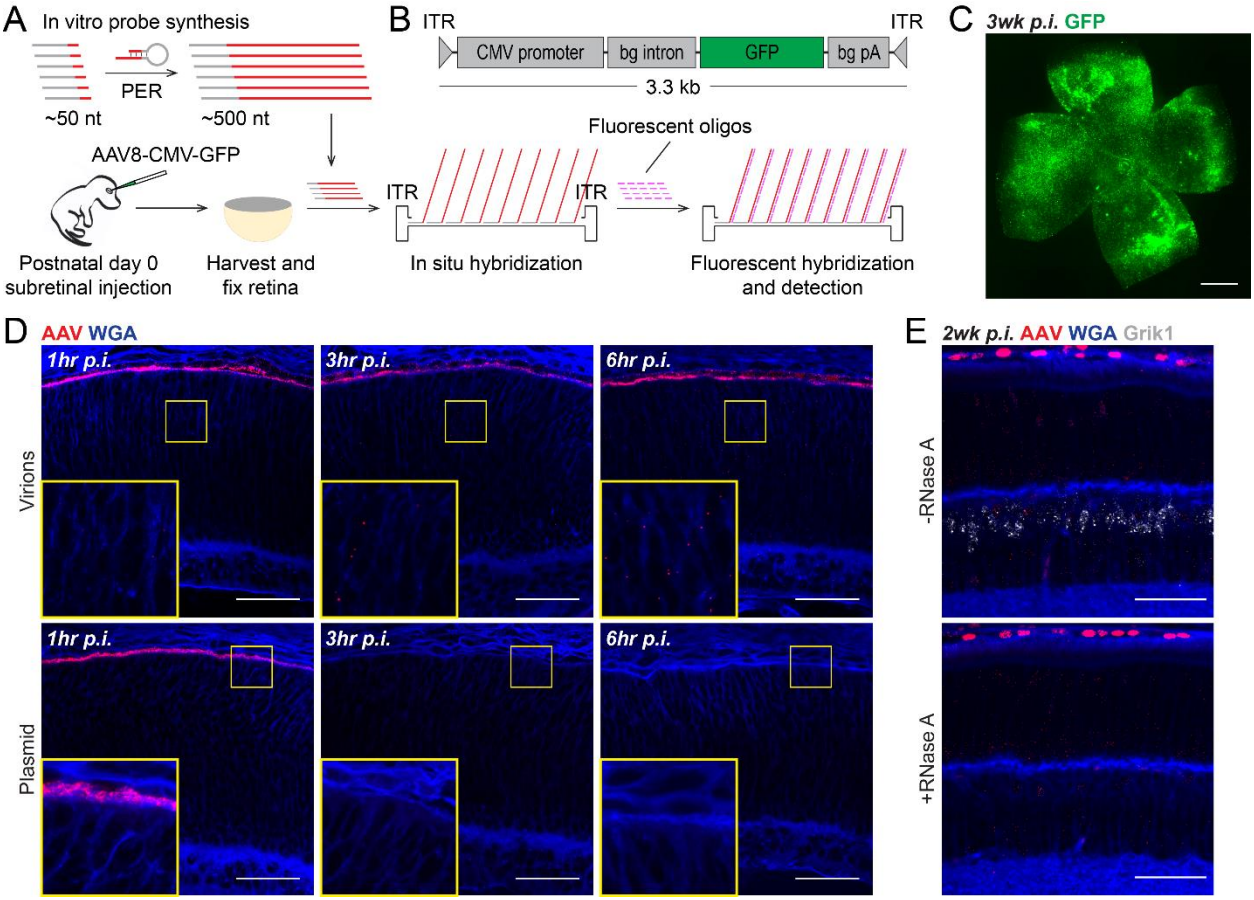

Figure 1. SABER-FISH detects fluorescent DNA puncta after subretinal delivery of AAV vectors. (**A**) Schematic of SABER-FISH protocol for detection of AAV genomes. SABER-FISH probes complementary to the negative-sense strand of the AAV8-CMV-GFP genome were synthesized *in vitro* and hybridized to fixed retinal tissue from mice that had been subretinally injected with the vector. Short fluorescent oligos were then hybridized to the primary SABER-FISH probes, allowing for signal amplification and fluorescent detection. (**B**) Schematic of AAV8-CMV-GFP vector design. (**C**) Representative image of a flat-mounted retina demonstrating pan-retinal GFP expression by 3 weeks after postnatal day 0 subretinal injection of 1 x 10^{12} vector genomes (vg)/mL of AAV8-CMV-GFP. Scale bar, 1mm. (**D**) Low and high magnification images of retinas at 1, 3, and 6 hours after subretinal injection of 1 x 10^{12} vg/mL of AAV8-CMV-GFP (top) or 1 mg/mL of plasmid encoding the AAV8-CMV-GFP sequence (bottom). Cell membranes were labeled with WGA. Scale bar, 50 µm. (**E**) Simultaneous detection of AAV8-CMV-GFP puncta and *Grik1* mRNA in sections from the same retina with or without RNase A treatment. Scale bar, 50 µm. nt, nucleotides; PER, primer exchange reaction; ITR, inverted terminal repeat; bg, beta-globin; pA, polyadenylation sequence.

Probes were initially tested after subretinal injection of either AAV8-CMV-GFP virions, which were predicted to infect and enter retinal cells, or AAV8-CMV-GFP plasmid, which was predicted to remain in the subretinal space. These locations were identified by using wheat germ agglutinin (WGA) to label cell membranes. One hour after both virion and plasmid injections, the subretinal space was filled with fluorescent puncta (Fig. 1*D*, left panels). However, at 3 and 6 hours p.i., puncta could be detected inside retinal cells only in the eyes receiving AAV8-CMV-GFP virions (Fig. 1*D*, center and right panels). To verify that these puncta corresponded to AAV genomes and not mRNA from the vector, tissues were treated with RNase A, which degrades RNA without affecting DNA. While treatment with RNase A eliminated SABER-FISH detection of *Grik1* mRNA, it had no effect on fluorescent puncta from AAV8-CMV-GFP (Fig, 1*E*), suggesting that the latter consisted of DNA. SABER-FISH thus allows for the detection of DNA puncta in eyes after subretinal injection of AAV vectors, with puncta visible inside retinal cells as early as 3 hours p.i.

SABER-FISH enables visualization of individual AAV genomes in the retina.

Does each DNA punctum detected by SABER-FISH represent a single AAV genome or multiple genomes in close proximity? To distinguish between these possibilities, a limiting dilution analysis was performed by subretinally injecting mice with five different titers of AAV8-CMV-GFP. If each AAV genome generated a single fluorescent punctum, we reasoned that an *x*-fold decrease in AAV vector titer would likewise result in an *x*-fold decrease in the number of puncta; i.e. there would be a linear relationship between vector titer and puncta count. Conversely, if a group of *y* genomes in close proximity were needed to detect each punctum, the same *x*-fold drop in vector titer should produce a x^y-fold drop in puncta, assuming the location of each genome was independently determined. Using previously described methods (16,19), cell boundaries in the neural retina could be delineated in 3D based on their labeling with WGA (Supplemental Fig. 1). Puncta in these images could then be computationally

assigned to cells, facilitating automated quantification of puncta in the retina (Supplemental Fig. 1). At 24 hours p.i., puncta in retinal cells were significantly increased in eyes receiving higher titers of AAV8-CMV-GFP and were absent from uninjected controls (Fig. 2*A* and *B*). The relationship between AAV vector titer and puncta count was strongly linear (Fig. 2*C*, R^2 = 0.9942), indicating that each DNA punctum visualized by SABER-FISH most likely corresponded to a single AAV genome.

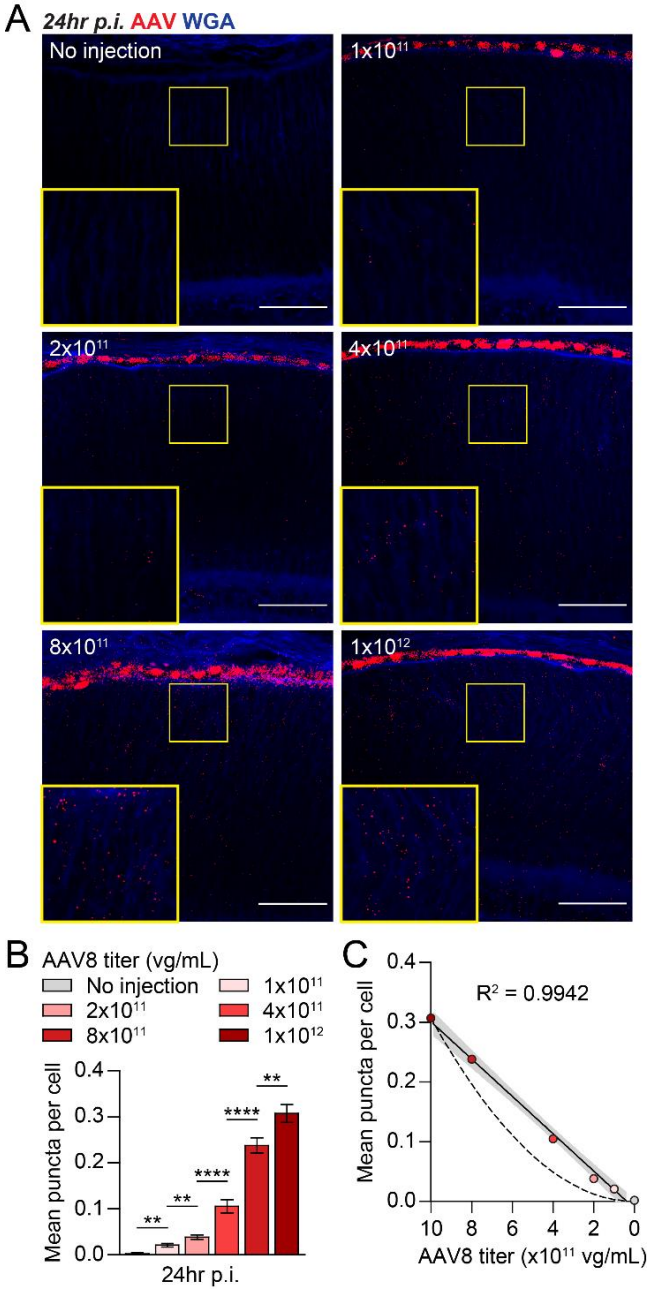

Figure 2. Quantification and limiting dilution analysis of fluorescent puncta after subretinal delivery of AAV vectors.

(**A**) Low and high magnification images of retinas at 24 hours after subretinal injection of the indicated titers of AAV8-CMV-GFP. Scale bar, 50 µm.

(**B**) Quantification of fluorescent puncta in cells of the retina with the conditions tested in (A). *n* = 477-1733 cells from 2-4 animals per group.

(**C**) Limiting dilution analysis of fluorescent puncta in retinas at 24 hours p.i. based on the data shown in (B). Solid line depicts linear regression for the plotted data with 95% confidence interval shown in gray and goodness-of-fit measured by R^2. Dotted line depicts expected relationship if puncta count were to decrease by the square of the vector titer, as would occur if two independent AAV genomes in the same location were required to detect each punctum. Data shown as mean ± SEM. ** *P*<0.01, **** *P*<0.0001 by two-tailed Student's t-test with Bonferroni correction.

To assess the overall integrity of individual AAV genomes after subretinal delivery, 24 of the 47 probes for AAV8-CMV-GFP were modified to enable detection of the 5' and 3' halves of the vector genome in separate fluorescent channels. Simultaneous detection of these partial genomes in the retina demonstrated colocalization in ~90% of cases at both 24 hours and 2 weeks p.i. (Fig 3*A* and *C*), suggesting that most AAV genomes are roughly of full-length. As a

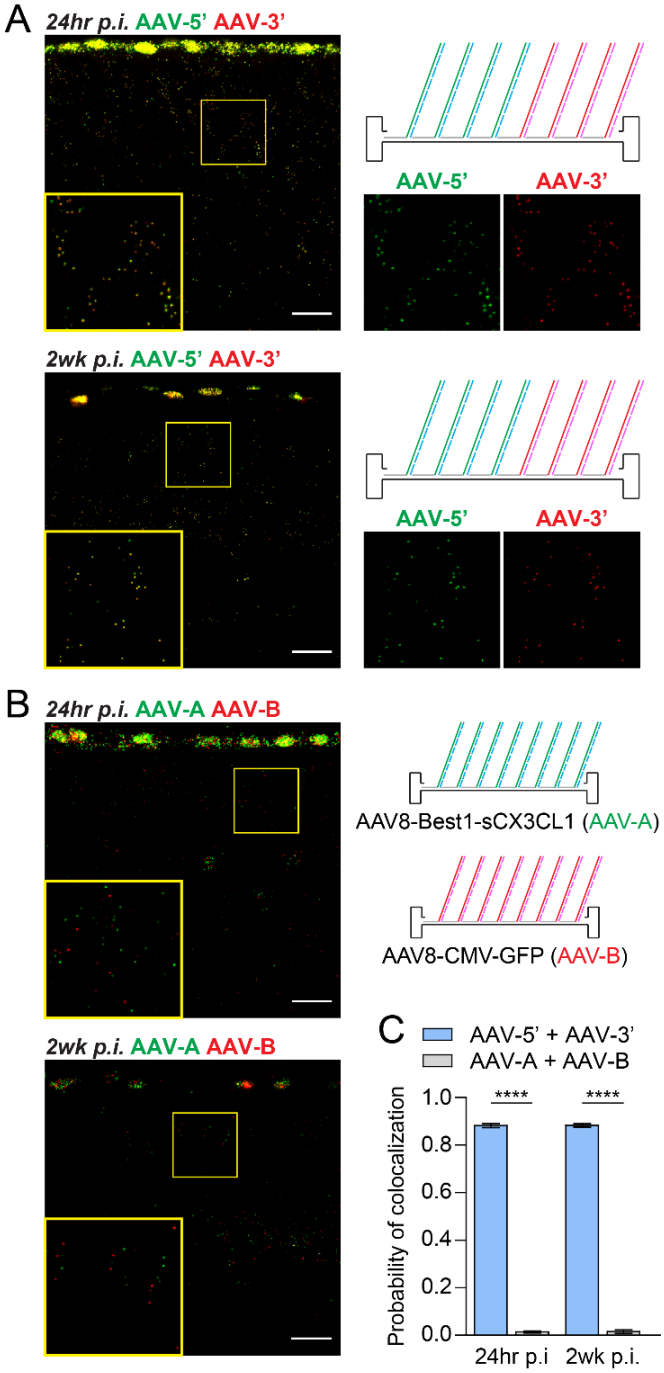

Figure 3. Detection of partial AAV genomes and genomes from multiple vectors with DNA SABER-FISH.

(**A**) Low and high magnification images of the 5' (AAV-5', green) and 3' (AAV-3', red) halves of the AAV8-CMV-GFP genome in retinas at 24 hours or 2 weeks after subretinal injection of 1 x 10^{12} vg/mL of AAV8-CMV-GFP. Colocalized green and red puncta appear yellow. Scale bar, 20 µm.

(**B**) Low and high magnification images of the AAV8-Best1-sCX3CL1 (AAV-A, green) and AAV8-CMV-GFP (AAV-B, red) genomes in retinas at 24 hours or 2 weeks after subretinal injection of 1 x 10^{12} vg/mL of each vector. Scale bar, 20 µm.

(**C**) Probability of green and red colocalization for the combinations tested in (A) and (B), defined as the fraction of puncta in the retina that colocalized with puncta of the other color. *n* = 3-5 animals per group. Data shown as mean ± SEM. **** *P*<0.0001 by two-tailed Student's t-test.

comparison, another set of probes was synthesized to target a different vector, AAV8-Best1-sCX3CL1 (20), which was co-injected with AAV8-CMV-GFP and analyzed at the same time points. Genomes from AAV8-Best1-sCX3CL1 and AAV8-CMV-GFP appeared randomly distributed in infected cells and showed colocalization in only ~1% of cases (Fig. 3*B* and *C*). Together, these data support the ability of SABER-FISH to track individual AAV genomes from one or multiple vectors in a quantifiable manner.

AAV8-CMV-GFP genomes correlate with GFP expression.

Following subretinal injection of AAV8-CMV-GFP in neonatal mice, GFP signal could be seen in three mature cell types: rod photoreceptors, cone photoreceptors, and the retinal pigment epithelium (RPE) (Fig. 4*A*). For each of these cell types, we employed SABER-FISH to ask how the number of AAV8-CMV-GFP genomes related to GFP expression. The outer nuclear layer (ONL) of the retina consists of the cell bodies of rods and cones, which can be identified by negative and positive staining for cone arrestin, respectively. SABER-FISH in these cell bodies was therefore combined with cone arrestin staining and detection of GFP to determine the distribution of AAV8-CMV-GFP genomes in GFP-negative and GFP-positive photoreceptors. For rods, 86.0% of GFP-negative cell bodies were devoid of AAV genomes, while 85.3% of GFP-positive cell bodies contained at least one genome with a mean of 2.1 per cell (Fig. 4*B*, *D*, and *G*). AAV8-CMV-GFP genomes in rods were thus highly predictive of GFP expression. For cones, AAV genomes were present in 91.2% of GFP-positive cell bodies with a mean of 2.5 per cell (Fig. 4*B*, *E*, and *G*). However, AAV genomes were also found in nearly half (48.0%) of GFP-negative cone cell bodies, suggesting that some cones may block AAV8-CMV-GFP from being expressed.

To analyze RPE cells, AAV8-CMV-GFP genomes were quantified in RPE nuclei labeled with 4′,6-diamidino-2-phenylindole (DAPI), as virtually all genomes in the RPE at 3 weeks p.i. aggregated in nuclei. Relative to photoreceptors, RPE nuclei on average contained much higher

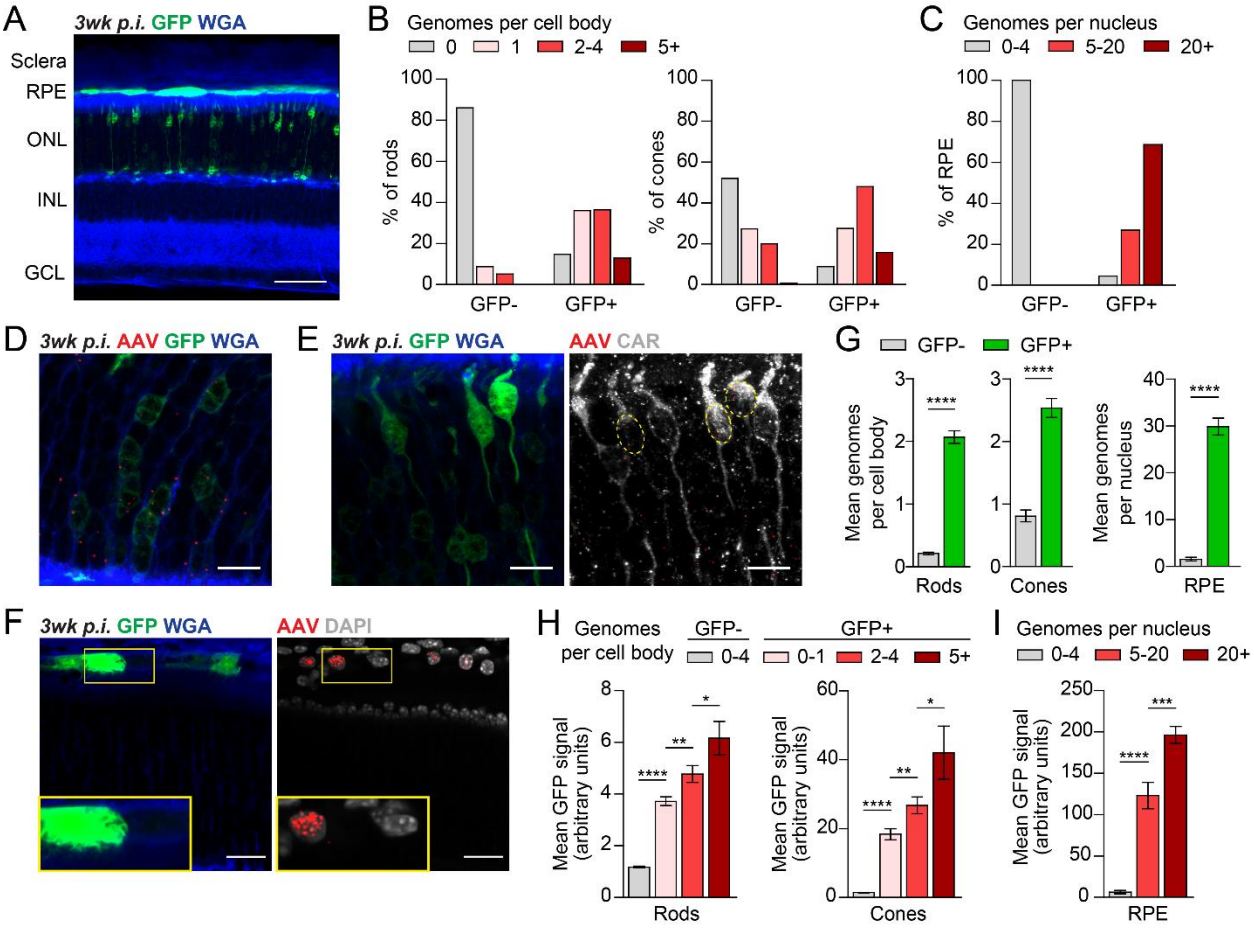

Figure 4. Comparison of AAV genomes and GFP expression in photoreceptors and RPE. (**A**) Representative section of an eye at 3 weeks after subretinal injection of 1 x 10^{12} vg/mL of AAV8-CMV-GFP demonstrating GFP expression in rods, cones, and RPE. Scale bar, 50 µm. (**B**, **C**) Distribution of AAV genomes in the cell bodies of GFP-negative and GFP-positive photoreceptors (B) and nuclei of GFP-negative and GFP-positive RPE (C). (**D-F**) Representative images of rods (D), cones (E), and RPE (F) at 3 weeks after subretinal injection of 1 x 10^{12} vg/mL of AAV8-CMV-GFP. Rods and cones were defined as CAR-negative and CAR-positive cells in the ONL, respectively. Nuclei were labeled with DAPI. Dotted lines in (E) indicate cell bodies of GFP-positive cones. Scale bars, 10 µm for (D) and (E), 20 µm for (F). (**G**) Mean number of AAV genomes in the cell bodies of GFP-negative and GFP-positive photoreceptors and nuclei of GFP-negative and GFP-positive RPE. (**H**, **I**) Mean intensity of GFP expression in photoreceptors (H) and RPE (I) relative to the number of AAV genomes. *n* = 81-850 cell bodies or nuclei from 4-8 animals per group for (B), (C), (G), (H), and (I). Data shown as mean ± SEM. * *P*<0.05, ** *P*<0.01, *** *P*<0.001, **** *P*<0.0001 by two-tailed Student's t-test. ONL, outer nuclear layer; INL, inner nuclear layer; GCL, ganglion cell layer; CAR, cone arrestin.

numbers of AAV genomes. While all GFP-negative RPE nuclei examined had four or fewer copies of AAV8-CMV-GFP, most GFP-positive RPE nuclei had over 20 genomes with a mean of 29.9 per nucleus (Fig. 4*C*, *F*, and *G*). For all three GFP-expressing cell types, cells with more AAV8-CMV-GFP genomes on average had significantly higher GFP expression (Fig. 4*H* and *I*).

Interestingly, GFP signal in cones and the RPE was much greater than that in rods infected with the same number of AAV8-CMV-GFP genomes. Additionally, there were several cell types, including horizontal cells and scleral fibroblasts, that remained GFP-negative despite receiving multiple copies of the vector (Supplemental Fig. 2). Collectively, these findings underscore the variability in expression among different cell types with the CMV promoter and provide direct evidence that the number of AAV genomes per cell correlates with the level of transgene expression.

Discussion

In this study, we used SABER to amplify FISH signals from AAV genomes, allowing for the detection and quantification of AAV vectors *in situ*. These genomes could be seen in the mouse retina as early as 3 hours after vector delivery, consistent with prior live imaging experiments of AAV vectors in cell culture (21). Based on a limiting dilution analysis, we determined that the AAV vectors visualized by SABER-FISH were most likely individual AAV genomes rather than concatemers of multiple vectors. While this conclusion assumed that AAV genomes localize independently within each cell, which may not necessarily be the case, it was supported by the high concordance between AAV8-CMV-GFP genomes and GFP expression, particularly in rods. Indeed, AAV genomes were absent from and present in ~85% of GFP-negative and GFP-positive rods, respectively, with many GFP-positive rods containing only one AAV genome. Our findings thus suggest that infection with a single AAV virion in rods is usually sufficient to drive transgene expression. In contrast, ~48% of cones in our study were GFP-negative despite experiencing at least one AAV transduction event. Whether this heterogeneity among cones was due to cell-intrinsic differences related to the CMV promoter or some uncharacterized stochastic process will be interesting to determine considering the growing number of gene therapy applications targeting photoreceptors (22–24).

Outside of the retina, we observed a massive accumulation of AAV genomes in RPE nuclei following subretinal injection of AAV8-CMV-GFP. Compared with rods and cones in the same eye, infected RPE on average contained 10-fold the number of AAV genomes. This higher concentration of AAV genomes in RPE cells may explain why transgenes delivered via AAV8 vectors are typically expressed in the RPE several days before they appear in the retina (18). In examining the rest of the eye, we additionally detected AAV8-CMV-GFP genomes in vimentin-positive fibroblasts of the sclera. While these fibroblasts did not express GFP, their transduction suggests that subretinally administered AAV vectors can also reach cells in the eye beyond the retina and RPE.

Unlike in animal studies, AAV vectors in clinical trials are administered without a reporter gene such as GFP to minimize the total dose of vectors and potential immunogenicity (25). Identification of infected cells in patient samples therefore relies on the detection of vector transgenes, frequently by histology or real-time polymerase chain reaction (RT-PCR). Unfortunately, not all transgenes from AAV vectors are amenable to antibody staining or RNA FISH due to inadequate reagents, silencing of the gene, or high endogenous expression in uninfected tissues. In these cases, RT-PCR can be used to verify successful AAV transduction, but at the expense of spatial information on the cell types infected. SABER-FISH offers a complementary assay that directly visualizes AAV vectors and identifies infected cells in a quantitative manner. Furthermore, as demonstrated here, the method can be combined with RNA FISH and immunohistochemistry to label specific cell types, as well as SABER-FISH for other AAV vectors. We thus anticipate that SABER-FISH will be of particular value for gene therapy studies in which the locations and identities of vector-transduced cells are otherwise difficult to discern.

Another emerging issue for AAV gene therapy, especially at high doses, is cellular toxicity mediated by the immune system or possibly directly by the vector (26–28). The mechanisms underlying these processes are not well understood, but in multiple cases have

resulted in clinically significant inflammation limiting the efficacy of treatment (29–31). Recently, our group developed Probe-Seq, which uses SABER-FISH probes targeting RNAs to fluorescently isolate cell populations for transcriptional profiling (32). We envision that combining Probe-Seq with SABER-FISH for AAV vectors could allow for the purification of infected cells prior to the onset of transgene expression, enabling closer investigation of the pathways responsible for the toxic response to AAV vectors. This strategy would expedite the development of safe yet efficacious gene therapy programs and might also be extended to other viral vectors to more generically interrogate acutely transduced cells.

Finally, one potential application of SABER-FISH not explored in this study is the development of an efficient method for functional AAV vector titering. Many groups, including our own, assay AAV vectors with RT-PCR to adjust the concentration of different stocks and ensure comparisons between vectors are fair and reproducible (33). While this approach corrects for variations in the number of AAV genomes per unit volume, it cannot account for how many of those genomes are properly packaged and capable of infecting cells. Functional titering, which involves transducing cells with a given vector and measuring some output of transgene expression, can instead be used to determine the infectivity of vector stocks. However, the process is often time-consuming, since transgenes may take several days to become detectable, and it requires the promoter of the vector to be expressed in the tested cells. As shown in this study, SABER-FISH can visualize and quantify intracellular AAV vectors within hours of vector delivery, bypassing the major limitations of current titering methods. An optimized SABER-FISH protocol for functional AAV vector titering may therefore further facilitate the dissemination of AAV-based therapies.

Materials and Methods

Animals. All mouse experiments were approved by the IACUC of Harvard University in accordance with institutional guidelines and performed using CD-1 (#022) animals purchased

from Charles River Laboratories. Mice were maintained at Harvard Medical School on a 12-hour alternating light and dark cycle.

***Vector production and delivery*.** The AAV8-CMV-GFP vector plasmid was obtained from the Harvard DF/HCC DNA Resource Core (clone ID: EvNO00061595) and consisted of a CMV promoter, beta-globin intron, cDNA sequence for GFP, and beta-globin polyadenylation sequence. The AAV8-Best1-sCX3CL1 vector plasmid was synthesized as previously reported (20) and consisted of a Best1 promoter, SV40 intron, cDNA sequence for soluble CX3CL1, woodchuck hepatitis virus posttranscriptional regulatory element, and bovine growth hormone polyadenylation sequence. Recombinant serotype 8 AAVs were produced, titered, and subretinally injected into postnatal day 0-1 mouse eyes as described in Chapter 2. For plasmid injections, ~0.25 µL of purified plasmid (1 mg/mL) was introduced into the subretinal space.

***Probe design and synthesis*.** SABER-FISH probes targeting the genomes of AAV8-CMV-GFP and AAV8-Best1-sCX3CL1 were designed *in silico* using ApE software. Unless otherwise specified, probes were generated to recognize only the negative-sense strand of the vector. For each AAV, we first identified a list of non-overlapping oligonucleotides that were 1) complementary to the genome, 2) at least 36 nucleotides long, and 3) predicted to have a melting temperature between 67°C and 71°C. A 9-nucleotide primer (CATCATCAT or CAACTTAAC) with a TTT linker was appended to the 3' ends of these oligonucleotides to finalize the probe sequences, which were then ordered from IDT with standard desalting in a 96-well plate at the 10 nM synthesis scale. Probes were pooled into a single tube with a multi-channel pipette and extended to ~500 nucleotides using a previously described primer exchange reaction, in which a catalytic hairpin and strand-displacing polymerase repeatedly added the same sequence to the end of the 9-nucleotide primer (16). Extended probe sets were subsequently purified with MinElute PCR purification columns (Qiagen) and eluted in nuclease-free water.

Eye dissections. Freshly enucleated eyes were dissected in phosphate buffer saline (PBS) to remove the cornea, iris, ciliary body, and lens. The remaining eye cup was fixed, cryoprotected, and cut into 30 µm sections as described in Chapter 2. Flat-mounts of retinas were likewise prepared as described in Chapter 2.

SABER-FISH. Detection of AAV genomes and cell type mRNAs by SABER-FISH was performed in 350 µL chamber wells (Grace Bio-Labs) using the RNA ISH protocol from Kishi et al. with minor modifications (16). Briefly, tissues were sectioned onto Superfrost Plus Micro slides (VWR) pretreated for 30 minutes with a 0.3 mg/ml solution of poly-D lysine in 2X borate buffer. After rehydration with PBSTw (PBS + 0.1% Tween-20), samples were washed with a wash-hybridization solution (40% formamide + 1% Tween-20 + 2X SSCT) at 43°C followed by incubation in hybridization solution (40% formamide + 10% dextran sulfate + 1% Tween-20 + 2X SSCT) containing 8.33 µg/mL of each probe set for 16 hours at 43°C. Samples subsequently underwent two 30-minute washes with wash-hybridization solution at 43°C and two 5-minute washes with PBSTw at room temperature. Hybridized probes were then detected by incubating with 0.2 µM of fluorescent oligonucleotides (IDT) in PBS + 0.2% Tween-20 for 30 minutes at 37°C. Cell membranes were labeled by staining with 10 µg/mL of WGA (Biotium) in PBSTw for 2 hours at room temperature. Nuclei were labeled by staining with 0.5 µg/mL of DAPI (Invitrogen) in PBS for 5 minutes at room temperature. If applicable, samples were treated with 100 µg/mL of RNase A (Thermo Scientific) in PBSTw for 30 minutes at 37°C prior to the first use of wash-hybridization solution. Slides were mounted with an 80% glycerol medium containing 1× PBS, 20 mM Tris pH 8.0, and 2.5 mg/mL of propyl gallate.

Immunostaining. After FISH and labeling of cell membranes with WGA, tissues were treated with blocking solution (PBS + 5% goat serum + 0.1% Triton X-100) for one hour at room temperature followed by incubation with either 1:3000 of rabbit anti-mouse cone arrestin (Millipore, AB15282) or 1:500 of rabbit anti-mouse vimentin (Abcam, ab92547) in blocking solution for 16 hours at 4°C. Tissues were subsequently washed with PBS and incubated with

1:1000 of donkey anti-rabbit Alexa Fluor 647 secondary antibody (Jackson ImmunoResearch, 711-605-152) in PBS for 2 hours at room temperature prior to slide mounting.

***Image acquisition and analysis*.** Imaging was conducted on a Zeiss LSM710 single-point scanning confocal microscope using 20x air, 40x oil, and 63x oil objectives. Laser lines were 405, 488, 561, and 633 nm. FISH images were acquired as *z*-stacks, processed with ImageJ, and displayed as maximum-intensity projections of equal depth for images within the same figure. For all images, the RPE-facing side of the retina was oriented toward the top. Automated cell segmentation and puncta detection were performed as previously described with minor modifications (16). For retinal samples, cells in 3D *z*-stacks were first segmented based on WGA labeling of cell membranes using ACME, an open-source segmentation software (19). Puncta were then detected and quantified with PD3D (github.com/ewest11/PD3D), a MATLAB script employing a Laplacian of Gaussian method to distinguish puncta from tissue background and assign them to segmented cell bodies. Cells adjoining any boundary of the 3D image or located outside the neural retina were computationally removed to confine analyses of puncta to whole retinal cells. For RPE, puncta were again detected using PD3D but manually assigned to RPE nuclei labeled with DAPI. Quantification of colocalized puncta in 3D images were performed using coloc3D (mathworks.com/matlabcentral/fileexchange/5694-coloc3d), a MATLAB script identifying overlapping particles in *z*-stack images. Measurements of GFP expression were manually performed in ImageJ by drawing a mask around each cell body for photoreceptors or nucleus for RPE and recording the mean GFP intensity.

***Statistics*.** Statistical analyses were performed using GraphPad Prism software. For all statistical tests, a *P*-value less than 0.05 was considered significant.

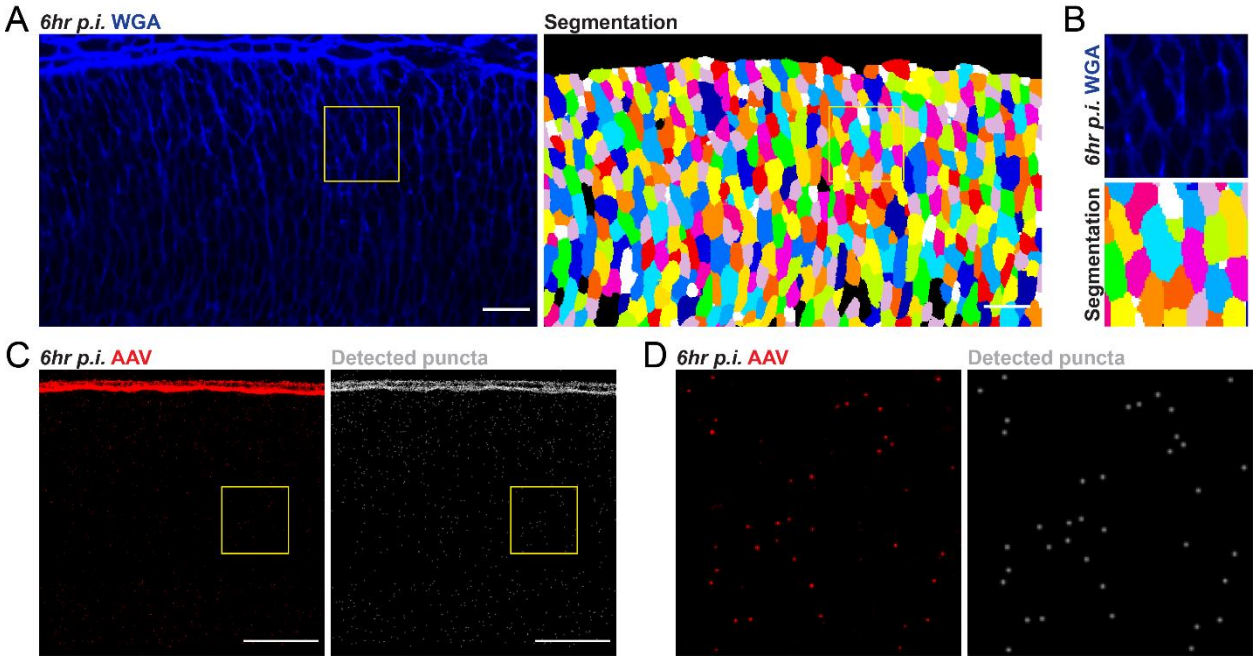

Supplemental Figure 1. Automated cell segmentation and puncta detection. (**A**, **B**) Low (A) and high (B) magnification images of cell membranes in the retina labeled with WGA and the corresponding output following automated cell segmentation (19). Different colors indicate boundaries of adjoining cell bodies. Scale bar, 20 µm. (**C**, **D**) Low (C) and high (D) magnification images of fluorescent puncta in the retina at 6 hours after subretinal injection of AAV8-CMV-GFP and the corresponding output following automated puncta detection (16). Scale bar, 50 µm.

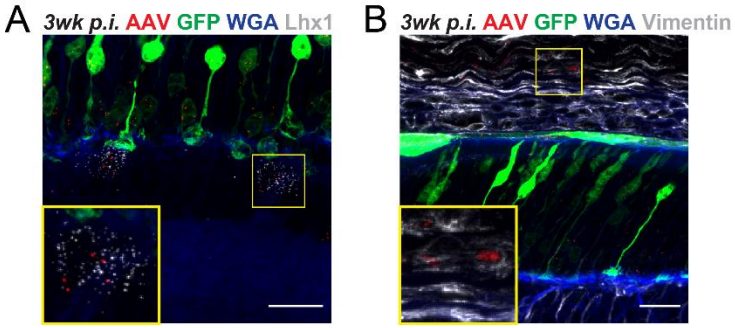

Supplemental Figure 2. AAV genomes in non-GFP expressing cell types after subretinal delivery of AAV8-CMV-GFP. (**A**) Low and high magnification images of AAV genomes at 3 weeks p.i. in GFP-negative horizontal cells, identified by their expression of *Lhx1* mRNA. Scale bar, 20 µm. (**B**) Low and high magnification images of AAV genomes at 3 weeks p.i. in GFP-negative fibroblasts in the sclera, identified by positive staining for vimentin. Scale bar, 20 µm.

References

1. Hermonat PL, Muzyczka N. Use of adeno-associated virus as a mammalian DNA cloning vector: Transduction of neomycin resistance into mammalian tissue culture cells. Proc Natl Acad Sci U S A. 1984;81(20 I):6466–70.
2. Tratschin JD, West MH, Sandbank T, Carter BJ. A human parvovirus, adeno-associated virus, as a eucaryotic vector: transient expression and encapsidation of the procaryotic gene for chloramphenicol acetyltransferase. Mol Cell Biol. 1984 Oct;4(10):2072–81.
3. Daya S, Berns KI. Gene therapy using adeno-associated virus vectors. Vol. 21, Clinical Microbiology Reviews. 2008. p. 583–93.
4. Sehara Y, Fujimoto K, Ikeguchi K, Katakai Y, Ono F, Takino N, et al. Persistent Expression of Dopamine-Synthesizing Enzymes 15 Years After Gene Transfer in a Primate Model of Parkinson's Disease. Hum Gene Ther Clin Dev. 2017 Jun;28(2):74–9.
5. Srivastava A, Lusby EW, Berns KI. Nucleotide sequence and organization of the adeno-associated virus 2 genome. J Virol. 1983 Feb;45(2):555–64.
6. Berns KI, Adler S. Separation of two types of adeno-associated virus particles containing complementary polynucleotide chains. J Virol. 1972 Feb;9(2):394–6.
7. Straus SE, Sebring ED, Rose JA. Concatemers of alternating plus and minus strands are intermediates in adenovirus associated virus DNA synthesis. Proc Natl Acad Sci U S A. 1976;73(3):742–6.
8. Lusby E, Fife KH, Berns KI. Nucleotide sequence of the inverted terminal repetition in adeno-associated virus DNA. J Virol. 1980 May;34(2):402–9.
9. Smith RH. Adeno-associated virus integration: Virus versus vector. Vol. 15, Gene Therapy. 2008. p. 817–22.
10. Penaud-Budloo M, Le Guiner C, Nowrouzi A, Toromanoff A, Cherel Y, Chenuaud P, et al. Adeno-Associated Virus Vector Genomes Persist as Episomal Chromatin in Primate Muscle. J Virol. 2008 Aug 15;82(16):7875–85.
11. Maguire AM, Simonelli F, Pierce EA, Pugh EN, Mingozzi F, Bennicelli J, et al. Safety and Efficacy of Gene Transfer for Leber's Congenital Amaurosis. N Engl J Med. 2008 May 22;358(21):2240–8.
12. Mendell JR, Al-Zaidy S, Shell R, Arnold WD, Rodino-Klapac LR, Prior TW, et al. Single-Dose Gene-Replacement Therapy for Spinal Muscular Atrophy. N Engl J Med. 2017 Nov 2;377(18):1713–22.
13. Kothari P, De BP, He B, Chen A, Chiuchiolo MJ, Kim D, et al. Radioiodinated Capsids Facilitate in Vivo Non-Invasive Tracking of Adeno-Associated Gene Transfer Vectors. Sci Rep. 2017 Jan 6;7.
14. Kelich JM, Ma J, Dong B, Wang Q, Chin M, Magura CM, et al. Super-resolution imaging of nuclear import of adeno-associated virus in live cells. Mol Ther - Methods Clin Dev. 2015 Apr 29;2:15047.
15. Lux K, Goerlitz N, Schlemminger S, Perabo L, Goldnau D, Endell J, et al. Green Fluorescent Protein-Tagged Adeno-Associated Virus Particles Allow the Study of Cytosolic and Nuclear Trafficking. J Virol. 2005 Sep 15;79(18):11776–87.
16. Kishi JY, Lapan SW, Beliveau BJ, West ER, Zhu A, Sasaki HM, et al. SABER amplifies FISH: enhanced multiplexed imaging of RNA and DNA in cells and tissues. Nat Methods. 2019 Jun 1;16(6):533–44.
17. Sarra GM, Stephens C, Schlichtenbrede FC, Bainbridge JWB, Thrasher AJ, Luthert PJ, et al. Kinetics of transgene expression in mouse retina following sub-retinal injection of

recombinant adeno-associated virus. Vision Res. 2002;42(4):541–9.

18. Natkunarajah M, Trittibach P, McIntosh J, Duran Y, Barker SE, Smith AJ, et al. Assessment of ocular transduction using single-stranded and self-complementary recombinant adeno-associated virus serotype 2/8. Gene Ther. 2008 Mar;15(6):463–7.
19. Mosaliganti KR, Noche RR, Xiong F, Swinburne IA, Megason SG. ACME: Automated Cell Morphology Extractor for Comprehensive Reconstruction of Cell Membranes. PLoS Comput Biol. 2012 Dec;8(12).
20. Wang SK, Xue Y, Rana P, Hong CM, Cepko CL. Soluble CX3CL1 gene therapy improves cone survival and function in mouse models of retinitis pigmentosa. Proc Natl Acad Sci. 2019 Apr 29;116(20):201901787.
21. Cervelli T, Palacios JA, Zentilin L, Mano M, Schwartz RA, Weitzman MD, et al. Processing of recombinant AAV genomes occurs in specific nuclear structures that overlap with foci of DNA-damage-response proteins. J Cell Sci. 2008 Feb 1;121(3):349–57.
22. Rakoczy EP, Lai CM, Magno AL, Wikstrom ME, French MA, Pierce CM, et al. Gene therapy with recombinant adeno-associated vectors for neovascular age-related macular degeneration: 1 year follow-up of a phase 1 randomised clinical trial. Lancet. 2015 Dec 1;386(10011):2395–403.
23. Pichard V, Provost N, Mendes-Madeira A, Libeau L, Hulin P, Tshilenge KT, et al. AAV-mediated gene therapy halts retinal degeneration in PDE6β-deficient dogs. Mol Ther. 2016 May 1;24(5):867–76.
24. Banin E, Gootwine E, Obolensky A, Ezra-Elia R, Ejzenberg A, Zelinger L, et al. Gene Augmentation Therapy Restores Retinal Function and Visual Behavior in a Sheep Model of CNGA3 Achromatopsia. Mol Ther. 2015 Sep 3;23(9):1423–33.
25. Gao G, Wang Q, Calcedo R, Mays L, Bell P, Wang L, et al. Adeno-associated virus-mediated gene transfer to nonhuman primate liver can elicit destructive transgene-specific T cell responses. Hum Gene Ther. 2009 Sep 1;20(9):930–42.
26. Xiong W, Wu DM, Xue Y, Wang SK, Chung MJ, Ji X, et al. AAV cis-regulatory sequences are correlated with ocular toxicity. Proc Natl Acad Sci U S A. 2019 Mar 4;116(12):5785–94.
27. Hinderer C, Katz N, Buza EL, Dyer C, Goode T, Bell P, et al. Severe Toxicity in Nonhuman Primates and Piglets Following High-Dose Intravenous Administration of an Adeno-Associated Virus Vector Expressing Human SMN. Hum Gene Ther. 2018 Mar 1;29(3):285–98.
28. Colella P, Ronzitti G, Mingozzi F. Emerging Issues in AAV-Mediated In Vivo Gene Therapy. Vol. 8, Molecular Therapy - Methods and Clinical Development. Cell Press; 2018. p. 87–104.
29. Manno CS, Arruda VR, Pierce GF, Glader B, Ragni M, Rasko J, et al. Successful transduction of liver in hemophilia by AAV-Factor IX and limitations imposed by the host immune response. Nat Med. 2006 Mar;12(3):342–7.
30. Dimopoulos IS, Hoang SC, Radziwon A, Binczyk NM, Seabra MC, MacLaren RE, et al. Two-Year Results After AAV2-Mediated Gene Therapy for Choroideremia: The Alberta Experience. Am J Ophthalmol. 2018;193:130–42.
31. Cukras C, Wiley HE, Jeffrey BG, Sen HN, Turriff A, Zeng Y, et al. Retinal AAV8-RS1 Gene Therapy for X-Linked Retinoschisis: Initial Findings from a Phase I/IIa Trial by Intravitreal Delivery. Mol Ther. 2018 Sep 5;26(9):2282–94.
32. Amamoto R, Garcia MD, West ER, Choi J, Lapan SW, Lane EA, et al. Probe-Seq

enables transcriptional profiling of specific cell types from heterogeneous tissue by RNA-based isolation. Elife. 2019 Dec 9;8.

33. Veldwijk MR, Topaly J, Laufs S, Hengge UR, Wenz F, Zeller WJ, et al. Development and optimization of a real-time quantitative PCR-based method for the titration of AAV-2 vector stocks. Mol Ther. 2002 Jul 1;6(2):272–8.

Chapter 7: Conclusions and future directions

There are several lines of investigation currently under development based on the work presented in this thesis. In particular, the promising findings of cone and vision preservation with AAV8-sCX3CL1 and AAV8-TGFB1 in mouse models of RP have sparked collaborations to test these vectors in non-human primates and potentially human patients. If successful, these vectors would provide a much-needed mutation-independent treatment option for the many patients with RP for whom mutation-specific gene therapy is unrealistic. In addition, although AAV8-sCX3CL1 and AAV8-TGFB1 were originally designed to target RP, it is possible that these vectors are similarly protective for photoreceptors in other degenerative retinal conditions such as age-related macular degeneration (AMD). As AMD affects an estimated 170 million people worldwide (1), this would tremendously expand the number of individuals who could benefit from ocular gene therapy.

Our data on TGF-β1 in RP further indicate that microglia can dramatically affect the rate of cone degeneration, since microglia were necessary for AAV8-TGFB1 to rescue cones. We anticipate that using genomic and proteomic methods to more precisely elucidate how TGF-β1 induces microglia-mediated cone survival may thus lead to the identification of novel therapeutic targets for this disease. Outside of the eye, microglial dysfunction has moreover been implicated in numerous pathologies of the central nervous system, including Alzheimer's disease, Parkinson's disease, and amyotrophic lateral sclerosis (2–4). Modulation of dysregulated microglia by TGF-β1 may therefore also be beneficial in some of these devastating disorders, an avenue which we are actively exploring using mouse models of neurodegeneration.

The successful mitigation of AAV vector toxicity in both mice and pigs with the TLR9-blocking strategy described here argues for the incorporation of these inhibitory oligonucleotides in human gene therapy trials. Indeed, despite convincing rescue with AAV vectors in multiple preclinical models of eye disease (5–7), gene therapy for these conditions in patients has produced mixed results, possibly due to the masking of treatment effects by dose-dependent

inflammation (8,9). Suppressing ocular toxicity and inflammation with TLR9-blocking sequences in future clinical studies would reduce confounding from host immunity and could be especially useful for AAV vectors being considered for intravitreal administration. Unlike subretinal injections, intravitreal injections do not require a surgery or general anesthesia and are routinely performed as office procedures in ophthalmology clinics. However, intravitreal delivery of AAV vectors has also been shown to be more immunogenic (10), making it a less desirable choice for trials trying to establish safety and tolerability. By helping minimize this immunogenicity, our TLR9-blocking approach may enable more AAV vectors to be delivered intravitreally. Such a development would vastly improve patient accessibility to ocular gene therapy by allowing individuals to receive AAV vectors without having to undergo an eye surgery.

Finally, it is evident that TLR9-independent immune responses to AAV vectors are also present in the eye, as blocking of TLR9 significantly alleviated vector-induced toxicity but did not eliminate all ocular pathologies. Specifically, antibodies directed against the AAV capsid and transgene are known to substantially lessen the efficacy of gene therapy (11), and there may be other immune or non-immune pathways contributing to vector toxicity that have yet to be identified. To develop AAV vectors capable of safe administration even at high doses, a more comprehensive and mechanistic understanding of the response to AAV transduction in different cell types is warranted. With SABER-FISH, we can now distinguish infected and uninfected cells in the eye as early as 3 hours post-vector delivery, well before the onset of any reporter gene. Using this technique, we plan to interrogate individual cells shortly after AAV transduction and, by comparing them with untransduced populations, pinpoint the cell types ultimately responsible for triggering vector toxicity.

References

1. Pennington KL, DeAngelis MM. Epidemiology of age-related macular degeneration (AMD): associations with cardiovascular disease phenotypes and lipid factors. Eye Vis (London, England). 2016;3:34.
2. Block ML, Zecca L, Hong J-S. Microglia-mediated neurotoxicity: uncovering the molecular mechanisms. Nat Rev Neurosci. 2007 Jan;8(1):57–69.
3. Smith JA, Das A, Ray SK, Banik NL. Role of pro-inflammatory cytokines released from microglia in neurodegenerative diseases. Brain Res Bull. 2012 Jan 4;87(1):10–20.
4. Subhramanyam CS, Wang C, Hu Q, Dheen ST. Microglia-mediated neuroinflammation in neurodegenerative diseases. Semin Cell Dev Biol. 2019 Oct;94:112–20.
5. Park TK, Wu Z, Kjellstrom S, Zeng Y, Bush RA, Sieving PA, et al. Intravitreal delivery of AAV8 retinoschisin results in cell type-specific gene expression and retinal rescue in the Rs1-KO mouse. Gene Ther. 2009 Jul;16(7):916–26.
6. Byrne LC, Oztürk BE, Lee T, Fortuny C, Visel M, Dalkara D, et al. Retinoschisin gene therapy in photoreceptors, Müller glia or all retinal cells in the Rs1h-/- mouse. Gene Ther. 2014 Jun;21(6):585–92.
7. Tolmachova T, Tolmachov OE, Barnard AR, De Silva SR, Lipinski DM, Walker NJ, et al. Functional expression of Rab escort protein 1 following AAV2-mediated gene delivery in the retina of choroideremia mice and human cells ex vivo. J Mol Med. 2013 Jul;91(7):825–37.
8. Cukras C, Wiley HE, Jeffrey BG, Sen HN, Turriff A, Zeng Y, et al. Retinal AAV8-RS1 Gene Therapy for X-Linked Retinoschisis: Initial Findings from a Phase I/IIa Trial by Intravitreal Delivery. Mol Ther. 2018 Sep 5;26(9):2282–94.
9. Dimopoulos IS, Hoang SC, Radziwon A, Binczyk NM, Seabra MC, MacLaren RE, et al. Two-Year Results after AAV2-Mediated Gene Therapy for Choroideremia: The Alberta Experience. Am J Ophthalmol. 2018;193:130–42.
10. Reichel FF, Dauletbekov DL, Klein R, Peters T, Ochakovski GA, Seitz IP, et al. AAV8 Can Induce Innate and Adaptive Immune Response in the Primate Eye. Mol Ther. 2017 Dec 6;25(12):2648–60.
11. Mingozzi F, High K a. Immune responses to AAV vectors : overcoming barriers to successful gene. Blood. 2013;122(1):23–36.

Glossary: Abbreviations

AAV:	adeno-associated viral
AMD:	age-related macular degeneration
ANOVA:	analysis of variance
bg	beta-globin
bGH:	bovine growth hormone
cDNA:	complementary DNA
CAR:	cone arrestin
CD:	cluster of differentiation
CMV:	cytomegalovirus
CNS:	central nervous system
CpG:	cytosine-phosphate-guanine
CSF1R:	colony stimulating factor 1 receptor
CX3CL1:	C-X3-C motif chemokine ligand 1
CX3CR1:	CX3C chemokine receptor 1
C1qa:	complement C1q subcomponent subunit A
DAMP:	damage-associated molecular pattern
DAPI:	4′,6-diamidino-2-phenylindole
DC:	dendritic cell
DNA:	deoxyribonucleic acid
dpi:	days post-injection
ELISA:	enzyme-linked immunosorbent assay
ELISpot:	enzyme-linked immune absorbent spot
ERG:	electroretinography
FACS:	fluorescence-activated cell sorting
FAM:	fluorescein amidite
FDA:	Food and Drug Administration
FFB:	final formulation buffer
FISH:	fluorescence *in situ* hybridization
FIX:	factor IX
Gapdh:	glyceraldehyde 3-phosphate dehydrogenase
GCL:	ganglion cell layer
GFAP:	glial fibrillary acidic protein
GFP:	green fluorescent protein
GSEA:	gene set enrichment analysis
HEK:	human embryonic kidney
hpi:	hours post-injection
Iba1:	ionized calcium binding adaptor molecule 1
Ifn:	interferon
Il:	interleukin
INL:	inner nuclear layer
io:	inflammation-inhibiting oligonucleotide
IRD:	inherited retinal disease
IS:	inner segment

kb:	kilobase
LCA:	Leber’s congenital amaurosis
NF-kB:	nuclear factor kappa-light-chain-enhancer of activated B cells
NHP:	non-human primate
ns / N.S.:	not significant
nt:	nucleotide
OCT:	optical coherence tomography
ODN:	oligodeoxyribonucleotide
ONL:	outer nuclear layer
OS:	outer segment
P:	postnatal day
pA:	polyadenylation
PBMC:	peripheral blood mononuclear cell
PBS:	phosphate-buffered saline
PCR:	polymerase chain reaction
PEG:	polyethylene glycol
PER:	primer exchange reaction
PNA:	peanut agglutinin
RedO:	red opsin
Rho:	rhodopsin
RK:	rhodopsin kinase
RNA:	ribonucleic acid
RP:	retinitis pigmentosa
RPE:	retinal pigment epithelium
RT-PCR:	real-time polymerase chain reaction
SABER:	signal amplification by primer exchange reaction
sc:	self-complementary
SD:	standard deviation
SEM:	standard error of the mean
ss:	single-stranded
SV40:	simian virus 40
TGF-β:	transforming growth factor beta
TGFBR:	transforming growth factor beta receptor
TLR:	Toll-like receptor
Tmem119:	transmembrane protein 119
Tnf:	tumor necrosis factor
TTR:	transthyretin
UbiC:	ubiquitin C
UTR:	untranslated region
vg:	vector genomes
WGA:	wheat germ agglutinin
wpi:	weeks post-injection
WPRE:	woodchuck hepatitis virus posttranscriptional regulatory element
WT:	wild-type